SURFACE HARDENING OF AUSTENITIC FE–CR–NI ALLOYS FOR ACCIDENT-TOLERANT NUCLEAR FUEL CLADDING

by

ZHEN LI

Submitted in partial fulfillment of the requirements

For the degree of Doctor of Philosophy

Department of Materials Science and Engineering

CASE WESTERN RESERVE UNIVERSITY

January, 2018

Surface Hardening of Austenitic Fe–Cr–Ni Alloys For Accident-Tolerant Nuclear Fuel Cladding

Case Western Reserve University
Case School of Graduate Studies

We hereby approve the thesis[1] of

ZHEN LI

for the degree of

Doctor of Philosophy

Dr. Frank Ernst	**04/26/2017**
Committee Chair, Adviser Department of Materials Science and Engineering, CWRU	Date
Dr. Arthur Heuer	**04/26/2017**
Committee Member Department of Materials Science and Engineering, CWRU	Date
Dr. John Lewandowski	**04/26/2017**
Committee Member Department of Materials Science and Engineering, CWRU	Date
Dr. Sunniva Collins	**04/26/2017**
Committee Member Department of Mechanical and Aerospace Engineering, CWRU	Date
Dr. Scott Lillard	**04/26/2017**
Committee Member Department of Chemical and Biomolecular Engineering, The University of Akron	Date

[1]We certify that written approval has been obtained for any proprietary material contained therein.

Dedicated to my wife Xun Zhan, my daughters Macie Li, Joanna Li, my parents Liming Li, Yingnan Fan and parents in law Zhijun Zhan, Liping Gao with love

Table of Contents

List of Tables

List of Figures

Acknowledgements

0.1 Acknowledgements

At first, I would like to express my gratitude from the bottom of my heart to my thesis advisor Prof. Frank Ernst. Your keen sense and great wisdom in finding the truth in science and engineering guided me throughout my pursuit of my doctoral degree. Equally as important appreciation should be given to Prof. Arthur Heuer. I also owe thanks to my wife Dr. Xun Zhan, my two lovely daughters, my parents and parents in-laws for their long-term, tireless support. Without their altruistic love, it would not have been possible for me to finish the Ph. D. program in Department of Materials Science and Engineering at Case Western Reserve University. Moreover, I would like to acknowledge the financial support for the research project 12-3451 from the DOE-NEUP program under contract number 00128081. Finally, I appreciate the useful discussion with Prof. Harold Kahn, our collaborator Dr. Stuart Maloy from Los Alamos National Laboratory, Prof. Scott Lillard, Dr. Wei Niu from University of Akron, Prof. Thangadurai Paramasivam from Pondicherry University (India), Prof. Sunniva Collins from Case Western Reserve University, Peter Williams and Steve Marx from Swagelok company. Last but not least, I also want to thank the help from my colleagues, my friends and the scientists in the Swagelok Center for Surface Analysis of Materials (SCSAM) at Case Western Reserve University.

Abstract

Surface Hardening of Austenitic Fe–Cr–Ni Alloys For Accident-Tolerant Nuclear Fuel Cladding

Abstract

by

ZHEN LI

0.2 Abstract

Three Fe–Cr–Ni alloys (AISI-316L, AL-6XN and IN-718) were surface-engineered by infusion of interstitial solutes (C and N) for potential application as nuclear fuel cladding. However, an 'activation' process, which removes the Cr-rich oxide layer that blocks the infusion of interstitial solutes, is needed before these alloys can be successfully surface-engineered. An innovative and highly effective aqueous acid activation process was applied. The surfaces of these Fe–Cr–Ni alloys are successfully activated in 300 s to 600 s at room temperature compared to 21.6 ks at carburizing temperature with gaseous HCl activation. Moreover, the activated surface of Fe–Cr–Ni alloys can be well protected by immersing in ethanol before these specimens are transfered into the carburizing furnace. Specimens of the Fe–Cr–Ni alloy AISI-316L, IN-718 and AL6-XN were successfully surface-engineered by low-temperature carburization and low-temperature nitrocarburization. Near the alloy surface, up to 15 at% to 20 at% of carbon and 20 at% of

nitrogen were observed in Fe–Cr–Ni alloys – without detectable carbides. This high carbon and nitrogen fraction results in a threefold increase of surface hardness, significantly improved wear resistance and corrosion resistance of Fe–Cr–Ni alloys. Cr depletion can be seen in all the surface-engineered Fe–Cr–Ni alloys. Low-temperature carburization and low-temperature nitro-carburization can induce ferromagnetism in the surface of IN-718 ni-based alloy. The ferromagnetism detected in low-temperature carburized and low-temperature nitro-carburized IN-718 may have interesting applications, independent of nuclear technology. Thermal stability of low-temperature carburized material was tested by post-carburization heat exposure. No observable difference of properties (i. e. no observable precipitates, no detectable diffusion of interstitial solutes and no obvious change of the shapes of X-ray diffraction peaks and Auger concentration profiles) appeared in surface-engineered Fe–Cr–Ni alloys after exposure at 620 K in air in comparison with as-carburized Fe–Cr–Ni alloys. However, properties of low-temperature carburized and low-temperature nitro-carburized Fe–Cr–Ni alloys showed significant variation (i. e. metallography, X-ray diffractometry and scanning Auger microprobe profile) after exposure in the simulated loss of coolant accident environment (1070 K for 3.6 ks) compared to those of as-carburized Fe–Cr–Ni alloys. Carbon depletion and infusion were observed in the low-temperature carburized and low-temperature nitro-carburized Fe–Cr–Ni alloys after exposure to 1070 K for 3.6 ks. Among all these surface-engineered Fe–Cr–Ni alloys, low-temperature carburized IN-718 did not show

observable oxidation after exposure to the simulated loss of coolant accident environment. Non-treated and low-temperature carburized AISI-316L have severe stress corrosion cracking on the surface after exposure in a boiling water reactor simulated environment. However, stress corrosion cracking is not observable in the carburized IN-718 specimen. Finally, exposure to 1.5 MeV proton irradiation at elevated temperature (620 K), as well as exposure in the simulated loss of coolant accident environment (with no radiation at 1070 K for 3.6 ks), causes precipitation of nano-sized Cr-rich carbides in low-temperature carburized IN-718. These prevented the loss of Cr (as well as C) by evaporation under the loss of coolant accident. Among all the surface-engineered alloys, low-temperature carburized IN-718 has the most potential for nuclear cladding.

1 Introduction

1.1 Motivation

Zr-based alloys (e. g. Zircaloy^{TM}) have been widely used as nuclear fuel cladding materials in BWR (boiling water reactor) since 1960.[1] This is due to their low thermal neutron scattering cross sections σ (Zircaloy-4: $\sigma = 0.18\times10^{-28}\,m^2$) and high melting points, T_m (Zircaloy: $T_m > 2070\,K$).[2] Generally, the working temperature of BWR is around 560 K.[3] However, Zr-based alloys *do not* show good performance under working conditions of BWR: (1) Zr-based alloys have low wear resistance, therefore, prone to GTRF (grid-to-rod fretting) failure,[2,4,5] namely structural damage caused by friction between the fuel rod and the grid under flow-induced vibration. (2) Zr-based alloys have smaller thermal expansion coefficients, α (Zircaloy-4: $\alpha = 6.7\times10^{-6}\,K^{-1}$), than pellet material UO_2 ($\alpha = 10.5\times10^{-6}\,K^{-1}$).[2,6] Meanwhile, Zr-based alloys have large irradiation creep rate. Therefore, the gap between cladding and pellet can only be maintained for about 1.2×10^4 h.[2] Once the contact occurs, Zr-based alloys suffer from PCMI (pellet cladding mechanical interaction). PCMI causes deformation and stresses in the claddding, leading to SCC (stress corrosion cracking). (3) Zr-based alloys have relatively low thermal conductivities, κ (Zircaloy-4: $\kappa = 16.8\,W/mK$),[2] resulting in a high cladding temperature, thus shortening the service life of fuel claddings.

The Chernobyl and Fukushima Daiichi nuclear accidents show the disastrous behaviors of Zr-based alloys under LCA (loss of coolant accident) condition. When LCA happens, the temperature of pressurized water can reach to $\approx 1270\,\mathrm{K}$,[7] forming steam with high temperature and pressure. Zr-based alloys oxidize rapidly in such steam,[8,9] producing a large amount of hydrogen based on the reaction

$$\mathrm{Zr} + 2\mathrm{H_2O} = \mathrm{ZrO_2} + 2\mathrm{H_2}\,. \tag{1.1}$$

The hydrogen and the radioactive UO_2 can leak out of the fuel rods and enter the reactor buildings, causing explosions.

Therefore, we are looking for alternate materials, which possess improved performance under both working and accident conditions of BWR, to substitute the Zr-based alloys as fuel cladding for BWR. Specifically, the candidates should have much better wear, SCC and oxidation resistance, lower irradiation creep rate, higher thermal expansion coefficient α and thermal conductivity κ.

1.2 Materials Candidate

1.2.1 Austenitic SS (stainless steel)

One plausible alternative to Zr-based alloys are 300 series austenitic stainless steels ($\approx$ 18 at.%Cr, 10 at.%Ni) due to these characteristic properties: SS (stainless steel) has much lower irradiation creep rate; much higher thermal expansion coefficient α (AISI-348: $\alpha = 18.5\times10^{-6}\,\mathrm{K^{-1}}$); and higher thermal conductivity κ (AISI-348: $\kappa = 19.1\,\mathrm{W/mK}$) than those of Zr-based alloys.[2] Most importantly, 300 series austenitic SSs possess much better oxidation resistance under a high-temperature and high-pressure steam environment than that of Zr-based alloys, resulting from a high Cr concentration.[10–13] Historically, plasma

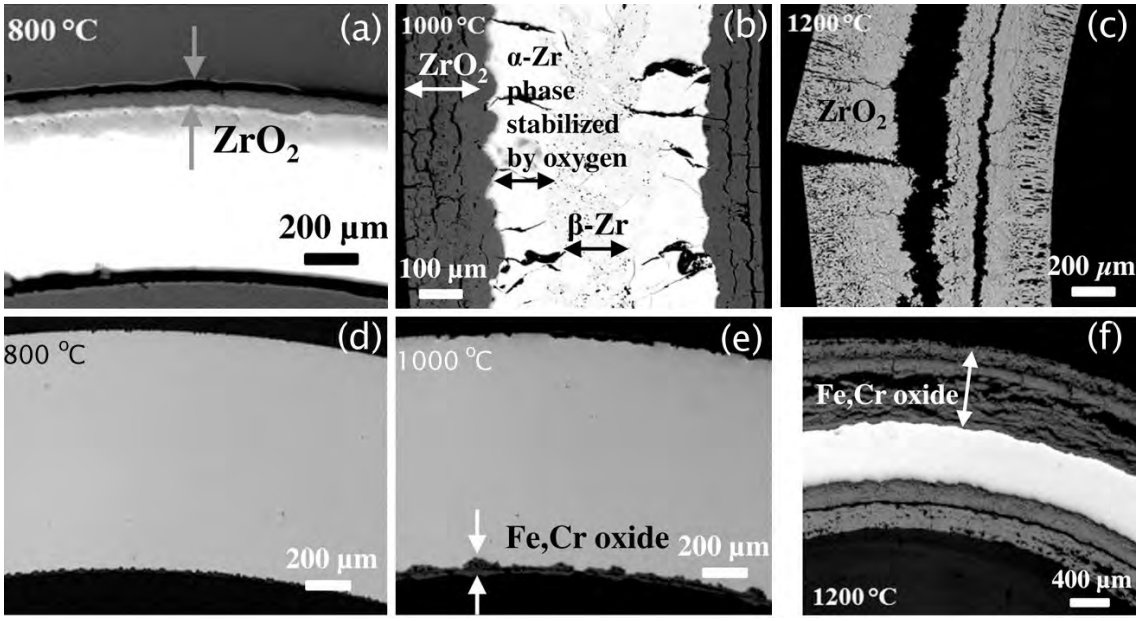

Figure 1.1. Optical micrographs of cross sections of Zircaloy-2 and AISI-317L after 28.8 ks exposure to 1 MPa steam at 1070 K, 1270 K, 1470 K, respectively. (a)-(c) Zircaloy-2. (d)-(f) AISI-317L.[10]

nitriding AISI-316L has already been applied in the nuclear industry.[14] Figure 1.1 a-f are micrographs of oxide layers on Zircaloy-2 and AISI-317L after 28.8 ks exposure to 1 MPa steam at 1070 K, 1270 K, 1470 K, respectively.[10] Due to similar compositions, Zr-based alloys have similar oxidation behavior. In the same way, the 300 series SSs also exhibit similar oxidation behavior due to their similar chemisty within the 300 series. At 1070 K and 1270 K, Zr-based alloys form a thick and loose ZrO_2 layer as well as brittle oxygen-stabilized α-Zr, while 300 series SSs form a thin and dense Fe, Cr oxide layer, preventing further oxidation of SSs matrix. This indicates that 300 series austenitic SSs have much slower metal-steam reaction rates than that of Zr-based alloys when the temperature is below 1270 K. At 1470 K, both Zr-based alloys and 300 series SSs encounter severe oxidation, forming loose and non-protective oxide layers. The rapid evaporation of SSs at

temperature higher than 1270 K is due to the reaction,[15]

$$\frac{1}{2}Cr_2O_3(s) + \frac{3}{4}O_2(g) + H_2O(g) \rightarrow CrO_2(OH)_2(g)\,, \tag{1.2}$$

causing Cr evaporation by forming a volatile Cr(VI) oxide hydroxide. After the protective Cr-rich oxide layer striped off quickly, severe oxidation occurred on the surface of 300 series austenitic SSs. Under LCA conditions, the cladding temperature is usually higher than 1270 K. Therefore, the oxidation resistance of 300 series SSs to high temperature (> 1270 K) and pressure steam should be improved before they can be considered as replacements of Zr-based alloys as fuel cladding.

In addition, SSs have similar hardness (AISI-348: 85 HRB) to that of Zr-based alloys (Zircaloy-4: 89 HRB),[2] suggesting that they are also prone to GTRF failure; SSs are also prone to SCC;[16–19] SSs have higher thermal neutron scattering cross sections, σ (AISI-348: $\sigma = 3.13\times10^{-28}$ m^2) than that of Zr-based alloys.[2] Therefore, to use SSs as fuel claddings, we need to overcome associated performance drawbacks through decreasing the thermal neutron scattering cross sections, σ, increasing the hardness and wear resistance to reduce GTRF failure, improving the SCC resistance, and increasing the oxidation resistance at temperatures above 1270 K.

1.2.2 Surface Treated Austenitic SSs

Thinner walls can be fabricated to reduce the high thermal neutron scattering cross section of SSs. It is expected that the other properties mentioned above can be improved by surface treatment (i. e. forming a near-surface diffusion zone by infusing small carbon or nitrogen atoms into the interstitial sites of the crystal structure of the Fe–Cr–Ni alloys).

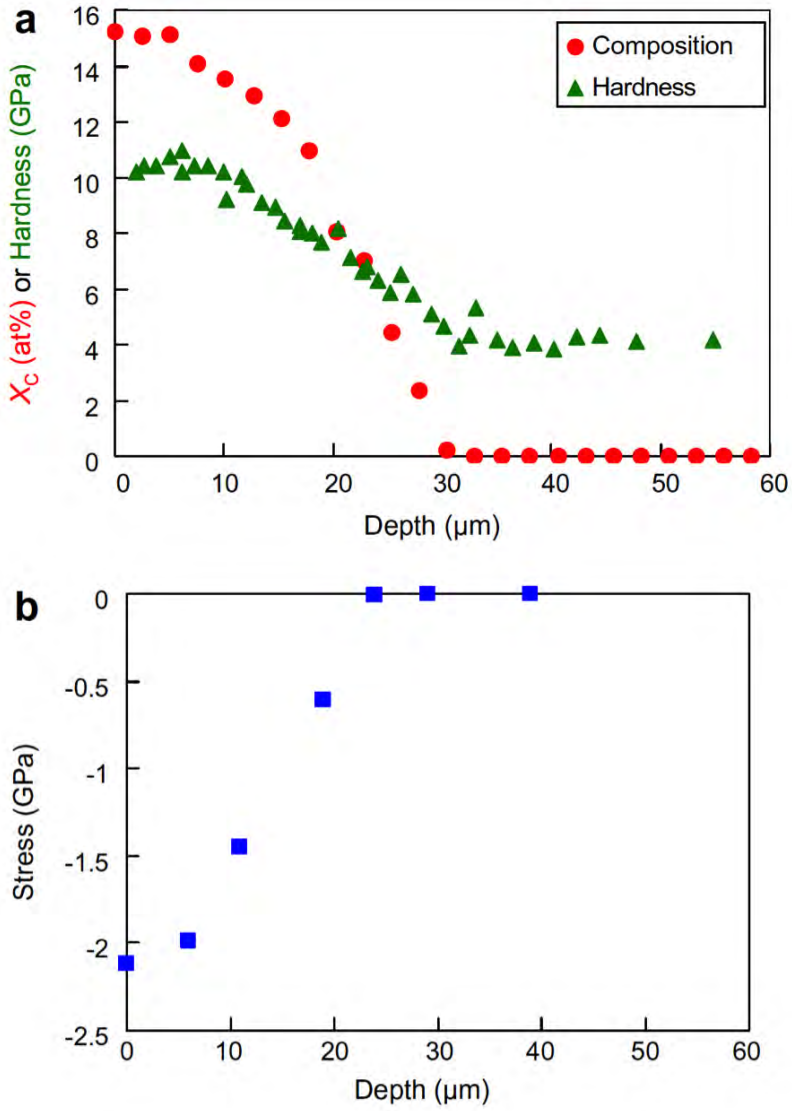

Figure 1.2. (a) Vickers hardness (triangles) and carbon concentration (circles) depth profiles. (b) Residual stress profile of carburized 316L stainless steel.[20]

In general, the near-surface region containing interstitial carbon or nitrogen atoms shows enhanced mechanical properties (strength and hardness) compared to its core region, since the interstitial atoms can pin dislocations and hinder dislocation movement under external stress.[20–24] The enhanced mechanical properties of the near-surface zone has been confirmed in Fig 1.2a, which shows the Vickers hardness of the near-surface

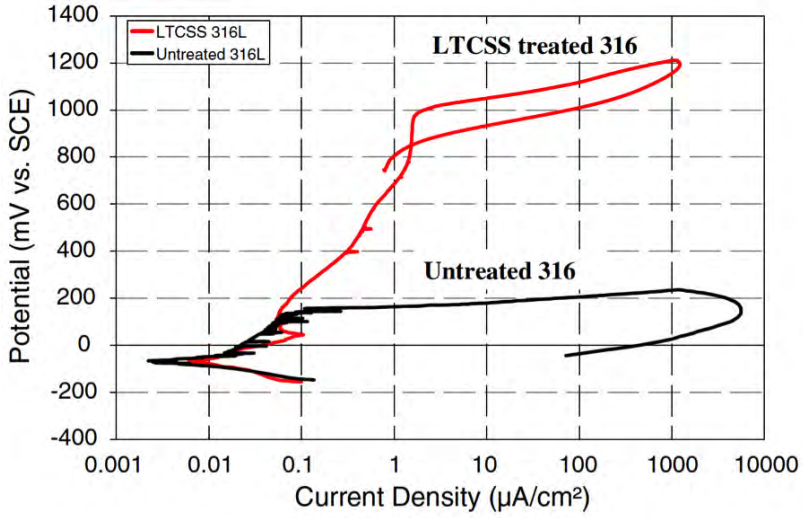

Figure 1.3. Potentiodynamic polarization curves of carburized and as-received AISI-316L, recorded in sea-water-like electrolyte (0.6 M NaCl solution).[24]

zone and AISI-316L core.[20] A higher hardness has been observed in the near-surface region than in the bulk material. Moreover, the higher carbon concentration results in higher hardness. In addition, carbon or nitrogen atoms dissolved interstitially can cause considerable compressive stress. For example, the compressive stress in the near-surface region of AISI-316L can reach ≈ 2 GPa, as shown in Fig 1.2b.[20] An improved wear resistance of the near-surface zone can then be expected as a result of the improved hardness and the compressive stress.

Surface containing interstitial carbon or nitrogen atoms also have improved corrosion resistance of the near-surface infusion region of the Fe–Cr–Ni alloys compared to its core.[23–25] Figure 1.3 compares the corrosion resistance of carburized and as-received AISI-316L.[24] As-received AISI-316L starts to show a passive region at voltages below 300 mV (versus the SCE (saturated calomel) electrode). The passive film breakdown occurs by pitting when the voltage reaches 350 mV. The carburized one, in contrast,

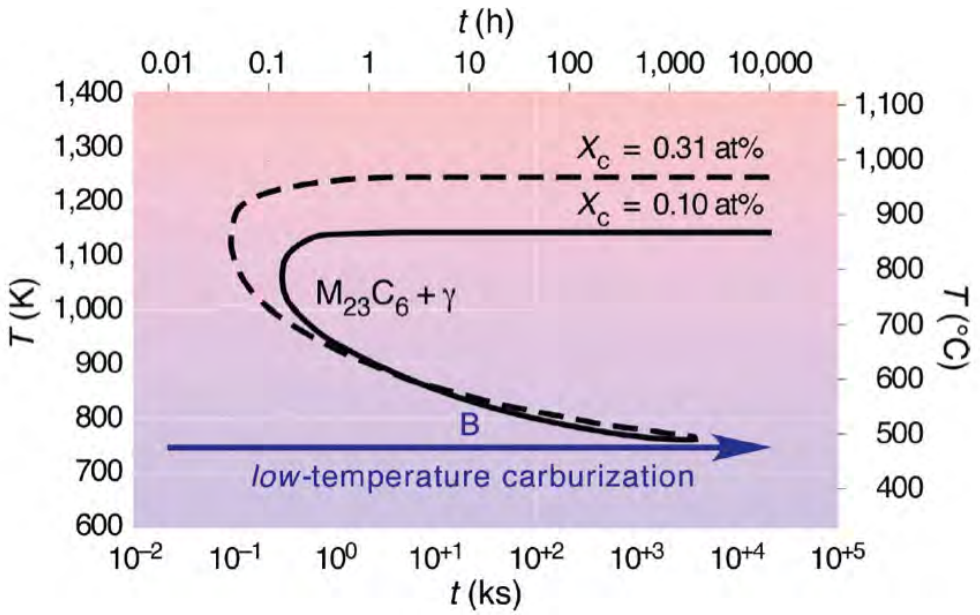

Figure 1.4. TTT diagrams of an AISI-316 austenitic SS with two different atom fractions X_C of carbon.[26]

exhibits a passive region up to around 1000 mV. Even at this high voltage (versus SCE electrode), there is no evidence that breakdown is induced by pitting corrosion, but by transpassive dissolution of the oxide. The large increase of breakdown potential (≈ 700 mV) suggests better corrosion resistance in carburized alloys. Moreover, the existence of compressive stress may offset the tensile stress from pellet material expansion, and thus improve the SCC resistance.

Therefore, properties of carburized or nitrocarburized Fe–Cr–Ni alloys were investigated under working and LCA conditions of BWR in this thesis. To accomplish the infusion of carbon or nitrogen atoms into these alloys, CSS (colossal super-saturation) engineering is the most effective way, and it is introduced in the following section.

1.3 Colossal Super-saturation Engineering

The infusion of carbon or nitrogen into SSs needs to avoid the formation of carbides or nitrides, since they can have detrimental effects on the mechanical properties and the corrosion resistance of Fe–Cr–Ni alloys.

The solution to this problem is to carburize or nitride SSs at lower temperature (called LTC (low-temperature carburization) or LTNC (low-temperature nitro-carburization)) where carbides or nitrides can only form after a long time (path B in Figure 1.4), by which a large amount of carbon or nitrogen atoms (the fraction can be 800 times the equilibrium solubility at the carburizing temperature) can stay in the interstitial sites instead of precipitating as carbides or nitrides.[21,27–31] This method is called CSS engineering. CSS can be achieved by fulfilling the following requirements:

1. The alloy contains metal atoms with a high affinity for carbon or nitrogen like Cr in AISI-316L.[27] It is well known that equilibrium carbides are rich in Cr.[32]
2. The processing temperature is chosen such that the metal atoms (Fe, Ni, Cr, *etc.*) are practically immobile, therefore, Cr cannot precipitate in the form of carbides or nitrides, whereas the carbon atoms residing in interstitial sites can still diffuse over useful distances (a few micrometers) within the processing time.[33]

IN-718 is a precipitation-hardenable Ni-based alloy; however, it is of interest to see how precipitate-free IN-718 responds to the low-temperature carburizing process. In this thesis, solutionized IN-718 ni-based alloy was studied. According to the TTT (time-temperature-transformation) diagram of IN-718,[21] the highest carburization temperature is 860 K, under which precipitates do not form after a long time, indicating that every property changed after low-temperature carburization was due to the infusion

of carbon. Although a high carburization temperature leads to a fast diffusion of carbon into IN-718, it can also result in notable Cr depletion, reducing its corrosion resistance. Cr depletion usually happens when temperature is higher than 800 K according to Sharghi-Moshtaghin.[21] In addition, the carburization temperature cannot be chosen as the carburizing temperature of AISI-316L (720 K), since the diffusivity of carbon in Ni-based alloys is lower than in Fe-based alloys. This means that IN-718 cannot be properly carburized at such temperatures. Sharghi-Moshtaghin[21] found 780 K is the most appropriate carburizing temperature for IN-718 to achieve the comparable diffusion depth as AISI-316L in the similar carburizing time. Therefore, the carburization temperature of IN-718 was selected as 780 K in this thesis.

CSS is a highly conformal post-process to components in their final shape, without changing their dimensions, and at low cost. This can be accomplished using the following methods: (1) gas phase, (2) plasma, (3) encapsulation, and (4) salt bath, which have all been used to process CSS, and are reviewed in the following paragraphs.

1.3.1 Gas Phase Method

The gas phase method was invented by Swagelok Company (Solon, OH).[34] The LTC or LTNC process of alloys is carried out in a customized J4915 furnace manufactured by CVD Equipment Corporation for CWRU (Case Western Reserve University), shown in Fig 1.5a. The configuration of the main chamber of the furnace is shown in Fig 1.5b. The diameter and the depth of the main chamber are 0.21 m and 0.7 m, respectively, yielding a total chamber volume of 2.4×10^{-2} m^3. The main chamber is uniformly heated and the temperature can be precisely controlled to ±0.2 K. The alloys were placed in a basket located at the center of the chamber and the total pressure in the chamber was kept at 0.1 MPa. Several gas delivery channels are equipped to precisely control (precision:

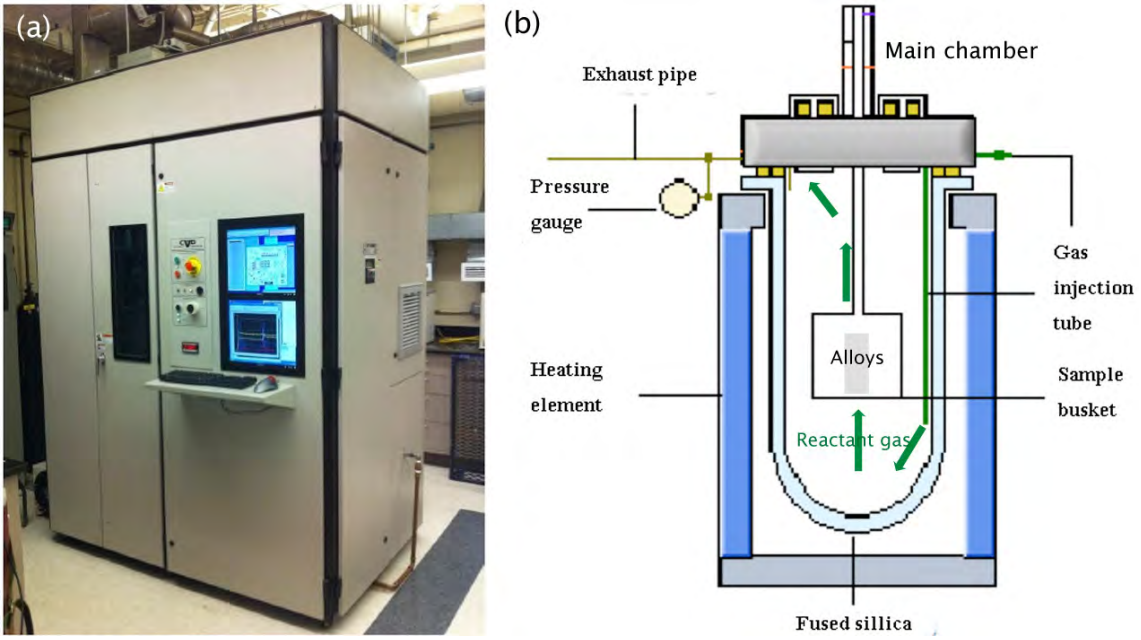

Figure 1.5. (a) J4915 furnace. (b) Main chamber of J4915 furnace.

2×10^{-6} m^3/s) the injection gas flow rate. To ensure a uniform mixture of gaseous components, the sample basket rotates during the process. The gas phase method can control the carbon and nitrogen activity in LTC and LTNC process by precisely controlling the gas flow rates.

A typical LTC or LTNC "recipe" is shown in Fig 1.6. The first step is called activation, aiming to remove the passivating layer (Cr-rich oxide layer) using gaseous HCl at 520 – 720 K for 7.2 ks. Subsequently, carburization or nitriding is operated under a CO-H_2-N_2, C_2H_2-H_2-N_2 or NH_3-H_2-N_2 gas atmosphere at 720 – 780 K for 7.2 ks.[21,35,36] The carbon or nitrogen atoms are provided based on the reactions

$$CO + H_2 \rightarrow C + H_2O, \tag{1.3}$$

$$C_2H_2 \rightarrow 2C + H_2, \tag{1.4}$$

$$NH_3 \rightarrow 2N + \frac{3}{2}H_2, \tag{1.5}$$

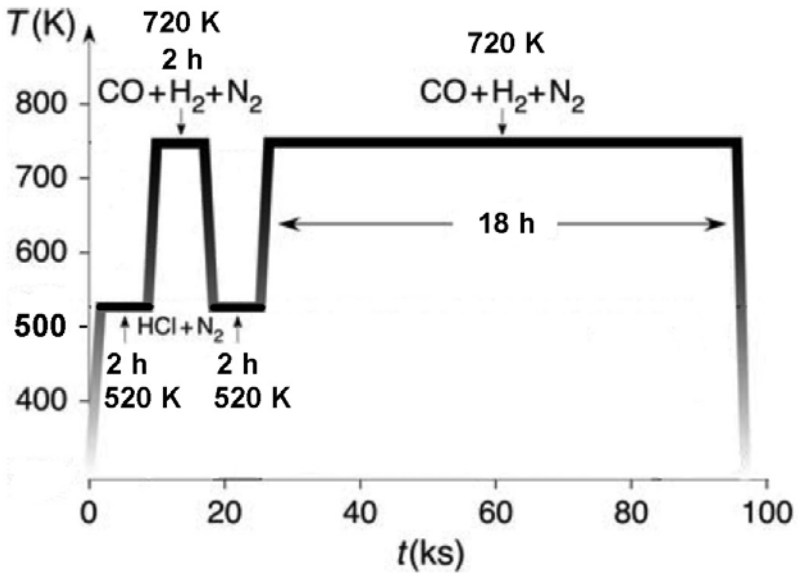

Figure 1.6. Gas phase LTC or LTNC process.

respectively, enabled by catalysis of the alloy surface. The selected temperature range (720 – 780 K) for LTC or LTNC is because substitutional solutes (e.g. Cr, Ni) diffuse much slower than that the interstitial solutes (e.g. carbon, nitrogen). For example, the diffusivity of Cr at 720 K in austenitic SSs is 10^{-21} m^2/s, whereas the carbon diffusivity is 10^{-16}-10^{-17} m^2/s.[27] Then, the activation step is repeated to remove the Cr oxide layer built during the 7.2 ks carburization or nitriding. After that, a long time (usually ≈ 72 ks) carburization or nitriding process is operated at the carburizing/nitriding temperature, providing the near-surface region with interstitial carbon or nitrogen.

Gas phase (C_2H_2 was used in this case) LTC of AISI-316L based on the "recipe" yields a uniform, precipitate-free region with a smoothly graded carbon concentration-depth profile and a thickness of about 25 μm as shown in Fig 1.7. The featureless layer is the carburized region ('case'), in which the carbon concentration is high enough to prevent

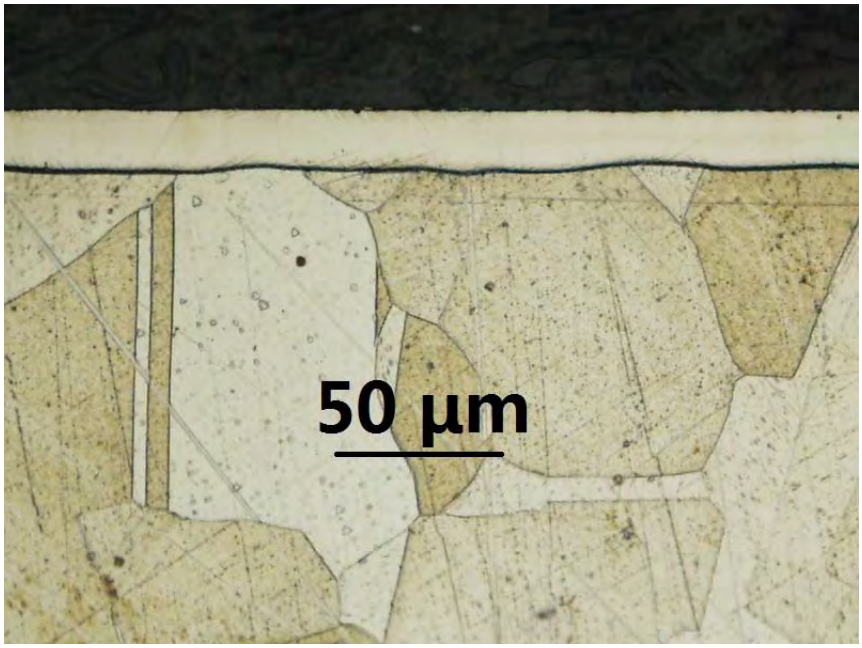

Figure 1.7. Metallographic image of gas phase (C_2H_2) LTC of electro-polished AISI-316L.[35]

the surface from etching. Generally, a carbon concentration of 1 at%[20,31] is needed to keep the case featureless.

Somers and Christiansen found C_2H_2 can activate and carburize the surface of SSs simultaneously.[37] This means that the double activation steps mentioned above could be replaced by acetylene carburization process. However, C_2H_2 carburization cannot yeild a uniform layer on SSs samples with coarse surface finish, which is probably because C_2H_2 cannot remove a nano-crystalline layer that is observed on SSs samples resulting in blocking the infusion of carbon atoms, although it worked well to remove the Cr-rich oxide layer on SSs specimens.[35]

1.3.2 Plasma Method

LTC or LTNC can also be achieved by plasma process.[28,38,39] Figure 1.8[28] shows a plasma unit, where mixed gas turn to plasma with high energy, carburizing or nitriding the

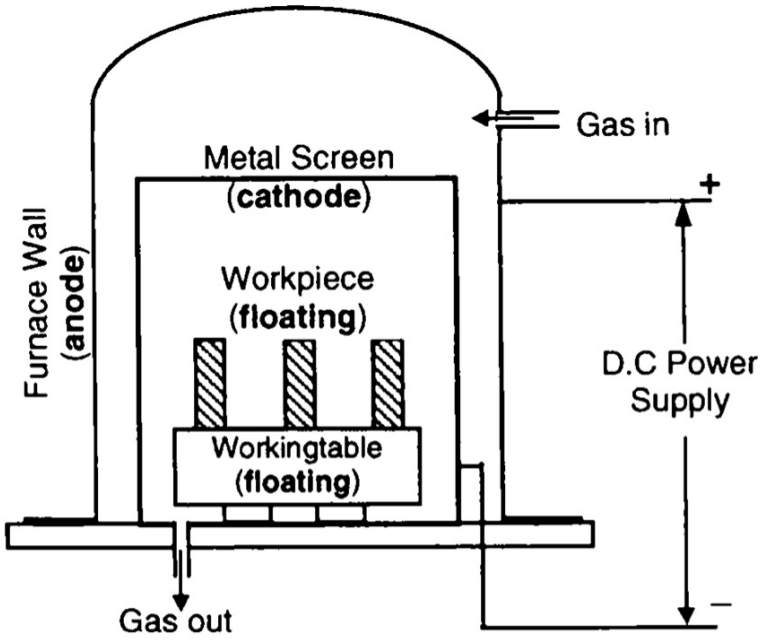

Figure 1.8. Schematic structure of a plasma unit.[28]

working piece in the furnace, by applying electric field. The most widely used precursor gas for plasma carburizing and nitriding are CH_4-H_2 and N_2-H_2, respectively.[28]

Plasma method can effectively remove the passive Cr oxide layer on the sample surface by *in situ* sputtering, and there is no need for extra activation step before LTC or LTNC process. However, the plasma method is prone to generate a non-uniform carburized/nitriding surface zone because of the non-uniform electric discharge phenomenon.[40] Therefore, the sample with a complicated geometric shape after Plasma LTC or LTNC may perform very differently due to different surface treatments in different areas of the specimen.

1.3.3 Encapsulation Method

Ernst *et al.* invented a way to nitriding Ti with encapsulation method.[41] Agaponova applied this encapsulation method to nitro-carburize AISI-316L.[42] In this method, an alloy

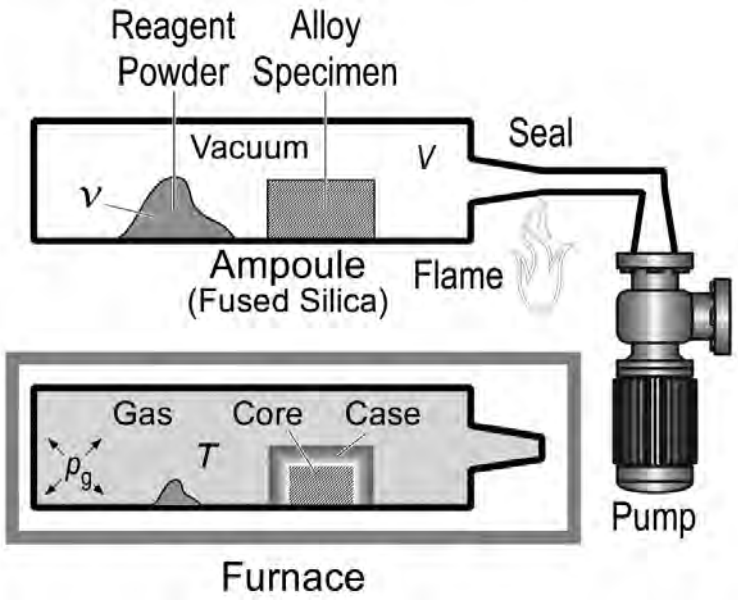

Figure 1.9. Schematic process of encapsulation method for LTNC.[43]

sample is encapsulated in an evacuated fused-silica ampoule together with e. g. urea ($CO(NH_2)_2$) (Fig 1.9). Ampoule is evacuated by oil pump and then purged with Ar. Repeat this step two times, and evacuate the ampoule to ≈ 2 Pa. The ampoule is then sealed by melting the silica using an oxy-acetylene torch. Subsequently, the ampoule is heated in a furnace up to ≈ 720 K for 7.2 ks (2 h). Maximum 0.13 g of urea can be sealed in an evacuated glass container with the diameter of 5 mm, wall thickness of 1 mm and length of 200 mm, otherwise explosion will happen with the elevating temperature. Upon heating, pyrolysis of the reagent generates gaseous species under increased pressure (typically 0.5 MPa). Some species effectively "activate" the sample surface (strip the passivating Cr-rich oxide layer). At the sample surface, other or the same species further decompose into elemental mono-atomic nitrogen or carbon. Finally, nitrogen and carbon diffuse into the surface of the alloys.

Encapsulation method only took 7.2 ks (2 h) at 723 K to achieve the same case thickness as that of gas phase method (nitro-carburizing) at the same temperature for 72 ks (20 h). However, the experimental data (case thickness and surface concentration *etc.*) are variable due to the following possible experimental errors: (1) mass loss during weighing the 0.13 g urea, (2) urea sticking in the unsealed part of glass tube will also cause mass loss, (3) the length of the glass tube cannot be sealed exactly with the length of 200 mm and (4) the vacuum condition in the sealed glass tube is different tube by tube.

1.3.4 Salt Bath Method

The salt bath method immerses samples into molten (700 – 780 K) cyanide- or cyanate-base salt for nitriding.[44,45] Cyanide-base salt baths contain a high percentage of toxic potassium and sodium cyanides, while cyanate-based bath is environmental friendly. The major components of salts in the cyanate-based bath are M_2CO_3 (M: halogen elements, e. g. K, Na, *etc.*) and urea ($CO(NH_2)_2$). Furthermore, cyanate-base salt bath nitriding process is a low-cost method. However, the nitrogen activity in salt bath process cannot be easily controlled.

1.4 Approach

In this project, the goal is to find material candidates for fuel claddings, which have better performance than Zr-based alloys, under working and LCA conditions of BWR. Firstly, three kinds of austenitic Fe–Cr–Ni alloys were selected: AISI-316L, AL-6XN, and IN-718, as matrix materials. AISI-316L contains 3 to 4 times less carbon than AISI-316

Table 1.1. Main chemical compositions (> 1.0 at%) of AISI-316L SS, AL-6XN, and IN-718. The unit of atomic concentration is at.%.

Material	Shape	Fe	Cr	Ni	Nb	Mo	Mn	Al	Si	Ti
AISI-316L	Coupon	70	19	9	–	2	–	–	–	–
	Tube	69	17	11	–	1	2	–	–	–
	Bar	70	18	10	–	1	1	–	–	–
AL-6XN	Coupon	43	24	25	–	4	2	–	2	–
IN-718	Coupon	19	21	53	3	2	–	1	–	1
	Tube	19	20	54	3	2	–	1	–	1
	Bar	19	21	54	3	2	–	–	–	1

stainless steel, other than that there is no difference between them. In all these Fe–Cr–Ni alloys, Ni helps to keep the FCC (face-centered cubic) structure of these alloys and Cr keeps them 'stainless' by forming a dense Cr-rich (Cr_2O_3) oxide layer with the thickness around 1 nm. The reasons that AISI-316L is selected are:

1. AISI-316L is one of the 300 series austenitic SSs, which has good oxidation resistance due to its high Cr ($17-19$ at%) and Ni (≈ 10 at%) concentrations , shown in Table 1.1. Its oxidation resistance is higher than that of 200 series austenitic SSs, which have lower Cr and Ni concentrations.
2. High Cr concentration is also beneficial to LTC and LTNC due to its high affinity for carbon and nitrogen.
3. AISI-316L contains Mo (Table 1.1), which produces better corrosion resistance and high temperature strength than other 300 series of austenitic SSs that do not contain Mo (i. e. 302, 304, 321, 347).

Compared to AISI-316L, the advantage of AL-6XN is

1. As a super-austenitic SS, AL-6XN contains more Cr, Ni and Mo (Table 1.1). Therefore, better oxidation and corrosion resistance as well as high temperature strength can be expected for AL-6XN than for AISI-316L.[46]

IN-718 belongs to Ni-based Ni–Fe–Cr austenitic alloys and it has better properties than AISI-316L and AL-6XN for the following reasons:

1. IN-718 has slightly higher Cr (≈ 20 at%) concentration than that of AISI-316L and has ≈ 3 at% Nb, which AISI-316L and AL-6XN do not have, shown in Table 1.1.
2. It has been reported that IN-718 has better oxidation and corrosion resistance than that of AISI-316L and AL-6XN.[47,48]
3. In addition, IN-718 has been widely used in aircraft with high working temperatures such as turbine blades, critical rotating parts, airfoils, supporting structures and pressure vessel, due to its appropriate combination of strength and ductility to about 920 K. Therefore, IN-718 should have the best oxidation resistance, corrosion resistance, as well as high temperature strength among the three alloys.

Secondly, to use these three Fe–Cr–Ni austenitic alloys as fuel claddings, we need to further improve their hardness, as well as wear, SCC and oxidation resistance to a level, at which they can avoid GTRF failure, SCC and cladding failure under a LCA. Therefore, we process LTC and LTNC on these alloys. In this thesis, we applied gas phase method to process the LTC and LTNC.

Three shapes of these alloys are used: coupon, tube, and bar. Tubes are used for LTC, LTNC and for further property evaluation since they are the shape required by fuel claddings. Real fuel cladding is closed in one end, the specimens tested in this thesis

are open-ended tubes. In addition, the tensile stress response of such tubes can directly correspond to practical application conditions. To study the SCC behavior to one surface, bars are used. Moreover, coupons are used for most of the property evaluations due to the straightforward geometry (flat surface).

Finally, the origin of different behavior of these carburized and nitro-carburized Fe–Cr–Ni austenitic alloys was discussed, so as to give a guidance for finding fuel cladding candidates with better properties.

2 Experimental

The properties of these Fe–Cr–Ni austenitic alloys before and after LTC and LTNCwere investigated to evaluate their possible application as fuel cladding under the working and the LCA conditions of BWR. The properties include:

1. The quality of carburized or nitro-carburized near-surface region: XRD (X-ray diffractometry) provides the phase state information after carburization and nitro-carburization. Metallography and SAM (scanning Auger microprobe) provides the information of the thickness and the concentration depth profiles of this near-surface zone. An interstitial diffusion region with uniform thickness and no precipitates is required for further property evaluations.
2. Hardness and wear resistance of the carburized or nitro-carburized near-surface zone. Such information can be used to evaluate the resistance of GTRF failure.
3. Oxidation resistance of the carburized or nitro-carburized near-surface region in air at 620 K (to simulate the working temperature of BWR), as well as in air and steam at 1070 K (to simulate the LCA conditions of BWR). After oxidation, the carburized near-surface zone is then investigated by XRD, SAM, and TEM (transmission electron microscopy).

4. SCC resistance of the carburized or nitro-carburized alloys under tensile stress and high-temperature and pressurized water to simulate the working condition of BWR. The cracking behavior is then investigated by SEM (scanning electron microscopy).
5. Irradiation resistance of the carburized or nitro-carburized near-surface region to proton irradiation in air at 620 K to simulate the working condition of BWR. The irradiated samples are then studied by TEM to understand the microstructure evolution during irradiation.

Specific processing parameters for various experiments and characterization techniques after these experiments are introduced in detail in the following sections.

2.1 AAA (aqueous acid activation)

The Cr_2O_3-rich oxide layer needs to be removed before carburization can happen. An AAA (aqueous acid activation) process was found to achieve this goal. The AAA procedure includes the following steps: (1) Fe–Cr–Ni alloys are immersed in aqueous HCl (22.4 at%) at room temperature for 600 s and (2) Fe–Cr–Ni alloys are taken out from the aqueous HCl and are immediately immersed in ethanol at room temperature (for roughly 300 s) until they are placed in a nitrogen-filled carburizing furnace without drying the ethanol on their surface. It is very critical to immerse the specimen in ethanol to prevent the activated surface from re-oxidizing. The AAA method was not applied to every specimen, however it is clearly stated in this thesis if this method has been applied to specific specimens. More detailed information can be found in Appendix A.

2.1.1 XPS (X-ray photoelectron spectroscopy)

To reveal the Cr oxidation state after aqueous HCl activation, XPS (X-ray photoelectron spectroscopy) was performed on 0.6 ks aqueous HCl activated AISI-316L at room temperature using a VersaProbe (Physical Electronics, Inc., USA), equipped with an Al-K_α source ($h\nu$ = 1486.6 eV). The specific treatment parameters of AISI-316L are shown in Table 2.1. To remove the carbon contamination before spectrum acquisition, the samples were cleaned *in situ* by Ar sputtering under conditions corresponding to high vacuum for about 10 s. The peak FWHM (full-width at half maximum) resolution was set to 0.7 eV. The core-level binding energies of Cr-2p 3/2 were determined by fitting the peaks using Multipak software.

Table 2.1. AISI-316L samples preparation parameters before XPS.

	Immerse in C_2H_6O	Immerse in H_2O
Time/ks	0.3	0.3
	1.8	1.8
	3.6	3.6

2.2 Gas Phase Processing

The shapes and dimensions of AISI-316L, AL-6XN, and IN-718 specimens are shown in Table 2.2. LTC was used for all these alloys, and LTNC for IN-718.

All the gases used for LTC and LTNC were supplied by Airgas Inc, including industrial grade acetylene (C_2H_2) dissolved in acetone (up to 4%), CO (purity: 99.99%), liquid N_2 (purity: 99.99%), ultra-high purity H_2 (purity: 99.99%), anhydrous ammonia (NH_3) (purity: 99.99%) and hydrogen chloride (HCl) (99.5%).

Table 2.2. Shapes and dimensions of AISI-316L, AL-6XN, and IN-718 samples.

Coupon	Material	Length/mm	Width/mm	Thickness/mm
	AISI-316L	50	50	0.38
	IN-718	50	50	0.25
	AL-6XN	50	50	0.6
Tube	Material	Length/mm	Outer Diameter/mm	Inner Diameter/mm
	AISI-316L	140	10.1	9.45
	IN-718	140	10.1	9.45
Bar	Material	Length/mm	Gauge Length/mm	Gauge Diameter/mm
	AISI-316L	80	25.4	2.5
	IN-718	80	25.4	2

2.2.1 LTC of Fe–Cr–Ni Alloys

The LTC recipes of Fe–Cr–Ni alloys are shown in Fig 2.1. AISI-316L was double activated by gaseous HCl at 600 K for 7.2 ks (2 h). After these activation steps, AISI-316L was carburized by a gas mixture of CO and H_2 at 720 K for 7.2 ks (2 h) and for 64.8 ks (18 h), respectively. The selection of the carburizing temperature is based on the TTT diagram of AISI-316, at which carbides do not form after a long time.[26] During the process, N_2 was used as carrier gas, which is stable and does not react with other gas phases. The carbon activity was controlled by the concentration of CO, H_2 and N_2 (i. e. the flow rates of these gases). The flow rates of HCl, CO, H_2 and N_2 are shown in Table 2.3.

AL-6XN was activated and carburized simultaneously by a gas mixture of C_2H_2 and H_2 at 720 K for 72 ks (20 h). Since AL-6XN also belongs to austenitic SSs, the selection

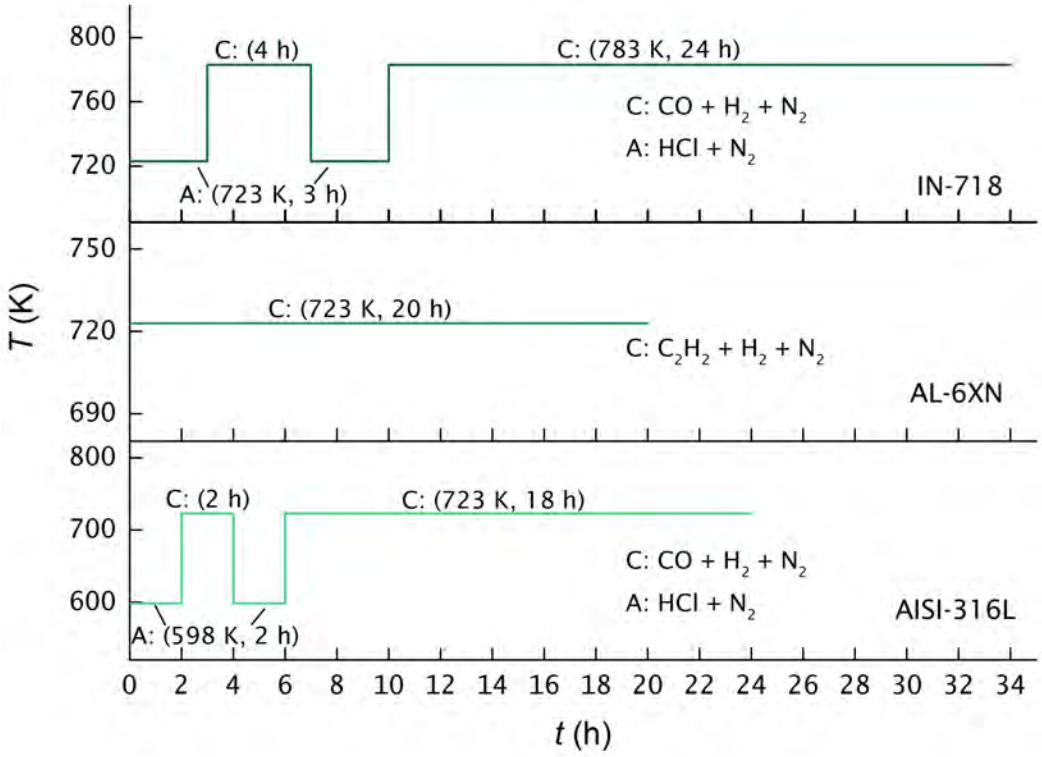

Figure 2.1. LTC recipes of AISI-316L, AL-6XN, and IN-718.

of the carburization temperature can also refer to the TTT diagram of AISI-316.[26] During the process, N_2 was also used as carrier gas. The flow rates of C_2H_2, H_2 and N_2 are shown in Table 2.3. According to Ge,[31] surface finish strongly influences the efficiency of C_2H_2-based LTC of AISI-316L. The samples with the finer surface finishes develop a thicker and more uniform carburized near-surface diffusion zone. The reason is that the combination of deformation-induced layer, which consists of nano-crystalline grains ($\approx$ 10 nm diameter), and the Cr oxide layer cannot be completely removed by C_2H_2, which therefore prevents the diffusion of carbon atoms. Due to the lack of the experimental data of C_2H_2-based LTC of AL-6XN, AL-6XN specimens were carburized with different surface finishes: water-cooled mechanical polishing with SiC grit P320, P800, P4000 papers, as well as electro-polishing with an electrolyte consisting of H_2SO_4 : H_3PO_4 : H_2O

in the ratio of 11 : 6 : 3. Moreover, to further improve the quality of the carburized near-surface region, the deformation-induced layer and oxide layer should be fully removed, considering the poorer efficiency of C_2H_2. Therefore, a second set of AL-6XN samples (the same surface finishes as mentioned above) were prepared, and they were immersed in aqueous HCl at room temperature for 600 s, and then these specimens were immersed in ethanol before C_2H_2-based LTC.

Table 2.3. Gas flow rates during activation and carburization process.

Activation	N_2 (m/s)	HCl (m/s)	–	Carbon activity
AISI-316L, IN-718	8.7×10^{-4}	9.6×10^{-5}	–	–
Carburization	N_2 (m/s)	CO (m/s)	H_2 (m/s)	–
AISI-316L, IN-718	4.3×10^{-4}	9.6×10^{-5}	4.3×10^{-4}	0.8
Carburization	N_2 (m/s)	C_2H_2 (m/s)	H_2 (m/s)	–
AL-6XN	2.4×10^{-3}	4.8×10^{-5}	1.4×10^{-4}	0.9

IN-718 sample was double activated by gaseous HCl at 720 K for 10.8 ks (3 h). The higher temperature and longer time for activation of IN-718 is because IN-718 is a Ni-based superalloy, which is more corrosion-resistant than AISI-316L and AL-6XN. After these activation steps, IN-718 was carburized by a gas mixture of CO and H_2 at 780 K for 14.4 ks (4 h) and for 86.4 ks (24 h), respectively. During the process, N_2 was used as carrier gas. The gas flow rates of HCl, CO, H_2 and N_2 are shown in Table 2.3.

Table 2.4. Gas flow rates during nitro-carburization of IN-718.

Activation	N_2 (m/s)	HCl (m/s)	–	–
	8.7×10^{-4}	9.6×10^{-5}	–	–
Nitro-carburization	CO (m/s)	NH_3 (m/s)	N_2 (m/s)	H_2 (m/s)
	9.6×10^{-5}	9.6×10^{-5}	4.3×10^{-4}	4.3×10^{-4}
Carbon activity	0.8	–	–	–
Nitrogen activity	–	1500	–	–

2.2.2 LTNC of IN-718

IN-718 was also processed with LTNC. The LTNC recipe is similar to the LTC recipe, shown in Fig 2.1, but with a different nitro-carburizing gas mixture. Specifically, IN-718 was double activated by HCl gas at 720 K for 10.8 ks (3 h). After these activation steps, IN-718 was nitro-carburized by a gas mixture of CO, NH_3 and H_2 at 780 K for 14.4 ks (4 h) and for 86.4 ks (24 h), respectively. The nitrogen atoms were provided by NH_3. During the process, N_2 was used as carrier gas. The flow rates of HCl, CO, NH_3, H_2 and N_2 are shown in Table 2.4.

2.3 Characterization of CSS-Engineered Near-surface Region

2.3.1 XRD (X-ray diffractometry)

XRD (X-ray diffractometry) was performed on non-treated and CSS-engineered (LTC and LTNC) Fe–Cr–Ni alloys to reveal the phases. XRD was also performed on non-treated

and CSS-engineered Fe–Cr–Ni alloys after oxidation tests to reveal the phases after oxidation. X-ray diffraction patterns were produced by a Bruker Discover D8 X-ray diffractometer. This instrument is equipped with a monochromatic Co-Kα radiation source (λ = 0.17889 nm). The peak positions were calibrated using an Al_2O_3 reference sample.

2.3.2 Metallography

Due to the different corrosion resistance of non-treated core and CSS-engineered (LTC and LTNC) near-surface zone of Fe–Cr–Ni alloys, the thickness of the diffusion zone can be observed by OM (optical microscopy) after etching. Specifically, the cross-sections were mounted vertically, and polished with P800 SiC grit paper, 9 µm diamond paste, 3 µm diamond paste and finally 0.1 µm diamond paste to obtain mirror-like surfaces. The etchant comprises HCl, HNO_3 and H_2O with the volume ratio of 2:1:1. A few drops of the reagent were applied on the cross-sections of AISI-316L, AL-6XN, and IN-718 for 60 s, 90 s and 90 s, respectively. Optical images were recorded on a laser scanning confocal microscope (Olympus FV1000).

2.3.3 SAM (scanning Auger microprobe)

The elemental concentration depth profiles of CSS-engineered Fe–Cr–Ni alloys were obtained by analyzing the cross-sectional specimens with a PHI680 SAM (scanning Auger microprobe), made by Physical Electronics. The probe size is 20 nm. In order to minimize artifacts introduced by adventitious carbon, an established technique of continuous Ar^+ sputtering was applied.[49] For precise quantification of the carbon concentration as a function of depth z below the surface, standard data obtained from specimens with certified carbon concentrations is applied as the reference to the specimens in this thesis.[49]

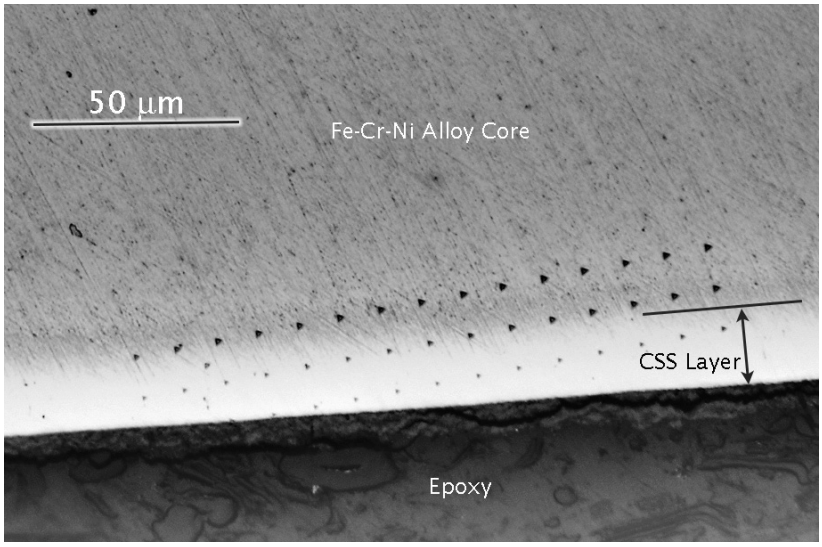

Figure 2.2. Typical nano-indentation setting for hardness depth profile of CSS-engineered Fe–Cr–Ni alloys. The black triangles are indentations.

2.4 Properties of CSS-engineered Near-surface Diffusion Zone

2.4.1 Hardness

The carburized or nitro-carburized near-surface region usually has a thickness in the range of $10-40\,\mu m$. Therefore, to reveal the influence of carbon or nitrogen concentration on the hardness of Fe–Cr–Ni alloys, a hardness test with a high spatial resolution is required. This can be fulfilled by nano-indentation. Flat and fine polished (mechanical polishing followed by polishing with 0.1 μm diamond paste) cross-sectional samples were prepared for nano-indentation. Nano-indentation tests were operated on an Agilent G200 nano-indenter (Keysight). The applied load is 1 gf. To obtain a hardness depth profile with a high spatial resolution and to eliminate the influence of neighboring indents, a specific indentation arrangement was set up, as shown in Fig 2.2. Specifically, 45 indents were distributed in a rectangular lattice with three parallel rows and with 15

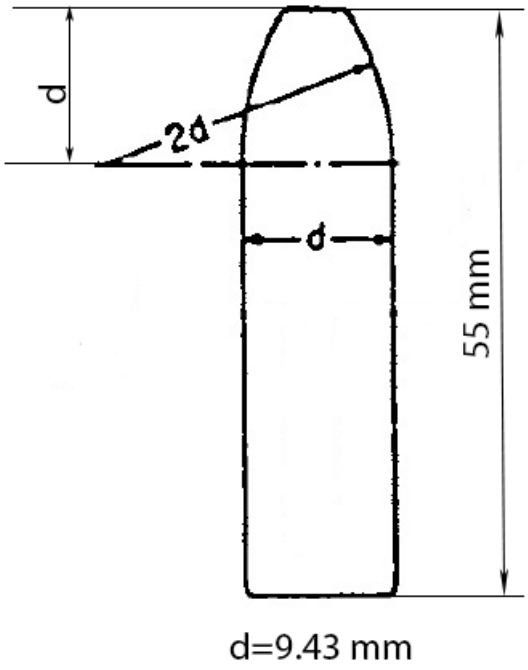

Figure 2.3. Schematic diagram of pin inserted into the ends of AISI-316L tube.

indents in each row. The shortest distance between two indents is 10 µm. This rectangular lattice group of indents was placed in a certain angle to the free surface of the carburized or nitro-carburized near-surface zone, for example 15°, so that the indents can reach many different depths of the carburized or nitro-carburized near-surface region.

2.4.2 Mechanical Properties

Tensile Strength. Tensile tests were conducted on the non-treated and the CSS-engineered Fe–Cr–Ni tubes based on ASTM (American Society for Testing of Materials) E8/E8M.[50] Two snug fit pins were inserted into the two ends of a tube before tensile tests. A schematic diagram of the pin is seen in Figure 2.3. Snug-fitting metal plugs were inserted far enough into the ends of tubular specimens to allow the jaws to grip the specimens properly. The total length of the pin was 55 mm with 5 mm outside the tube when testing the tubular

AISI-316L and IN-718 specimens. Tensile tests were performed on a Instron Model-1125 screw driven machine. MTS-Test-Works software and extensometer were linked to this instrument. Strain rate of the tensile test was $4.2\times10^{-4}\,s^{-1}$, and the gauge length was 40 mm.

Wear Resistance. Dry wear in air was conducted on non-treated and CSS-engineered AISI-316L coupons. The method is the ball-on-plate linear-motion. During the test, the sapphire ball is moving on the specimen back and forth. This test was performed on a BUMT (Bruker Universal Mechanical Tester). The specific test parameters followed ASTM G133, except that the standard load in ASTM G133 is 2.5 kg, which is too high for the non-treated AISI-316L coupon with the thickness of 380 μm. Therefore, the load was lowered to 1 kg.

2.4.3 Oxidation Tests

Oxidation Resistance and Thermal Stability Tests. Two types of high temperature exposure tests were carried out on the Fe–Ni–Cr alloys. One exposes non-treated and CSS-engineered Fe–Ni–Cr alloys at high temperatures, denoted as PCHE (post-carburization heat exposure). PCHE considers two different conditions, shown in Table 2.5. PCHE-A simulates the working temperature of an BWR. PCHE-B, with its higher temperature and shorter duration, corresponds to the LCA condition.

2.4.4 SCC Tests

To study the role of the CSS-engineered near-surface region on stress corrosion cracking (SCC) behavior, SSRTs (slow strain rate tests) were carried out on Fe–Cr–Ni bars, with dimensions shown in Table 2.2. SSRTs were performed in an autoclave which was connected to a recirculating high pressure-high temperature water loop. With controlled

Table 2.5. Post CSS-engineering heat exposure

Designation	Temperature	Duration	Ambient
PCHE-A-Air	86.4 ks (24 h)	620 K (350 °C)	Air, $p = 0.1$ MPa
PCHE-B-Air	3.6 ks (1 h)	1070 K (800 °C)	Air, $p = 0.1$ MPa
PCHE-B-Vac	3.6 ks (1 h)	1070 K (800 °C)	Vacuum, $p < 10$ Pa

water chemistry, this autoclave system simulated BWR normal water chemistry condition. Tensile bars were strained to failure at the strain rate of 1×10^{-6} s^{-1}. Control tests of non-treated and CSS-engineered Fe–Cr–Ni bars were conducted in air at ambient temperature and pressure. These tests were performed by Wei Niu at the University of Akron.

2.4.5 Irradiation Tests

The proton irradiation was generated using 3.2 MeV tandem accelerator. 1.5 MeV protons were used to produce a reasonably uniform dose ≈ 0.5 dpa within 12 μm below the surface of LTC IN-718. The dose was calculated using "Quick Calculation of Damage" option in SRIM (stopping and range of ions in matter) software developed by Ziegler,[51] which is based on the Kinchin-Pease formalism.[52] Profiles of predicted proton dose is presented in Figure 2.4. The proton irradiation test was conducted at 620 K for 86.4 ks (24 h). These tests were performed by our collaborators at LANL (Los Alamos National Laboratory).

2.4.6 Magnetism

AFM (atomic force microscopy)-MFM (magnetic force microscopy) was used to reveal the existence of any ferromagnetic phase after LTC or LTNC of IN-718. A Dimension 3100 (Veeco Digital Instruments by Bruker) AFM-MFM equipped with a Co-Coated Si tip was

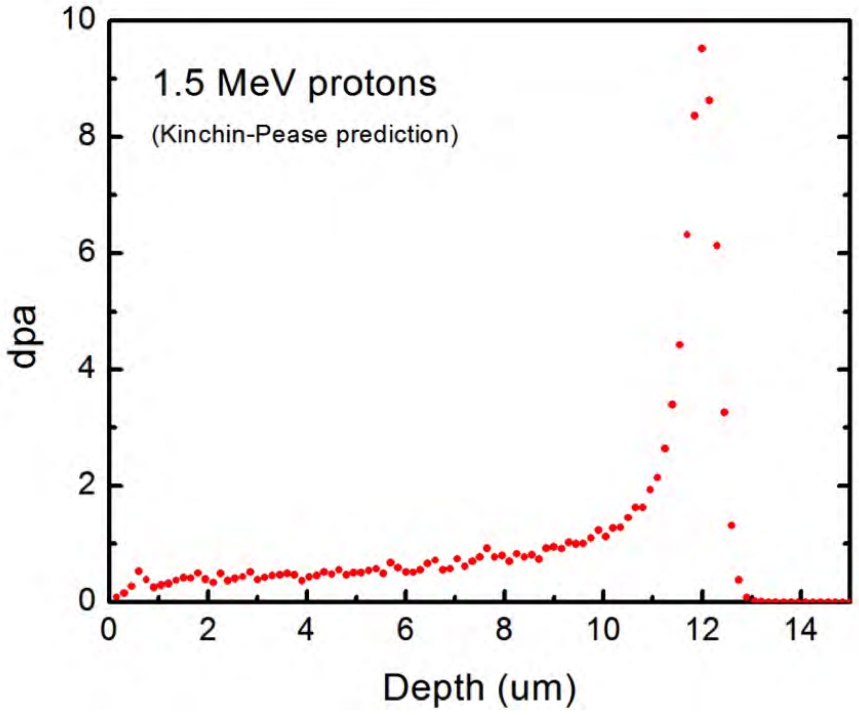

Figure 2.4. Dpa depth profile of 1.5 MeV protons into iron simulated by SRIM.

used to obtain the magnetic contrast. Scans in a non-contact mode were performed on cross-sectional samples after LTC and LTNC. Both topographic and phase images were obtained at the same time.

2.5 Oxidized and Irradiated LTC/LTNC Near-surface Region Characterization

2.5.1 SEM and TEM

The fracture surfaces of Fe–Cr–Ni alloys after tensile tests were studied by SEM (scanning electron microscopy) (Nova Nanolab 200, FEI).

TEM (transmission electron microscopy) specimens were prepared from oxidized and irradiated Fe–Cr–Ni alloys. FIB (focused ion beam)-SEM (Nova Nanolab 200, FEI) was used to prepare the TEM specimens. Specifically, Ga^+ was used to lift out a cuboid

with volume of $\approx 20\times10\times1.5$ μm^3. The lifted cuboid was then attached on a Cu grid by Pt welding. Subsequently, the cuboid was gradually thinned to TEM transparency using Ga^+ at voltages and currents of 30 kV and 1 nA, 30 kV and 0.3 nA, and 5 kV and 0.3 nA, respectively.

TEM studies of microstructures of carburized or nitro-carburized near-surface region after oxidation and irradiation tests were conducted using a Technai F30 ST transmission electron microscope (300 kV, FEI) with a point resolution of 0.2 nm and an information resolution limit of 0.14 nm. The XEDS (X-ray energy dispersive spectroscopy) system, combined with STEM (scanning transmission electron microscopy) nanoprobe that has a spatial resolution of about 2 nm, was used to study the elemental distribution in oxidized and irradiated near-surface zone.

3 Results

3.1 LTC/LTNC Near-surface Region Characterization

3.1.1 XRD

AISI-316L. Figure 3.1 presents the XRD patterns of non-treated and carburized AISI-316L coupons, respectively. The non-treated AISI-316L shows the characteristic peaks of FCC lattice, corresponding to the diffractions of {111} and {200} for 2θ at 50.8 °and 59.4 °(Co source), respectively. Based on the peak positions of {111} and {200}, the lattice parameter of a = 0.361 nm can be calculated, consistent with the data of Ge.[35] In

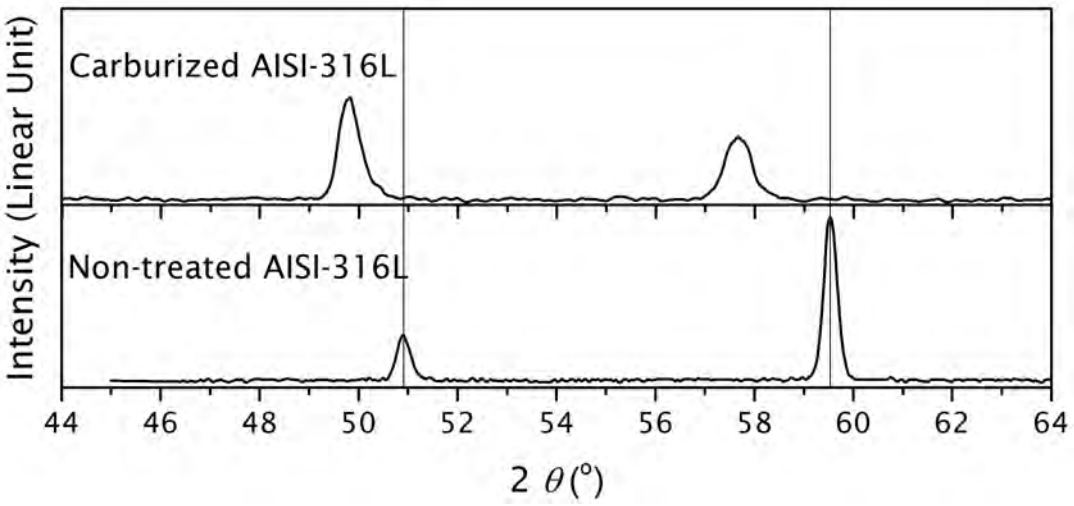

Figure 3.1. XRD patterns of non-treated and carburized AISI-316L tubes and coupons.

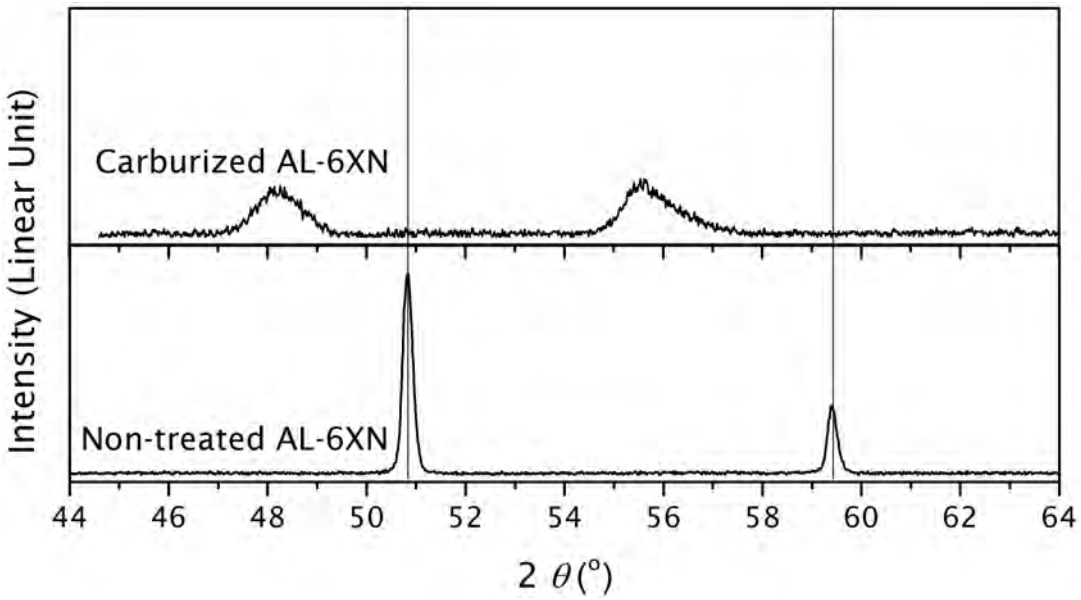

Figure 3.2. XRD patterns of non-treated and carburized AL-6XN.

addition, the lower {111} peak intensity than that of {200} in AISI-316L coupon suggests that strong texture exists on the surface of the coupon.

After LTC, the diffraction peak of AISI-316L shifts to lower angles. No extra peaks are shown in carburized AISI-316L coupons. The peak shifts toward lower angles correspond to an increase in the d-spacing of {111} and {200} lattice planes (i. e. an increase of FCC a). The combination of peak shifts and the absence of extra diffraction peaks indicate that carbon atoms occupy the interstitial sites, without forming carbides (< 5 vol% in the penetration depth 5 μm of the X-ray). Moreover, peak broadening has been observed in carburized AISI-316L compared to non-treated specimen.

AL-6XN. Figure 3.2 presents the XRD patterns of non-treated and carburized AL-6XN, respectively. The non-treated AL-6XN also shows the characteristic {111} and {200} peaks of an FCC lattice at 2θ = 50.8 °and 59.4 °(Co K_α), respectively. The peak positions are the

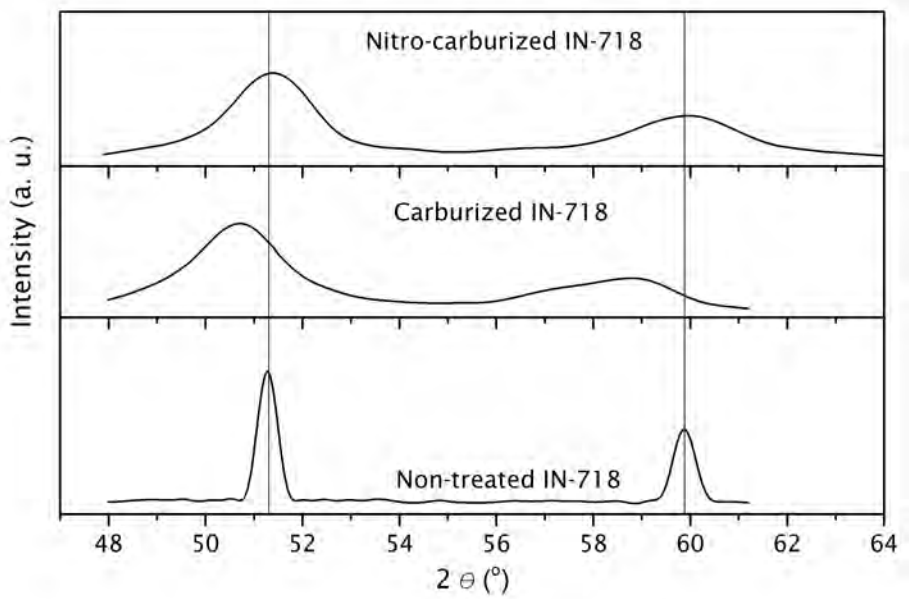

Figure 3.3. XRD patterns of non-treated, carburized, and nitro-carburized IN-718.

same as those of AISI-316L, suggesting that although the concentration between AISI-316L (≈ 69 at% Fe, 19 at% Cr, 10 at% Ni) and AL-6XN (≈ 43 at% Fe, 24 at% Cr, 25 at% Ni) (Table 1.1) is different, the lattice parameter a is similar.

After LTC, the diffraction peaks shift to lower angles, and no extra peaks are observed. This suggests that carbon atoms diffuse into AL-6XN, occupying the interstitial sites, instead of forming carbides. This is similar to the carburization of AISI-316L. Moreover, peaks broadening after LTC have also been observed in AL-6XN, with reasons similar to those of AISI-316L. The intensities of {111} and {200} peaks were similar after LTC, indicating the orientations of grains were changed after carburization. Possibly, recrystallization, which might be present in the LTC, caused the rotation of grains.

IN-718. Figure 3.3 presents the XRD patterns of non-treated, carburized, and nitro-carburized IN-718 samples, respectively. The non-treated IN-718 shows the characteristic {111} and {200} peaks of an FCC lattice at 2θ = 51.3 °and 59.9 °(Co K_α), respectively. Based on the peak positions of {111} and {200}, the lattice parameter of a = 0.358 nm can be calculated. The lattice parameter a of IN-718 is slightly lower than that of AISI-316L and AL-6XN.

After LTC, the diffraction peaks broaden and shift to lower angles. In addition, no extra peaks are observed. This indicates that carbon atoms diffuse into IN-718 and occupy the interstitial sites, instead of forming carbides. This is similar to carburized AISI-316L and AL-6XN. The broadening effect has the same reasons to that of AISI-316L and AL-6XN.

Different from LTC of austenitic stainless steels, the peaks of IN-718 after LTNC shift slightly to higher angles. Extra peaks are not detected, which means that carbides and nitrides do not form during the LTNC. In addition, diffraction peak broadening is also observed. Such broadening is probably due to the different carbon and nitrogen concentrations at different surface depths, leading to a continuous variation of lattice parameter a. The broadening can also be partially attributed to crystal defects (dislocations), which builds up at the nitro-carburized layer.

3.1.2 Metallography

Fe–Cr–Ni Coupons. Figure 3.4a and c present the metallographic cross-sections of CO carburized AISI-316L and IN-718 coupons after etching, respectively. Grain boundaries (dark lines) have been observed in the core regions of Fe–Cr–Ni alloys. On the surface, featureless white bands appear without any etching contrast, suggesting a better corrosion resistance to the etchant (volume ratio: HCl : HNO_3 : H_2O = 2 : 1 : 1) of surface layers than that of core regions. The etching time is 60 s, 90 s and 90 s for surface-engineered

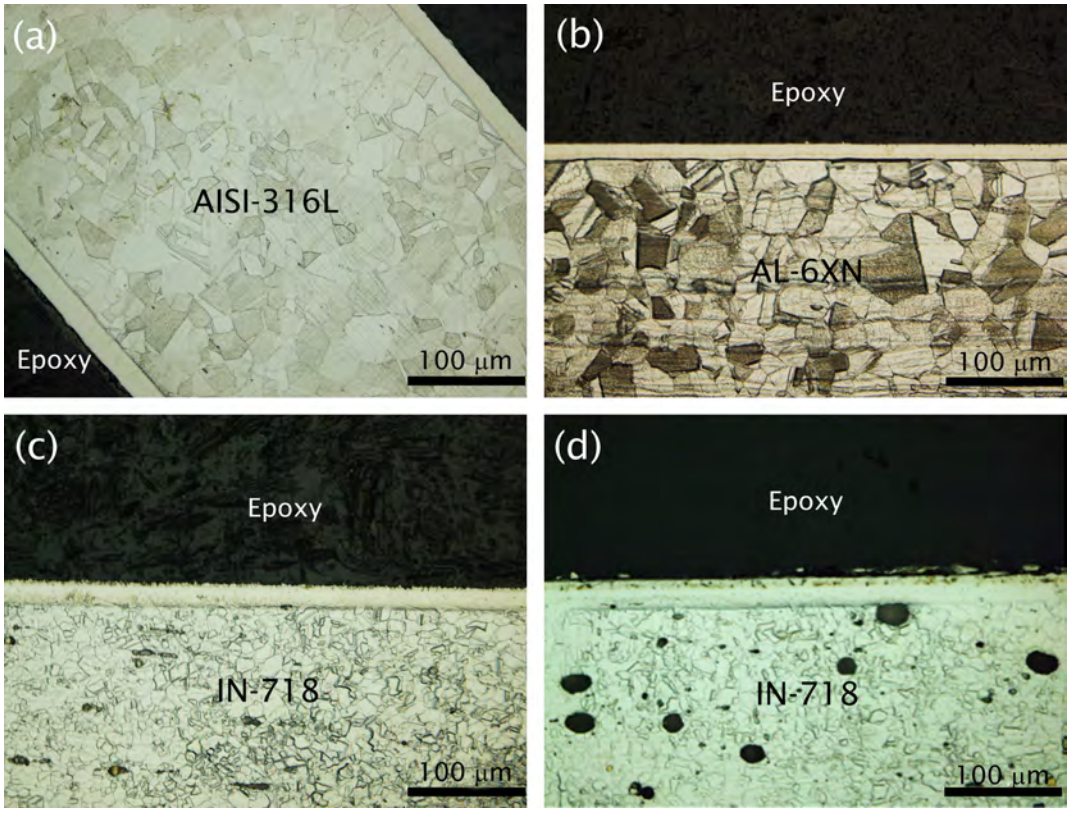

Figure 3.4. Metallographic cross-sections of (a) carburized AISI-316L, (b) carburized AL-6XN, (c) carburized IN-718, and (d) nitro-carburized coupons, respectively.

AISI-316L, AL-6XN and IN-718, respectively. In addition, all the etching experiments were conducted at room temperature (i. e. 300 K). The inner lines of the featureless white bands in carburized Fe–Cr–Ni alloys correspond to a cut-off carbon concentration (≈ 1 at%),[20,31] above which the layers cannot be etched by the etchant. Therefore, the thickness of the carburized near-surface zone is considered as the region where the carbon concentration is higher than the cut-off concentration, namely the thickness of the featureless band, as seen in Figure 3.4. Uniform carburized near-surface regions on both sides of coupons, with the thickness ≈ 20 µm, are observed for Fe–Cr–Ni alloys.

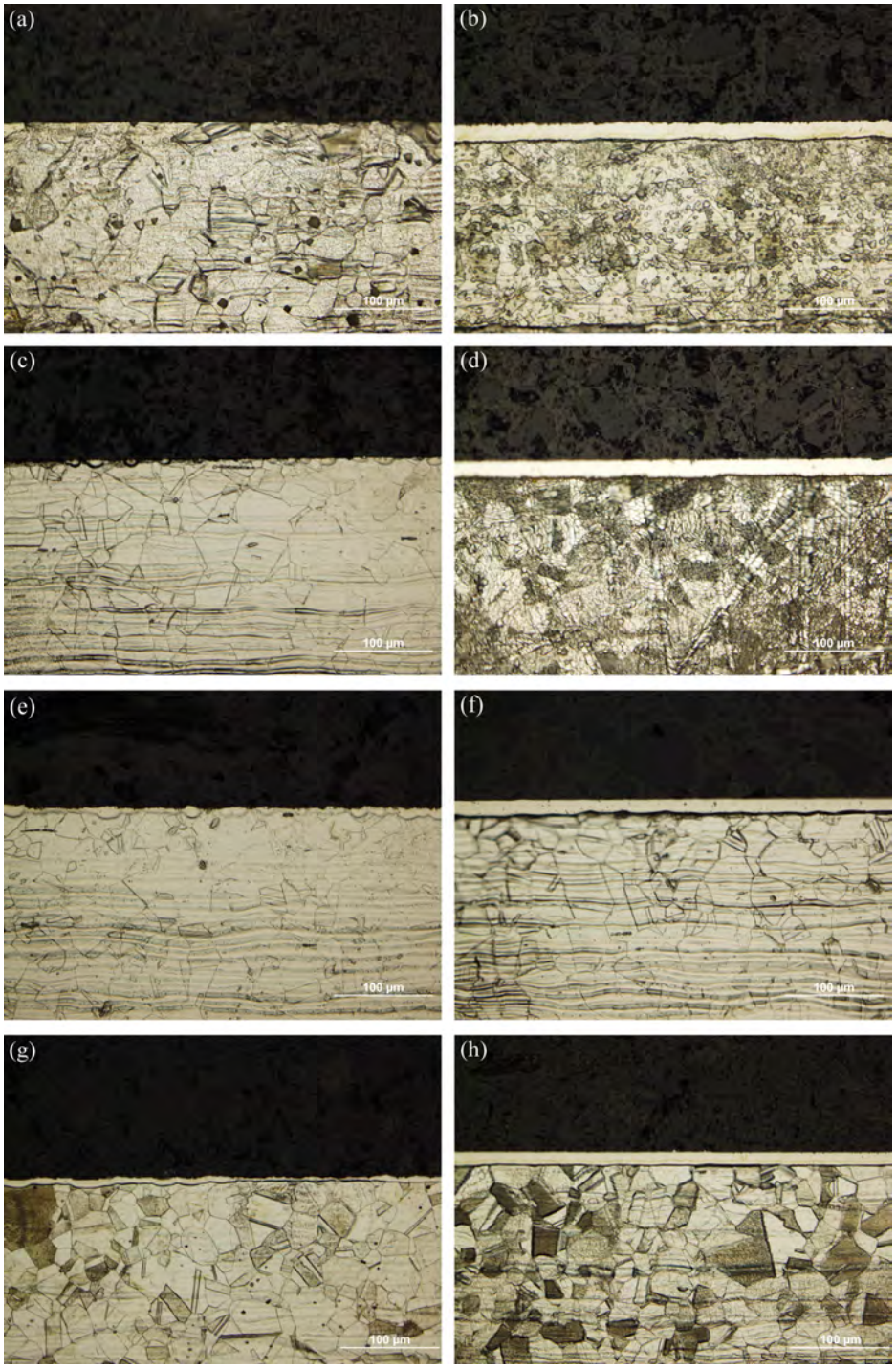

Figure 3.5. Metallographic cross-sections of carburized AL-6XN for different surface finishing and activation: (a), (c), (e), (g) are polishing with P180, P800, P4000, and electro-polishing, respectively. (b), (d), (f), (h) are polishing with the corresponding SiC grit papers and activating with aqueous HCl at room temperature for 300 s, respectively.

Figure 3.4b presents the metallographic cross-section of electropolished, aqueous HCl immersed, and C_2H_2 carburized AL-6XN coupon after etching. Similarly, grain boundaries in the core region, and uniform carburized layer on both surfaces with the thickness of ≈ 20 μm have been observed. Figure 3.5 shows the influence of surface finishes as well as room-temperature aqueous HCl activation on the carburized near-surface regions of AL-6XN. It can be seen in Figure 3.5a, c, e and g that the samples with finer surface finishes show thicker and more uniform carburized near-surface zone. However, the carburized near-surface region does not uniformly cover the surface of the electro-polished AL-6XN specimen after LTC. On the contrary, all the samples exposed to the AAA process show continuous and uniform carburized layer with thickness of ≈ 20 μm, no matter what surface finishes.

Figure 3.4d presents the metallographic cross-section of CO and NH_3 nitro-carburized IN-718 coupon after etching. Similarly, grain boundaries have been observed in the core region of IN-718. However, different from the carburized near-surface region, the nitro-carburized near-surface zone shows two bands. The outer band, with a thickness of ≈ 2 μm, shows etching contrast. The inner band, with a thickness of ≈ 18 μm, does not show etching contrast. The nature of the two bands will be further studied by SAM. In addition, uniform nitro-carburized near-surface regions on both sides of coupons are also observed for IN-718.

Fe–Cr–Ni Tubes. Figure 3.6a-b shows the metallographic cross-sections of a carburized AISI-316L tube. At the regions away from the two ends of the tube, the outer carburized near-surface zone is about 3 times thicker than inner region, as shown in Fig 3.6a. This difference is also observed by XRD in which the outer layer always shows larger peak shifts than that of the inner layer. However, at two ends of the tube, the outer and

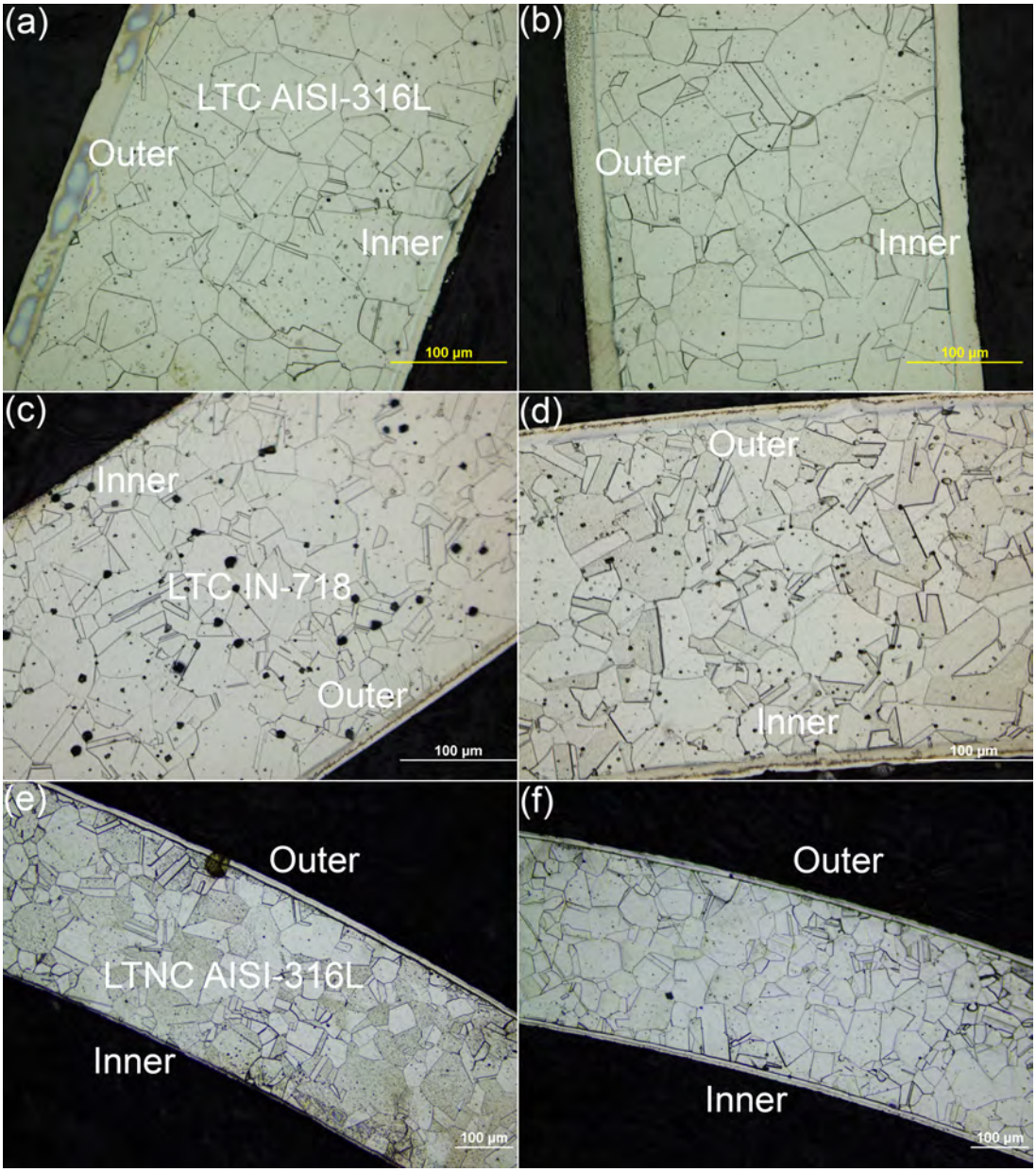

Figure 3.6. Metallographic cross-sections of LTC AND LTNC Fe–Cr–Ni alloy tubes. (a) Regions away from the two ends of the LTC AISI-316L tube. (b) A typical image of two ends of the LTC AISI-316L tube. (c) Regions away from the two ends of the LTC IN-718 tube. (d) A typical image of two ends of the LTC IN-718 tube. (e) Regions away from the two ends of the LTNC AISI-316L tube. (f) A typical image of two ends of the LTNC AISI-316L tube.

inner carburized layers have similar thicknesses, as shown in Fig 3.6b. Similar features have also been observed in carburized IN-718 and nitro-carburized AISI-316L tubes, as shown in Figure 3.6c-f.

Since nuclear fuel claddings are tubes, with dimensions similar to that of AISI-316L and IN-718 tubes, it is important to uniformly carburize and nitro-carburize the tubes. There are four hypotheses for the different thicknesses between outer and inner near-surface regions:

1. The different orientation of the tube relative to the gas flow direction in the furnace.
2. The different roughness of the inner and outer surfaces.
3. Less CO molecules and smaller carbon activity inside the tube than outside the tube.
4. The gas flow through the tube is smaller than outside the tube.

For the first hypothesis, two AISI-316L tubes were placed in the furnace for LTC horizontally and vertically. No difference of the thickness of the near-surface diffusion region between horizontally and vertically placed tubes was observed. Moreover, similar features, with thick outer carburized near-surface region and thin inner near-surface zone, have been observed in both tubes. Therefore, the orientation dose not cause significantly different thickness between inner and outer carburized near-surface zones.

For the second hypothesis, the outer and inner surface roughness of non-treated AISI-316L tubes were measured, and the average values are 16.6 RA and 22.5 RA, respectively. Subsequently, one tube was split in half along the long axis and then carburized. The outer and inner carburized near-surface region had the same thickness. Therefore, the influence of surface roughness could be ruled out.

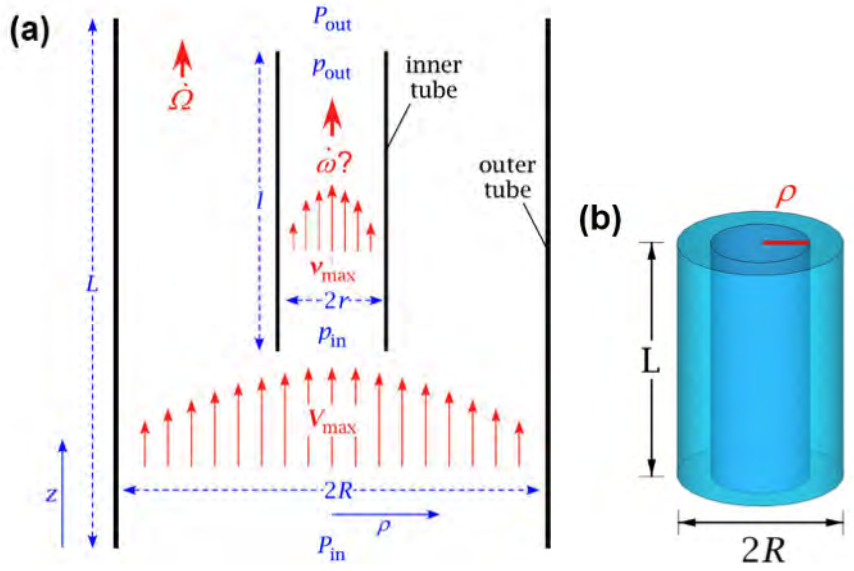

Figure 3.7. (a) Schematic diagram of gas flow through the AISI-316L tube. (b) Part of CVD furnace with diameter 2R and length L. (Prof. F. Ernst, unpublished)

For the third hypothesis, the carbon activity inside and outside the AISI-316L tubes was considered. The carburization reaction is shown in equation 1.3, and the carbon activity a_C can be calculated as

$$a_C = K\frac{P_{CO} \cdot P_{H_2}}{P_{H_2O}}, \tag{3.1}$$

where K is the equilibrium constant at the temperature of LTC. P_{CO}, P_{H_2}, and P_{H_2O} are partial pressure of CO, H_2 and H_2O, respectively, during LTC. Since the partial pressures of these gases are similar (if they are not the same) everywhere in the furnace, the carbon activities inside and outside the tubes should be very close (if not the same). Therefore, the third hypothesis is also excluded.

For the fourth hypothesis, the gas flow inside and outside the tube was considered. The effect of tube radius on the gas flow resistance can be described by the Hagen-Poiseuille law, which is based on the simplified assumption that laminar flow (gas layer) is 'sticking' to the walls. The following derivation and figures are from Prof. F. Ernst.

To estimate the gas flow through the AISI-316L tube, assuming that the gas-flow shown in Figure 3.7a is stationary, the pressure-induced force F_{p} must balance the friction force F_{f},

$$F_{\mathrm{p}} + F_{\mathrm{f}} = 0\,. \tag{3.2}$$

Considering the tube with radius ρ and length L, the pressure-induced force can be written as,

$$F_{\mathrm{p}} = \pi\rho^2 \cdot \Delta P\,, \tag{3.3}$$

where $\Delta P = P_{\mathrm{out}}$-$P_{\mathrm{in}}$. The friction force, F_{f}, is given as the product of viscosity η, cylindrical side area and velocity gradient,

$$F_{\mathrm{f}} = -2\pi\rho^2 \cdot L \cdot \eta \frac{dV[\rho]}{d\rho}\,, \tag{3.4}$$

and balance of forces implies,

$$\frac{dV[\rho]}{d\rho} = -\Delta P \frac{\rho}{2\eta L}\,. \tag{3.5}$$

Integration with the boundary condition $V[R] = 0$ to obtain integration constant yields the velocity profile,

$$V[\rho] = \frac{\Delta P}{4\eta L}(R^2 - \rho^2)\,. \tag{3.6}$$

The current through a hollow cylinder with radius ρ and infinitesimal wall thickness $d\rho$ is,

$$d\dot{\Omega} = 2\pi\rho V[\rho]\, d\rho\,. \tag{3.7}$$

Neglecting the influence of the small tube in the center, the total current through the outer tube is,

$$\dot{\Omega} = \int_0^R 2\pi\rho V[\rho]d\rho = \int_0^R 2\pi\rho\frac{\Delta P}{4\eta L}(R^2-\rho^2) = \pi\frac{\Delta P}{2\eta L}\int_0^R(\rho R^2-\rho^3)d\rho = \frac{\pi\Delta P}{8\eta L}R^4. \quad (3.8)$$

This relation is known as "Hagen-Poiseuille" law:

$$\dot{\Omega} = \frac{\pi\Delta P}{8\eta L}R^4. \quad (3.9)$$

Assuming a linear decrease of ΔP over the outer tube length L, the total current through the inner tube is,

$$\dot{\omega} = \frac{\pi\Delta p}{8\eta L}r^4, \quad (3.10)$$

where $\Delta p = \frac{l}{L}\Delta L$, so $\dot{\omega}$ can be written as,

$$\dot{\omega} = \frac{\pi\Delta P}{8\eta L}r^4. \quad (3.11)$$

For the ratio of currents through the inner and outer tube, this implies:

$$\frac{\dot{\omega}}{\dot{\Omega}} = \frac{r^4}{R^4}. \quad (3.12)$$

The diameter of the AISI-316L and IN-718 tube is around 10 mm and the diameter of the furnace chamber is around 200 mm. According to equation 3.12, the gas flow through the AISI-316L tube is ≈ 1/160,000 of the gas flow through the furnace chamber. Therefore, the HCl and CO gas flow through the tube is much less than around the outside of the tube. To verify the fourth hypothesis, the gas-flow through an AISI-316L tube was increased by inserting the tube into an upside-down funnel, shown in Fig 3.8a. The result shows that both inner and outer carburized near-surface regions have similar thicknesses, as shown in Fig 3.8b. Therefore, it can be concluded that the different

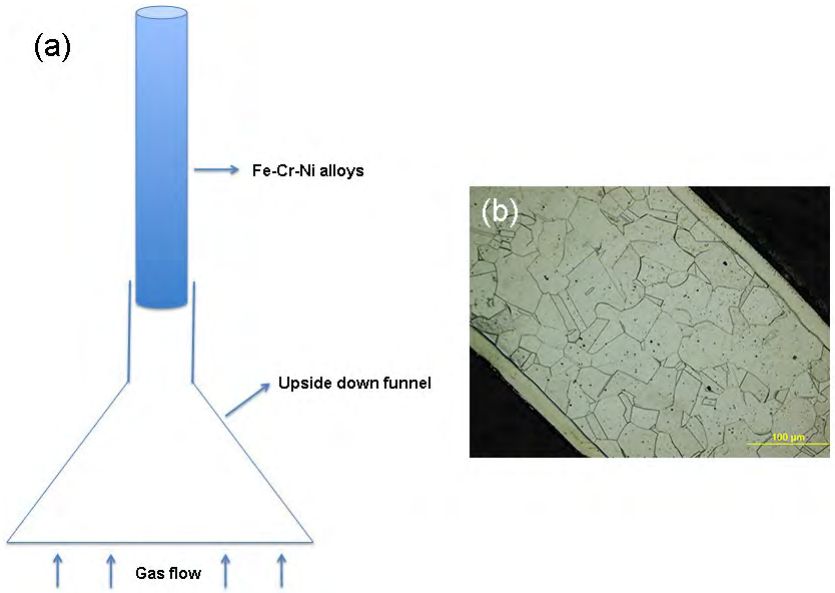

Figure 3.8. (a) Increasing gas-flow through the tube by using a funnel. (b) An optical image of a cross-section of a carburized AISI-316L tube by using the funnel.

depth between the outer and inner carburized near-surface zone is because the gas flow through the tube is smaller than outside the tube.

Moreover, further analysis confirmed which gas-flow, CO or HCl, dominates such phenomenon. The influence of CO gas-flow was considered. Assuming a uniform carbon concentration of 7.5 at% across the tube and a carburized near-surface region thickness of 20 µm, the total amount of carbon atoms in the volume of the carburized near-surface zone can be calculated as 5.8×10^{-2} mol, considering the tube dimensions in Table 2.2. This means that 5.8×10^{-2} mol CO gas is required to achieve such a near-surface region thickness. Since the CO concentration during LTC is 10 vol%, the required CO gas volume is 3.5×10^{-3} m^3 (3.5 L). During LTC, the total volume of CO gas injected into the carburizing furnace is 0.24 m^3 (240 L), which is much more than the required volume. This indicates that the different amount of CO gas-flow does not dominate the

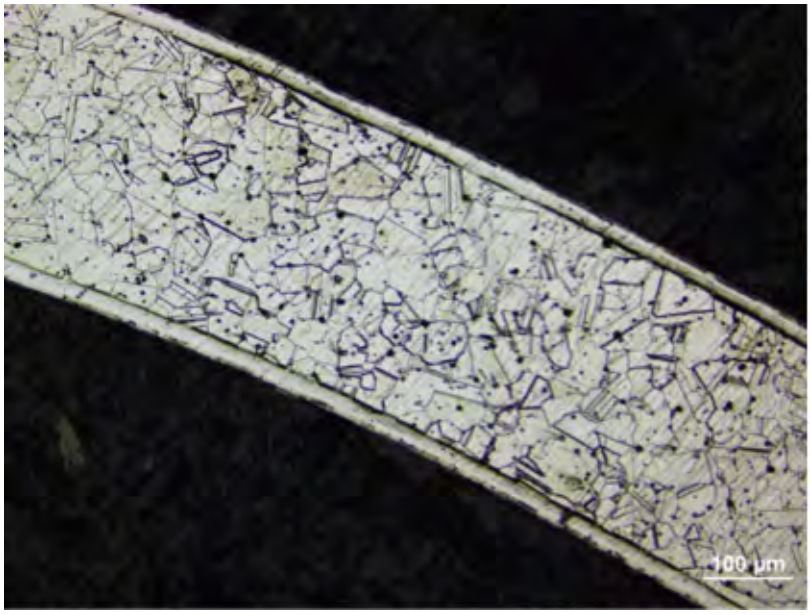

Figure 3.9. Metallographic cross-section of IN-718 tube after room-temperature aqueous HCl activation and LTNC.

phenomenon of different thickness between outer and inner carburized near-surface zones.

It can then be inferred that the different gas-flows of HCl are the dominant factor. This suggests that the activation efficiency of gaseous HCl is low. An activation that lasted 14.4 ks (4 h) is still not enough to fully remove the Cr_2O_3 layer (1 – 4 nm thick) [53–55] on the inner surface of the tube, considering the small flow of HCl through the tube. Similar thicknesses for the inner and outer carburized or nitro-carburized near-surface regions for both AISI-316L and IN-718 tubes can be achieved without inserting these tubes into an upside-down funnel during the LTC and LTNC treatment if they are exposed to the AAA process prior to surface-engineering. Figure 3.9 shows the cross-section of IN-718 tube after immersing in HCl for 600 s and LTNC. Both inner and outer surfaces contain a uniform nitro-carburized near-surface diffusion region with the thickness of ≈ 20 µm.

3.1.3 AAA

It has been found that surface activation with HCl gas does not always properly activate the surface of the tubes because of limited gas flow in the tube interior. Therefore, the tubes were immersed into aqueous HCl prior to the LTC. The immersion in aqueous HCl dramatically improved the success of the CSS-engineering process.

Encouraged by these results, it is speculated that the activation step with HCl gas may not be needed at all if the specimens were immersed in aqueous HCl solution prior to loading them into the furnace. If the main barrier to inward diffusion of carbon or nitrogen were the passivating Cr-rich oxide layer on the alloy surface, it has been expected that there is enough time for this layer to re-form before carburization can be started. However, the pending patent[56] implied that AISI-316L can be activated by this aqueous HCl activation method and later, successfully carburized with exposure in a CO, N_2 and H_2 containing environment at 720 K. Temporary prevention of oxidation happens when Si is dipped into aqueous HF solution.[57,58] In that case, a passivating layer of hydrogen forms on the surface protecting it against the formation of SiO_2 for a short period of time. This suggested that it is possible that the surface of AISI-316L and AL-6XN samples can be passivated after being immersed in an aqueous HCl solution and the subsequent cleaning procedure. This passive layer of unknown composition was later removed by heating, leaving a fully activated surface. Possibly, immersion in aqueous HCl solution passivates the surface against immediate oxidation for a limited amount of time, which is sufficient to transfer the specimens into the furnace and start the carburization process. Another possibility is that it is actually not the passivating surface oxide that constitutes the main barrier against low-temperature carburization, but the layer of poor

Air / Rinse	0.12 ks	18 ks	36 ks
Ethanol 0.3 ks	70%	17%	17%
Water 0.3 ks	17%	8%	12%
As-received	4%		

Figure 3.10. Metallic signals acquired by XPS.[56]

crystallinity generated by surface machining, which may be effectively removed by the liquid HCl.

XPS. After the aqueous HCl activation process, two AISI-316L specimens were immersed in water and ethanol for 300 s and exposed in air for 120 s. XPS data, as shown in Figure 3.10, implied that for the specimen immersed in ethanol, over 70% of its surface is covered with metallic element (Cr). However, for the one immersed in water, there is only 17% of the surface covered with elemental metal.

Figure 3.11 showed the binding energy of metal Cr (574 eV) and Cr^{3+} (576 eV) on the surface of activated surface of AISI-316L. Figure 3.11a suggested the surface was mostly covered by metal Cr. However, Figure 3.11b showed that Cr^{3+} (Cr oxide) occupied the most part of the surface.

Figure 3.11a indicated that immersing in ethanol after the AAA will delay the repassivation of the activated surface of AISI-316L, while Figure 3.11b suggested that immersing in deionized water would not protect the activated surface of AISI-316L.

The experimental data suggested that neither of the above assumptions are correct. Aqueous HCl activation worked well for AISI-316L because the formation of a Cr_2O_3-rich film on AISI-316L was delayed by immersing in ethanol. Accordingly, the re-passivation

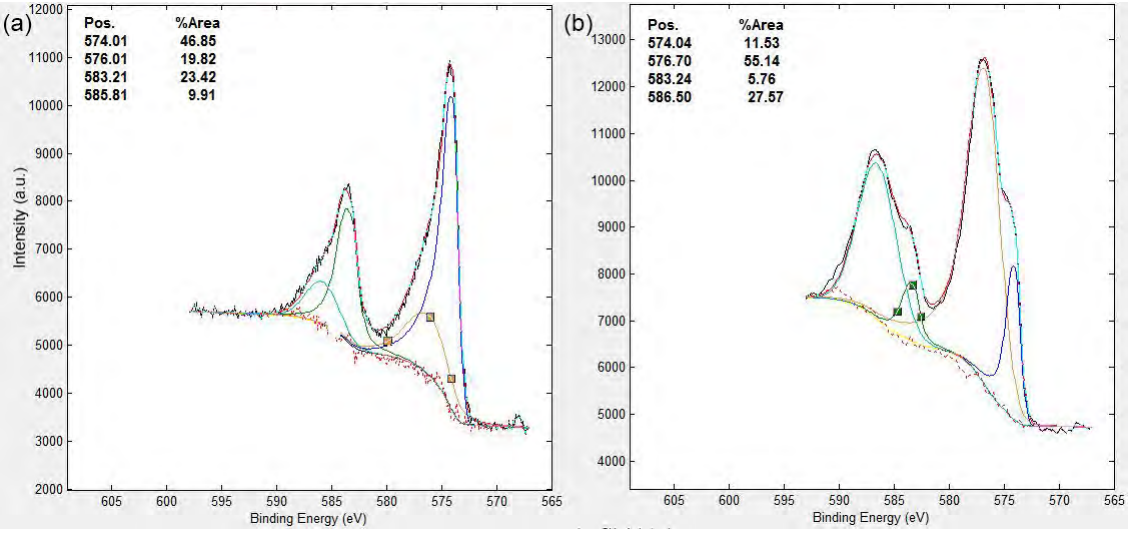

Figure 3.11. XPS data collected from the activated surface of AISI-316L: (a) immersed in ethanol for 300 s after AAA and (b) immersed in deionized water for 300 s after AAA.

is significantly retarded for the specimen immersed in ethanol compared to the specimen immersed in water. Two possible models were established in the 'Discussion' section to explain why immersing in ethanol could protect the activated surface of Fe–Cr–Ni alloys.

3.1.4 SAM Results

Case depth does not contain solute fraction information. Although Figure 3.12c and d show that the depth of the carbon-rich region of both LTC and LTNC IN-718 are around 20 μm, it is clear that a larger carbon fraction is detected in LTNC IN-718 than that in LTC IN-718. To include carbon fraction information in the case depth, the mean solute depth $\overline{z}$,

$$\overline{z} := \frac{\int z X_z \mathrm{d}z}{\int X_z \mathrm{d}z}, \tag{3.13}$$

is defined, where z is the depth and X_z is the solute fraction.

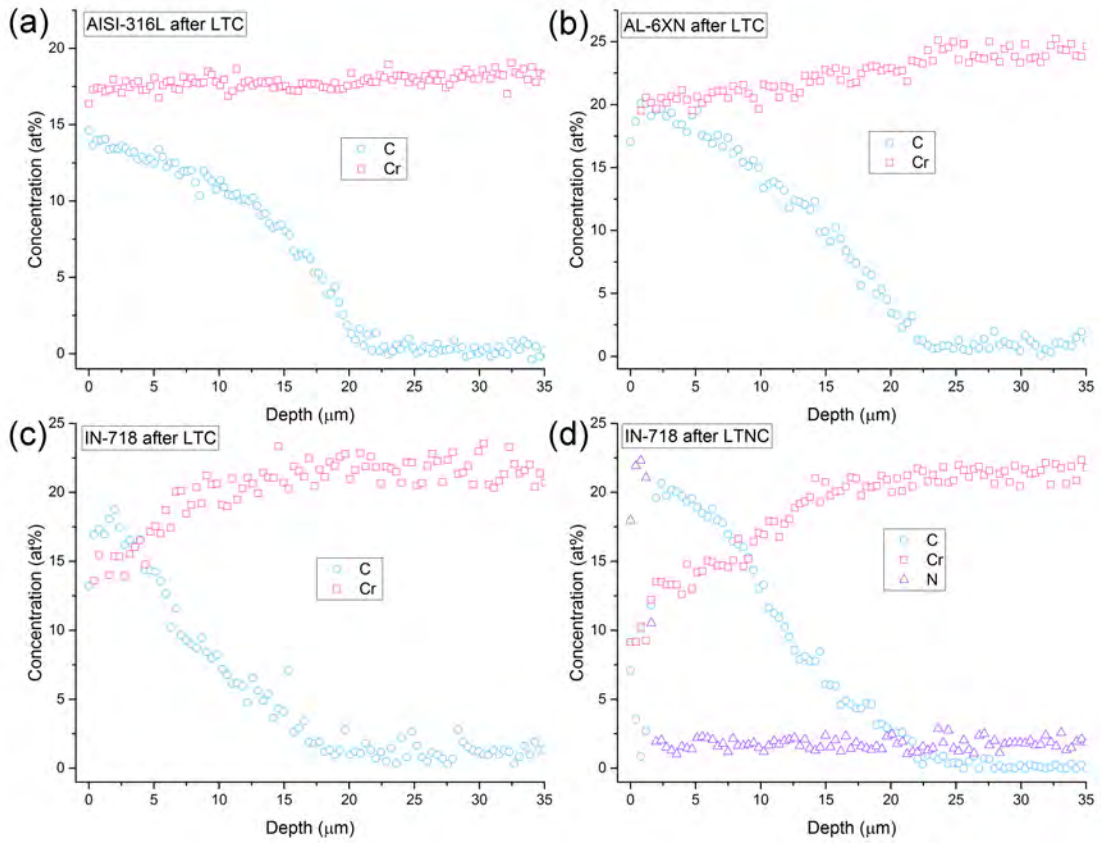

Figure 3.12. SAM elemental concentration depth profiles of (a) AISI-316L after LTC, (b) AL-6XN after LTC, (C) IN-718 after LTC, and (d) IN-718 after LTNC, respectively.

Figure 3.12a and b are the carbon concentration depth profiles on the cross-sections of AISI-316L and AL-6XN samples after LTC. The depths of carburized near-surface region in AISI-316L and AL-6XN are around 20 μm ($\overline{z}_C$ = 9 μm) and 22 μm ($\overline{z}_C$ = 11 μm), which are comparable to the white band thicknesses shown in the metallographic images in Figure 3.4a and b. The carbon concentrations at the outermost surface are about 16 at% and 20 at% for AISI-316L and AL-6XN samples, respectively. When the carbon activities are around 1 during the LTC of Fe–Cr–Ni alloys, such carbon concentrations are the maximum carbon concentrations (at certain temperature and carburizing time) that

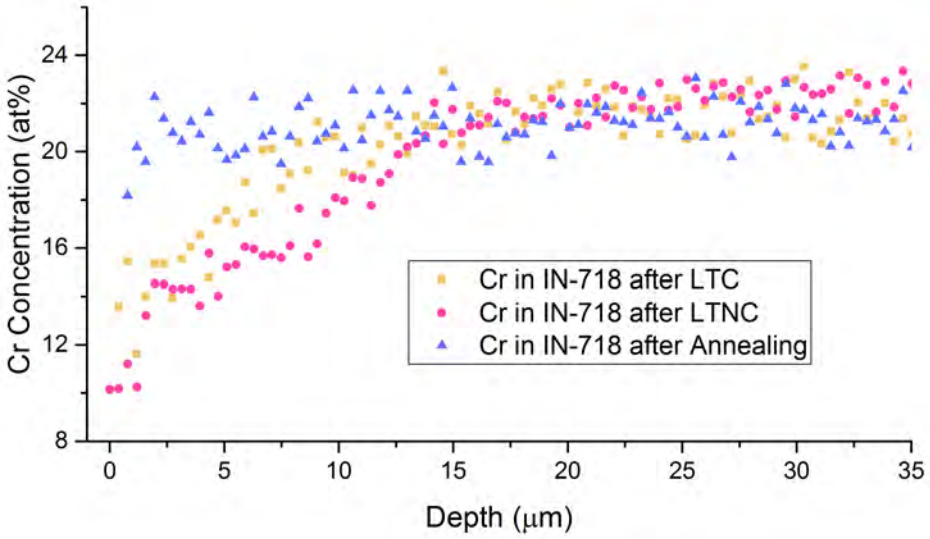

Figure 3.13. SAM Cr concentration depth profiles of IN-718 after LTC, LTNC, and annealing at carburization or nitro-carburization temperature under 0.1 MPa N_2 condition, respectively.

can be achieved at the surface of AISI-316L and AL-6XN, respectively. The carbon concentration gradually decreases until reaching the core regions. Comparing to AISI-316L, the carbon concentrations in AL-6XN dropped faster. In addition, the Cr concentrations in AISI-316L is slightly depleted (around $1-2$ at% lower while compared to that of core area) across the carburized near-surface zone. On the other hand, Cr depletion (5 at% less than that of the matrix) can be clearly seen in the carburized region of AL-6XN.

Figure 3.12c are the carbon and Cr concentration depth profiles on the cross-section of IN-718 sample after LTC. The depth of carburized near-surface region is also around 20 μm ($\overline{z}_C$ = 10 μm), which is consistent with the metallographic observation shown in Fig 3.4c. The carbon concentration at the outermost surface is about 18 at%. Similarly, such concentration is the maximum carbon concentration that can be achieved in IN-718 while the carbon activity is around 1 during the LTC. Inside IN-718, carbon concentration gradually decreases, with an even faster decreasing rate than that of AISI-316L

and AL-6XN. Moreover, Cr depletion is observed in the carburized near-surface zone after LTC. In the core region, Cr concentration is about 21 at%, while at the outermost surface, Cr concentration decreases to about 12 at%.

Figure 3.12d are carbon, nitrogen, and Cr concentration depth profiles on the cross-section of IN-718 sample after LTNC. The nitrogen atoms are present in the first 3 μm ($\overline{z}_N$ = 1 μm) thick region, with the concentration of about 20 at%, while the carbon concentration in such region is very low. This region corresponds to the outer band observed in the metallographic image shown in Fig 3.4d. Beyond the 3 μm thick region, nitrogen concentration drops rapidly to zero, and the carbon concentration increses dramatically to about 18 at%. The carbon-rich and nitrogen-poor region is around 20 μm ($\overline{z}_C$ = 11 μm) thick. The carbon concentration then gradually decreases with increasing depth, similar to the carbon concentration profiles of Fe–Cr–Ni after LTC. This region corresponds to the inner band observed in Fig 3.4d. Therefore, it is concluded that the nitro-carburized near-surface region contains two zones: an outer zone, which is mainly composed of interstitial nitrogen atoms, and an inner zone, which is mainly composed of interstitial carbon atoms. Moreover, Cr depletion is also observed in the nitro-carburized near-surface region after LTNC, and Cr is depleted more during nitro-carburization than carburization of IN-718, as seen in Fig 3.13. This might be because nitriding can also cause Cr depletion by forming some kind of volatile products containing Cr atoms. The X-ray diffraction peaks shift to higher angles for IN-718 after LTNC is probably due to the significant Cr depletion, since the Cr atom radius (139 pm) is larger than that of Fe (132 pm) and Ni (124 pm). That is, the lattice parameter expansion introduced by interstitial nitrogen and carbon cannot compensate the lattice parameter contraction resulted from Cr depletion. In carburized IN-718, however, Cr depletion is

also observed, lattice contraction is not observed. This means that the interstitial carbon concentration is high enough to compensate the lattice contraction effect of Cr depletion.

To further understand the phenomenon of Cr depletion during LTC and LTNC of IN-718, IN-718 specimen is annealed at the temperature of LTC process with the protection of N_2. One important thing that needs to be pointed out is that nitrogen is not capable of diffusing into IN-718 under the N_2 protecting atmosphere. The Cr concentration depth profile is shown in Fig 3.13. Under this condition, there is no Cr depletion detected. How the Cr fraction affects the lattice parameter of IN-718 will be fully discussed in the 'Discussion' section.

3.2 Properties of LTC and LTNC Layers

3.2.1 Mechanical Properties of Fe–Cr–Ni Alloys after LTC/LTNC

Nano-hardness. Figure 3.14 shows the hardness depth profiles of AISI-316L after LTC, IN-718 after LTCand IN-718 after LTNC. Accordingly, the hardness ($\approx$ 12 GPa, 16 GPa, and 14 GPa, respectively) at the outermost layers are more than three times higher than the non-treated core ($\approx$ 3 GPa, 5 GPa, and 5 GPa, respectively). Similar hardness profiles, corresponding to carbon and nitrogen concentration profiles, have been observed in the carburized and nitro-carburized layer. This suggests that the more carbon or nitrogen solutes located in the interstitial sites of Fe–Cr–Ni alloys, the harder the carburized or nitro-carburized layer.

Tensile Strength. Figure 3.15a shows the engineering stress versus strain profiles of non-treated, annealed, and carburized AISI-316L tubes. AISI-316L has the yield strength, σ_y, (at 0.2 % strain ε) of 0.23 GPa, the ultimate tensile strength, σ_f, of 0.61 GPa, and the strain

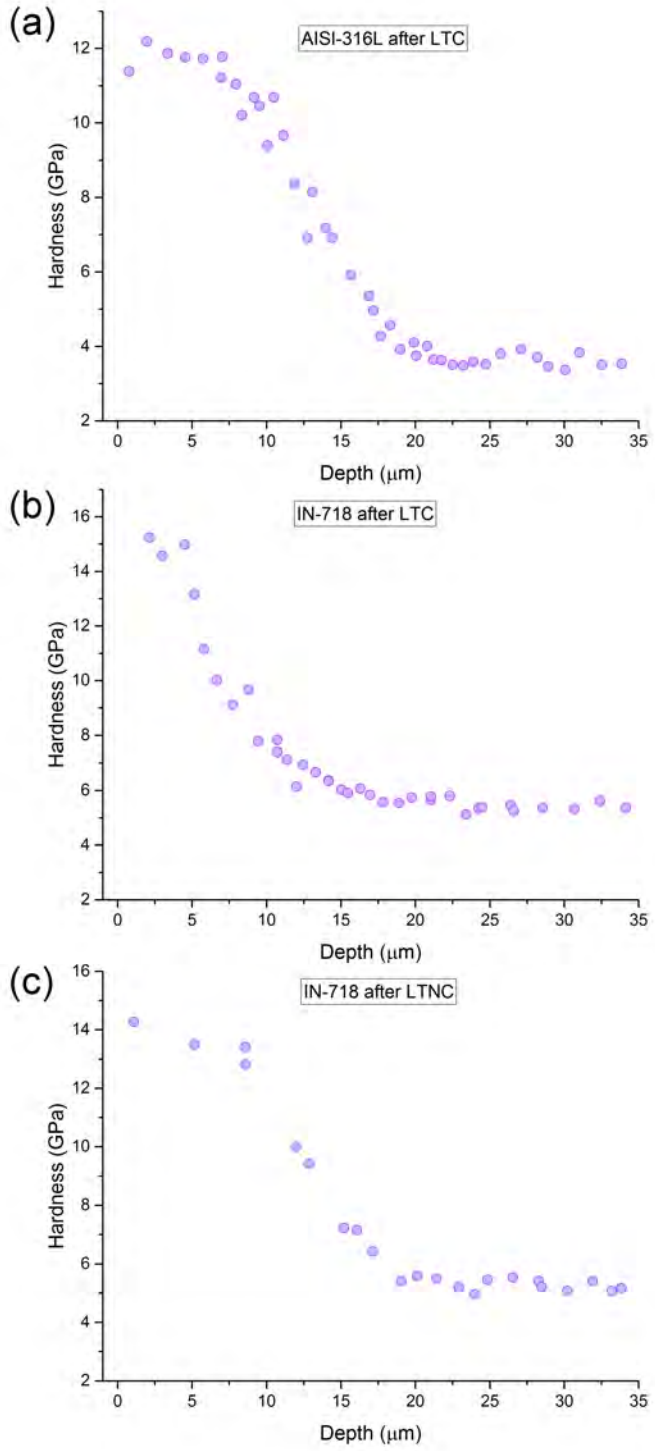

Figure 3.14. Nano-hardness depth profiles of (a) AISI-316L after LTC, (b) IN-718 after LTC, and (c) IN-718 after LTNC, respectively.

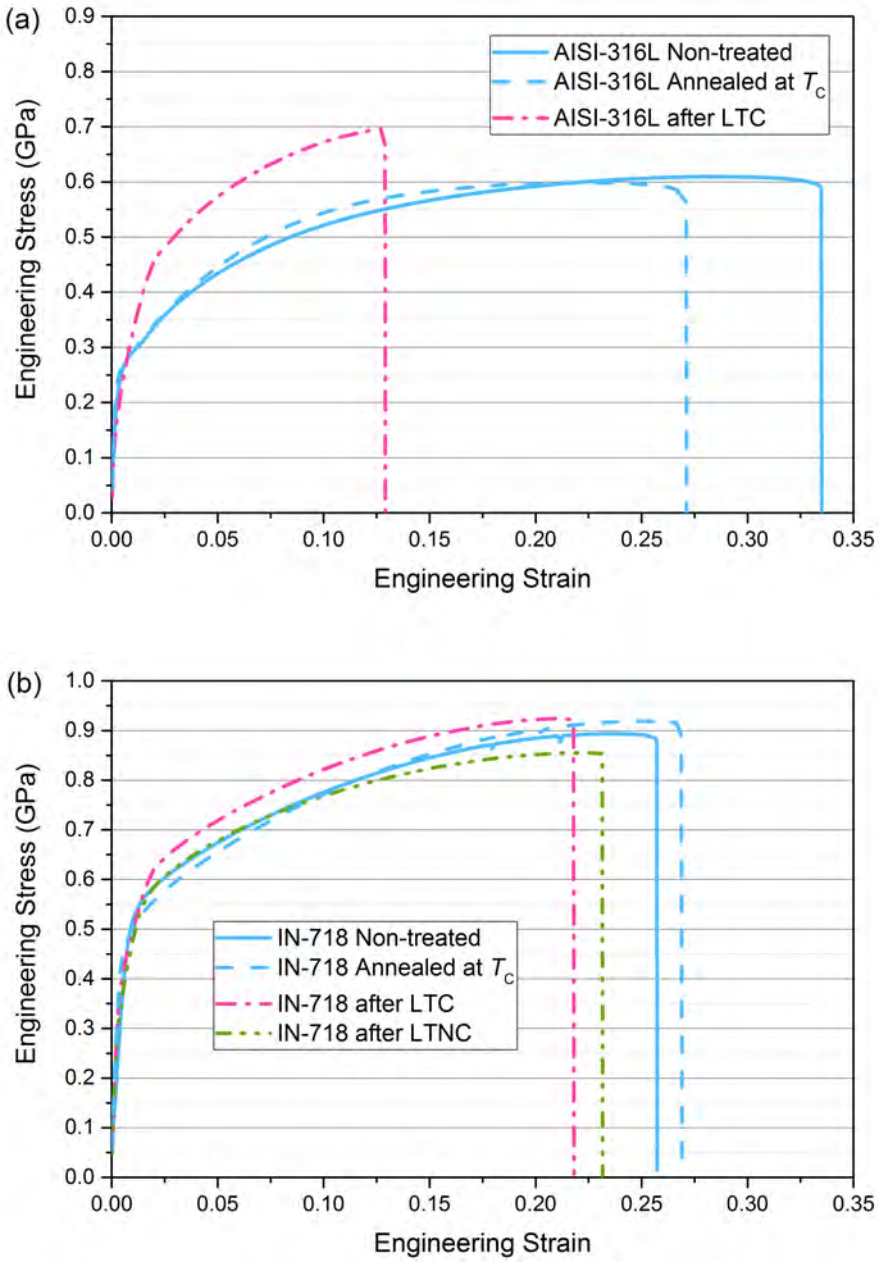

Figure 3.15. Tensile tests of (a) Non-treated, annealed at carburization temperature (720 K) for 72 ks (20 h), and carburized AISI-316L tubes, (b) Non-treated, annealed at carburization temperature for 100.8 ks (28 h), carburized and nitro-carburized IN-718 tubes.

to failure, ε_f, of 0.33. After annealing at carburization temperature T_C (T_C = 720 K) for 72 ks (20 h), σ_y increases to 0.26 GPa, while σ_f slightly decreases to 0.6 GPa. ε_f drops to 0.27. After LTC, σ_y and σ_f increase to 0.28 GPa and 0.7 GPa, respectively, while ε_f decreased to 0.13.

Figure 3.15b presents the engineering stress versus strain profiles of non-treated, annealed, carburized and nitro-carburized IN-718 tubes. IN-718 has σ_y of 0.49 GPa, σ_f of 0.9 GPa, and ε_f of 0.26. Compared to non-treated AISI-316L, non-treated IN-718 possesses 0.3 GPa higher tensile strength. After annealing at carburization/nitro-carburization temperature, T_C (T_C = 783 K), for 100.8 ks (28 h), σ_y decreases to 0.46 GPa, while σ_f and ε_f increases to 0.92 GPa and 0.27, respectively. After LTC, σ_y and ε_f decrease to 0.42 GPa and 0.22, respectively. However, σ_f remains at 0.92 GPa. Compared to carburized AISI-316L, carburized IN-718 possesses 0.2 GPa higher tensile strength and better strain to failure (0.22 compared to 0.12). After LTNC, σ_y and ε_f decrease to 0.36 GPa and 0.23, respectively. Different from carburized IN-718, nitro-carburized IN-718 shows a σ_f of 0.85 GPa, which is lower than that of non-treated IN-718 specimen.

Wear Resistance. Linear trenches were produced on the surfaces of non-treated and carburized AISI-316L coupons during the wear tests, as shown in Fig 3.16. The trench is narrower and much shallower for carburized AISI-316L (width: 0.25 mm, depth: 2 μm) than for the non-treated sample (width: 1.2 mm, depth: 40 μm). The volume (2.4×10^{14} μm^3) of the wear scar on the surface of carburized AISI-316L sample is around 100 times larger than that (0.3×10^{13} μm^3) on the surface of non-treated AISI-316L specimen. The wear resistance of AISI-316L is significantly enhanced after LTC.

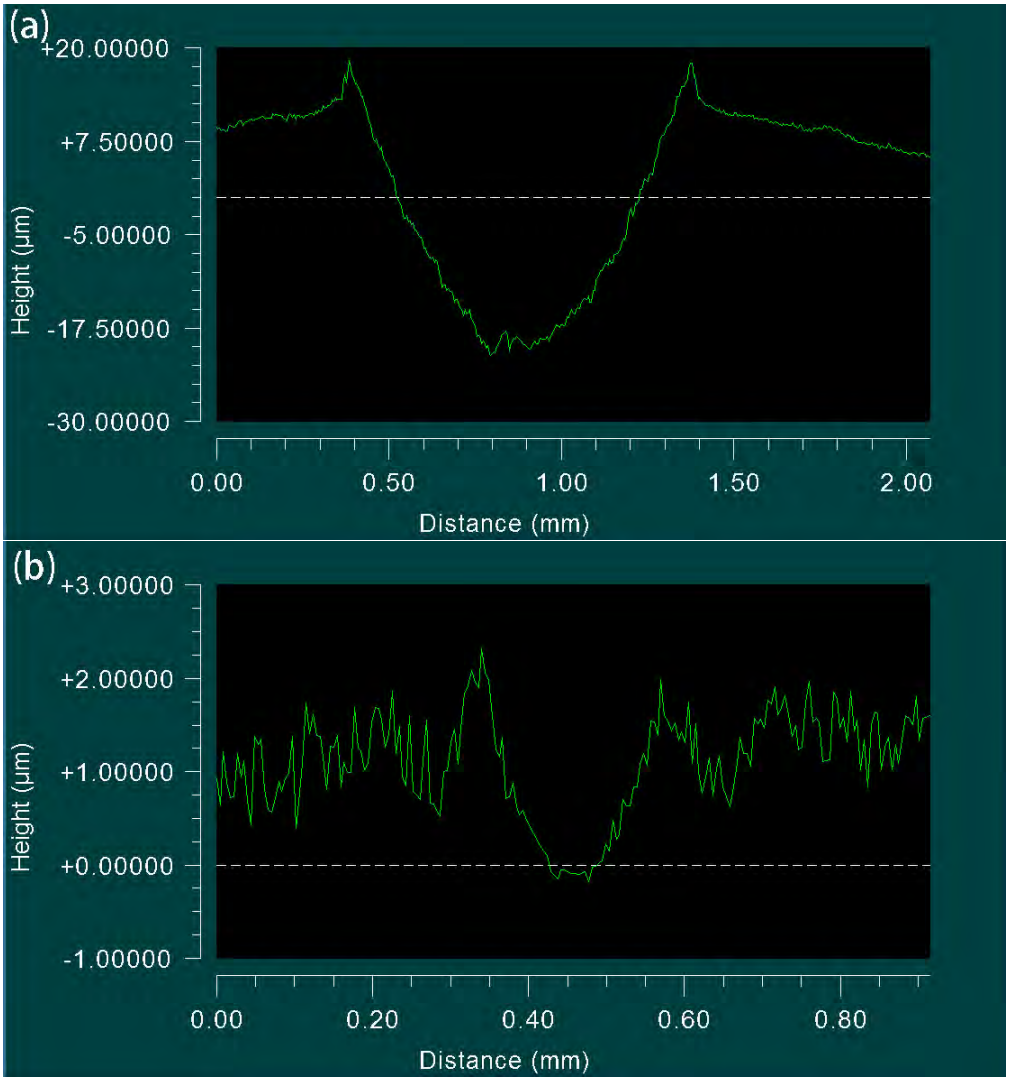

Figure 3.16. Wear trench profiles of (a) non-treated and (b) carburized AISI-316L coupons.

3.2.2 Ferromagnetism of IN-718 after LTC/LTNC

After LTC and LTNC, IN-718 can be attracted to a ferromagnet, indicating that paramagnetic IN-718 specimens show ferromagnetism after LTC and LTNC. The left side of Figure 3.17a is the AFM image. The bright part is the cross-section of carburized IN-718 and the dark side is the epoxy mount. The MFM image is on the right side of Figure 3.17b.

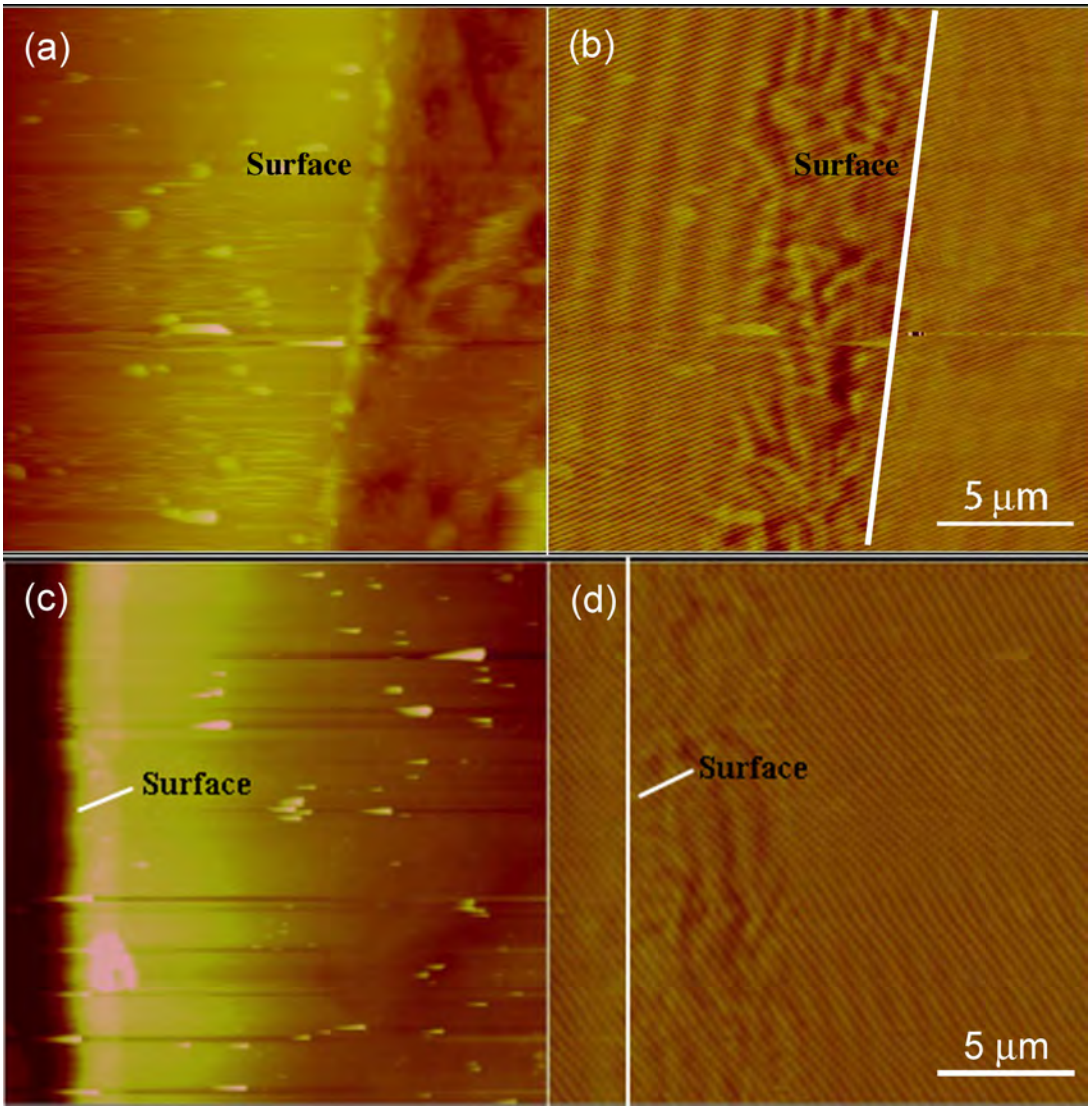

Figure 3.17. MFM data of (a) and (b) carburized IN-718, (c) and (d) nitro-carburized IN-718.

Ferro-magnetism was detected in the first five micrometers of carburized IN-718, as indicated in the MFM image.

A cross-sectional AFM image of low-temperature nitro-carburized IN-718 is seen on the left side of Figure 3.17c. The surface of the IN-718 sample can be clearly seen under AFM. On the right side of Figure 3.17d, ferromagnetism is detected under the surface. As seen in Figure 3.17d, ferromagnetism showed up in the first 7 μm after nitro-carburization. The reason for the ferromagnetism of IN-718 after surface-engineering will be discussed in the 'Discussion' section.

3.2.3 Oxidation Tests

PCHE-A-Air (annealing at 620 K in air for 86.4 ks). The working temperature of BWR is close to 620 K. In order to study the behaviors of CSS-engineered Fe–Cr–Ni alloys under the working temperature, these alloys have been exposed at 620 K in air for 86.4 ks, denoted as PCHE-A-Air. The carburized and nitro-carburized near-surface region after the annealing were then characterized by XRD, metallography, SAM and nano-hardness measurements.

1 XRD

Figure 3.18a are XRD patterns of non-treated, carburized, and PCHE-A-Air treated (annealing at 620 K in air for 86.4 ks) AISI-316L, respectively. Compared to carburized AISI-316L, position and width of FCC {111} and {200} peaks of PCHE-A-Air treated AISI-316L did not change. The lattice parameter of carburized AISI-316L did not significantly change. In addition, there are no extra peaks detected by XRD, implying that no oxides or carbides form during the annealing process. Similarly, the positions and widths of FCC {111} and {200} peaks are not significantly different between carburized/nitro-carburized and PCHE-A-Air treated AL-6XN and IN-718, as seen in Fig 3.18b-d, respectively. Moreover, extra peaks are not detected in these samples.

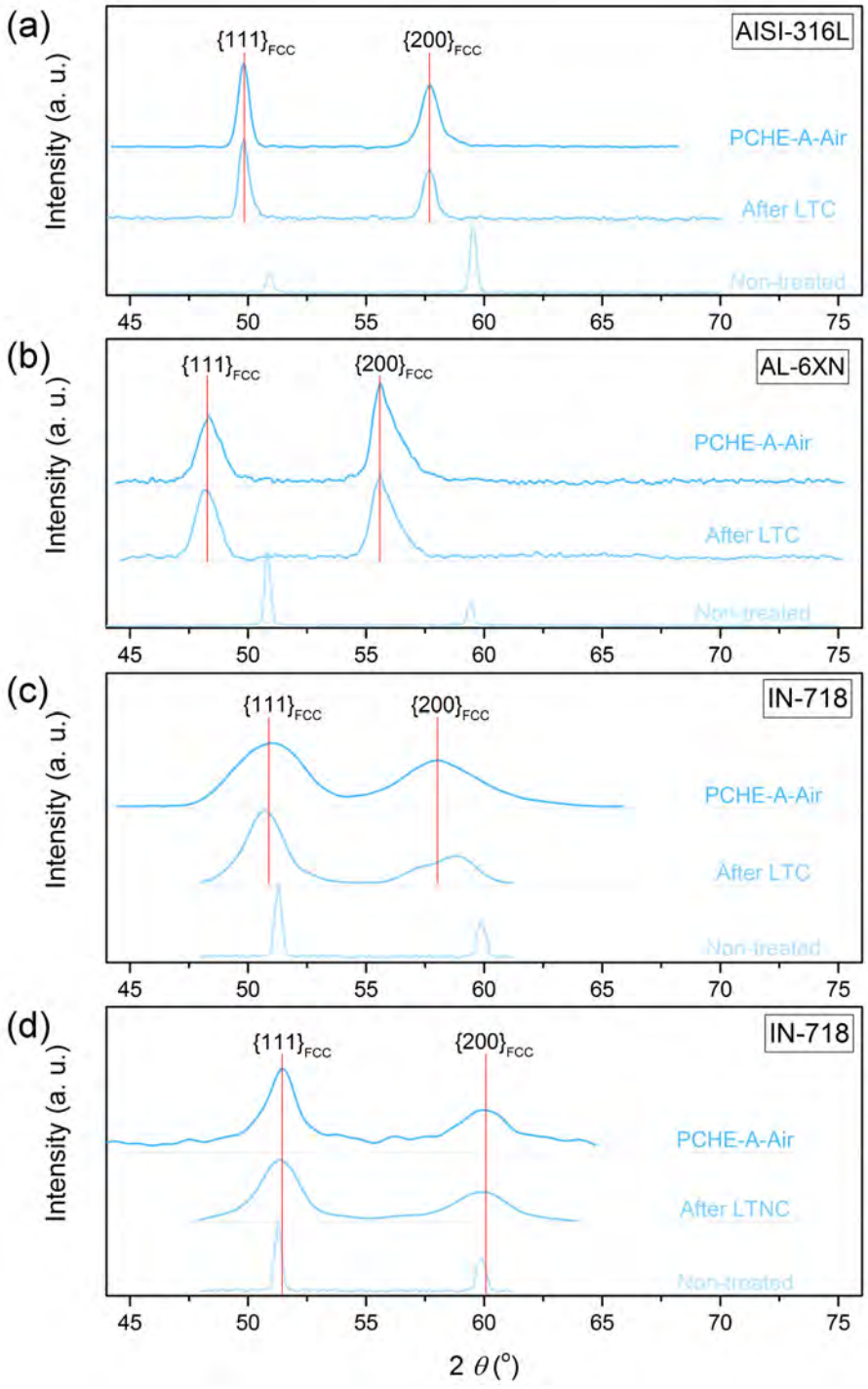

Figure 3.18. X-ray diffractograms of (a) carburized AISI-316L, (b) carburized AL-6XN, (c) carburized IN-718, and (d) nitro-carburized IN-718, respectively, before and after PCHE-A-Air.

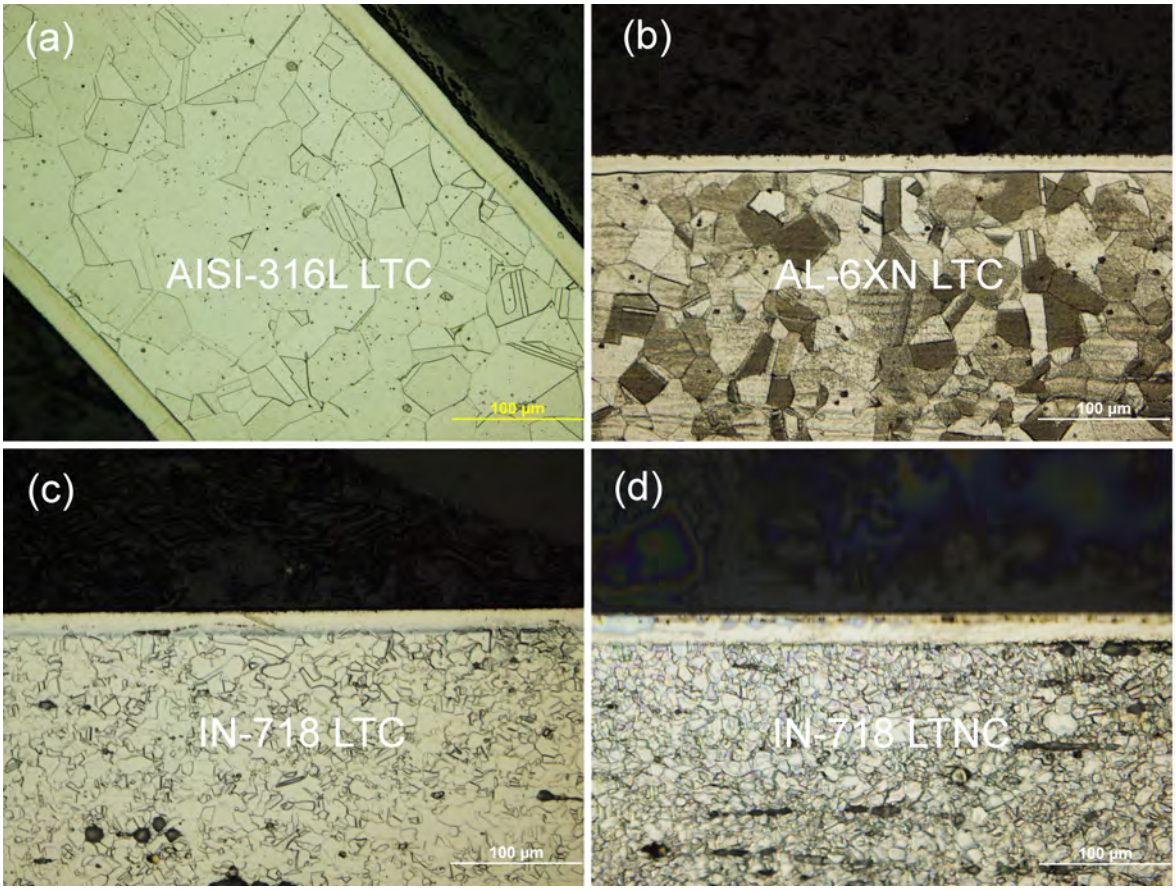

Figure 3.19. Metallographic cross-sections of (a) carburized AISI-316L, (b) carburized AL-6XN, (c) carburized IN-718, and (d) nitro-carburized IN-718, respectively, before and after PCHE-A-Air.

Therefore, the carburized near-surface zones of AISI-316L, AL-6XN, IN-718, and the nitro-carburized near-surface region of IN-718 do not involve phase changes under the exposure of BWR working temperature in air for 86.4 ks. The lack of carbides suggests the good thermal stability of CSS-engineered Fe–Cr–Ni alloys after annealing at the working temperature of BWR for 86.4 ks. The lack of oxides suggests a good oxidation resistance of CSS-engineered Fe–Cr–Ni alloys under the exposure of BWR working temperature in air for 86.4 ks.

2 Metallography

Figure 3.19a-d present the metallographic cross-sections of carburized AISI-316L, AL-6XN, IN-718, and nitro-carburized IN-718, respectively, after PCHE-A-Air (annealed at 620 K in air for 86.4 ks). White contrast-free 20 μm bands have been observed in carburized AISI-316L, AL-6XN, and IN-718 after the PCHE-A-Air treatment. Moreover, two bands, an outer 2 μm band that has etch contrast as well as an inner 20 μm band that is contrast-free have been observed in nitro-carburized IN-718 after the PCHE-A-Air process. The morphology and thickness of carburized and nitro-carburized near-surface zone does not show an obvious change compared to those that were CSS-engineered. The similar morphology implies similar corrosion resistance to the etchant between CSS-engineered and PCHE-A-Air treated Fe–Cr–Ni alloys. The similar thickness implies that carbon or nitrogen atoms diffuse a negligible distance at 620 K for 86.4 ks. This result is consistent with the XRD data.

3 SAM

Figure 3.20 compares the elemental concentration depth profiles of CSS-engineered Fe–Cr–Ni alloys before and after PCHE-A-Air. It can be seen that the Cr, carbon and nitrogen concentration profiles coincide between CSS-engineered Fe–Cr–Ni alloys and PCHE-A-Air treated specimens. Moreover, the concentration depth profiles of Fe, Ni also coincide between CSS-engineered Fe–Cr–Ni alloys and PCHE-A-Air annealed samples. This means that all atoms diffuse negligibly at 620 K for 86.4 ks. The SAM result is consistent with the XRD and metallography data.

4 Nano-hardness

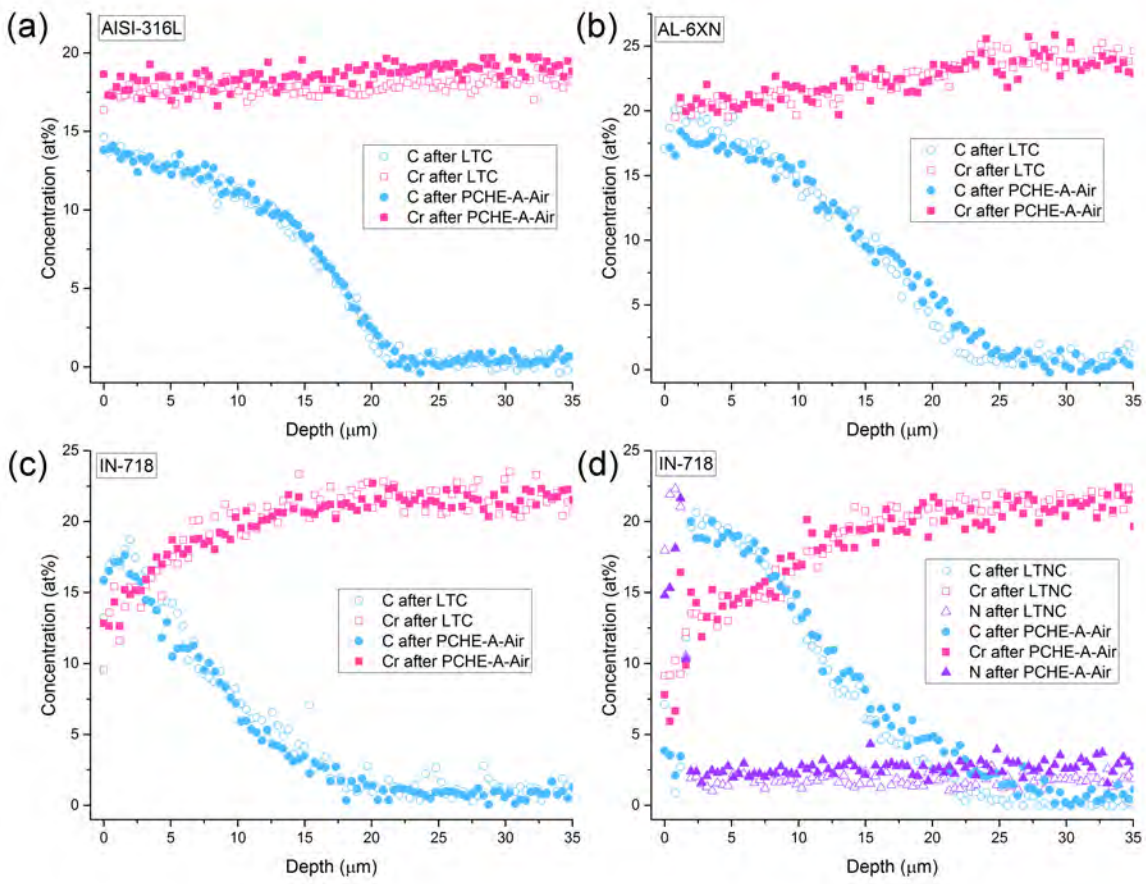

Figure 3.20. SAM elemental concentration depth profiles of (a) carburized AISI-316L, (b) carburized AL-6XN, (c) carburized IN-718, and (d) nitro-carburized IN-718, respectively, before and after PCHE-A-Air.

Figure 3.21 compares the nano-hardness depth profiles of CSS-engineered Fe–Cr–Ni alloys before and after the PCHE-A-Air process. It can be seen that the nano-hardness profiles coincide. The nano-hardness result is consistent with the XRD, metallography and SAM data.

Therefore, it is concluded that the corrosion resistance to the etchant, elemental distribution, and nano-hardness do not change for CSS-engineered Fe–Cr–Ni alloys after annealing at 620 K in air for 86.4 ks. In other words, the carbon atoms stay at the

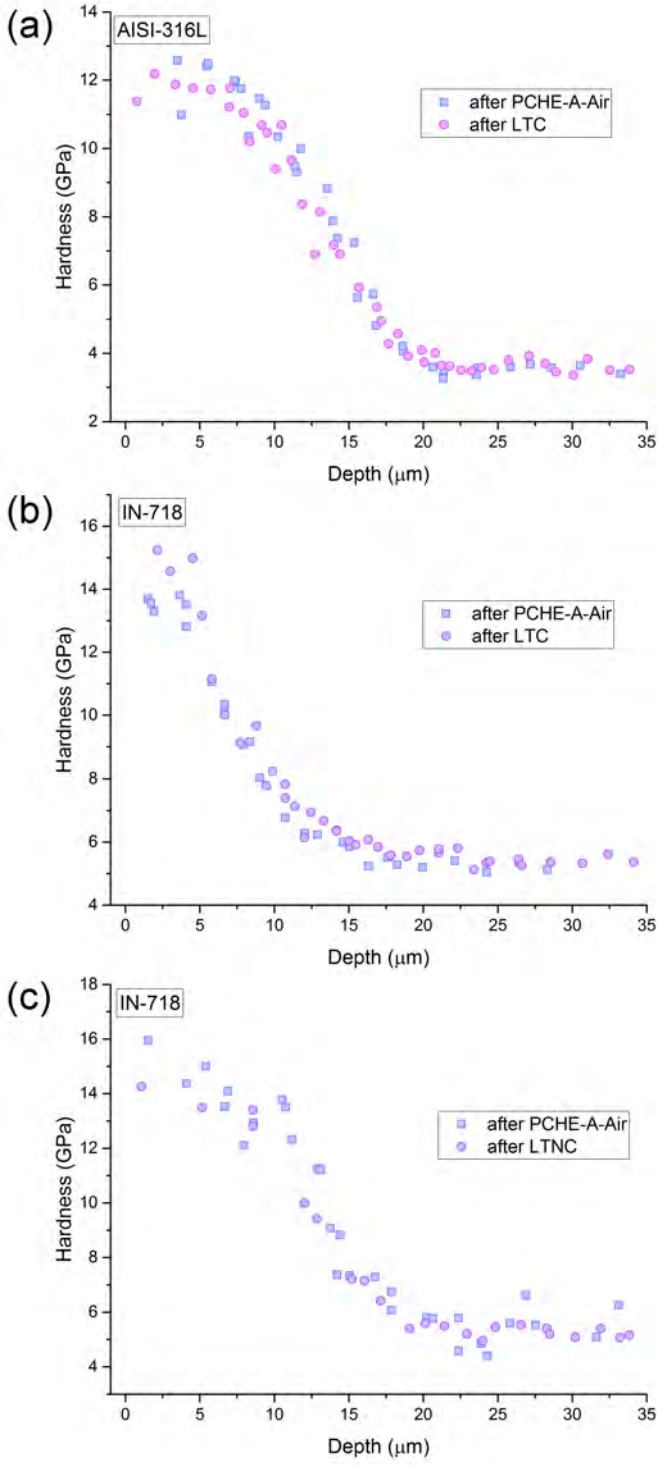

Figure 3.21. Nano-hardness depth profiles of (a) carburized AISI-316L, (b) carburized AL-6XN, and (c) carburized IN-718, respectively, before and after PCHE-A-Air.

interstitial sites of the FCC lattice instead of segregating to form carbides, retaining the corrosion and oxidation resistance, as well as the mechanical properties.

PCHE-B-Air and -Vac (annealed at 1070 K in air or in vacuum for 3.6 ks). The temperature in the BWR can reach 1000 K under the LCA condition in a very short time. In order to study the behavior of CSS-engineered Fe–Cr–Ni alloys under the LCA temperature, these alloys were exposed at 1070 K in air and in vacuum for 3.6 ks, represented as PCHE-B-Air and PCHE-B-Vac, respectively. The carburized or nitro-carburized near-surface regions after the annealing were then characterized by XRD, metallography, SAM TEM and nano-hardnesses measurements.

1 XRD

Figure 3.22a shows the XRD pattern of non-treated, carburized, and PCHE-B-Air treated AISI-316L. The diffraction peaks corresponding to FCC {111} and {200} in the PCHE-B-Air treated sample disappear, while the major oxide peaks are present; the oxide layer must be greater than 5 μm.

Figure 3.22b presents the XRD pattern of non-treated, carburized, PCHE-B-Air treated AL-6XN, and PCHE-B-Vac treated AL-6XN. In the PCHE-B-Air treated sample, the major peaks corresponding to FCC {111} and {200} are present. This indicates a thinner oxide layer (< 10 μm) of PCHE-B-Air treated AL-6XN compared to AISI-316L. However, {111} and {200} peak positions shift to much higher angles compared to carburized and 620 K annealed AL-6XN, even higher than those of a non-treated sample. This indicates a lattice contraction of AL-6XN after PCHE-B-Air (i. e. , the lattice parameter a of AL-6XN after PCHE-B-Air is smaller than that of non-treated sample). In addition, minor peaks, corresponding to carbides and oxides, are also observed in this sample. In the PCHE-B-Vac treated sample, similar lattice contraction as well

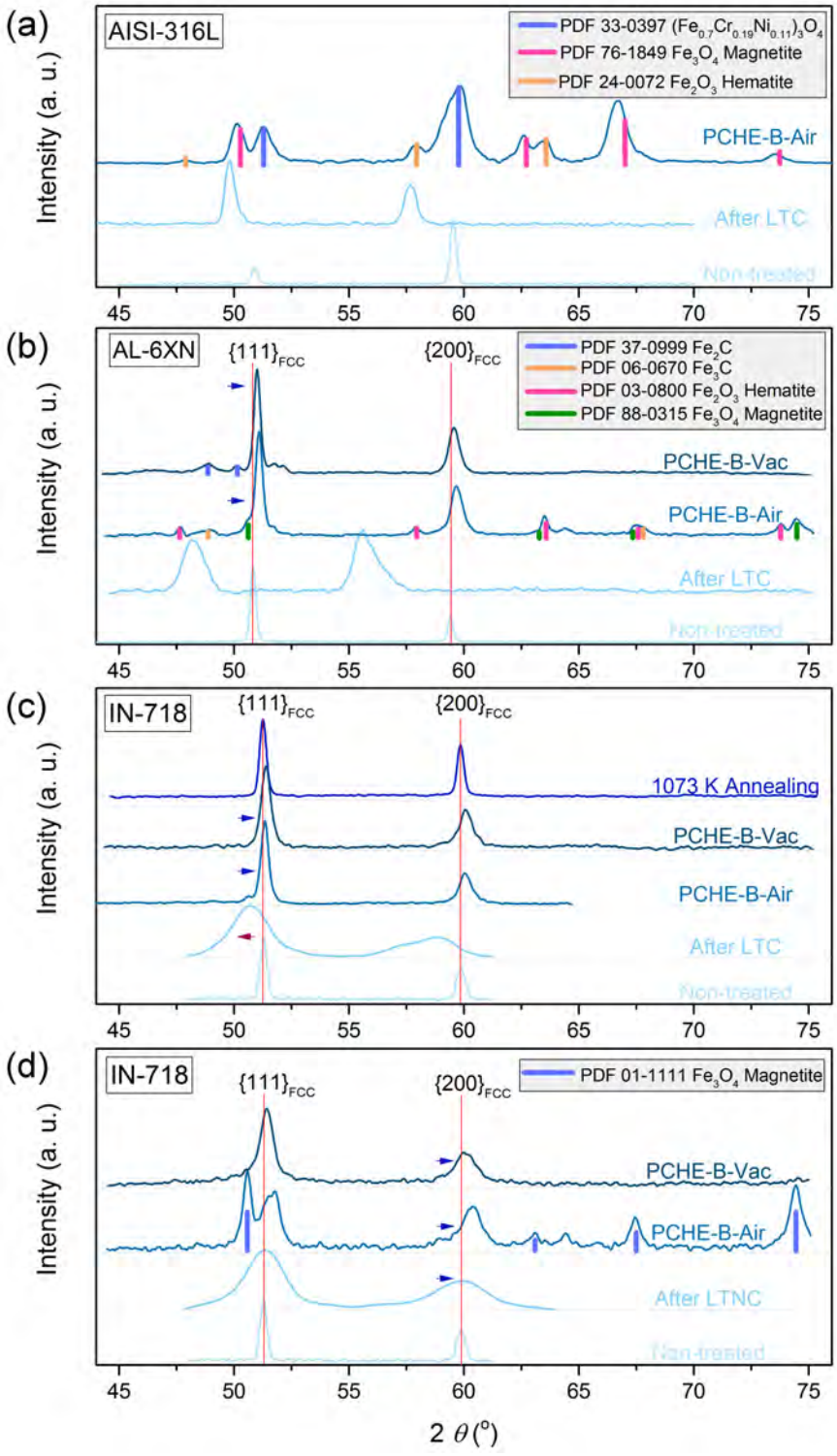

Figure 3.22. X-ray diffractograms of (a) carburized AISI-316L, (b) carburized AL-6XN, (c) carburized IN-718, and (d) nitro-carburized IN-718, respectively, before and after the PCHE-B-Air and -Vac treatment.

as the formation of a small amount of carbides has also been observed, while peaks corresponding to oxides were not observed.

Figure 3.22c shows XRD patterns of non-treated, carburized, PCHE-B-Air treated, PCHE-B-Vac treated, and 1070 K annealed IN-718. In the PCHE-B-Air and PCHE-B-Vac treated sample, only FCC {111} and {200} peaks are present. The carburized IN-718 does not significantly oxidize at 1070 K in air for 3.6 ks. Moreover, the peak positions of FCC {111} and {200} shift to higher angles, indicating a lattice parameter a shrinkage after PCHE-B-Air and PCHE-B-Vac treatment. However, lattice parameter a shrinkage has not been observed in non-treated IN-718 after annealing at 1070 K in air for 3.6 ks, as seen in Fig 3.22.

Figure 3.22d shows XRD patterns of non-treated, nitro-carburized, PCHE-B-Air treated, and PCHE-B-Vac treated IN-718. In the PCHE-B-Air treated sample, extra oxide peaks with strong intensities have been observed. This indicates that the oxide layer is thicker on PCHE-B-Air treated nitro-carburized IN-718 than on carburized AL-6XN with the same treatment. On the contrary, extra peaks are absent in PCHE-B-Vac treated sample. For both samples, the peak positions of FCC {111} and {200} shift to higher angles than those of the non-treated specimen, which is similar to the observations in carburized AL-6XN and IN-718 after PCHE-B-Air and -Vac treatment. This also indicates a lattice parameter shrinkage of nitro-carburized IN-718 after the PCHE-B-Air and -Vac process.

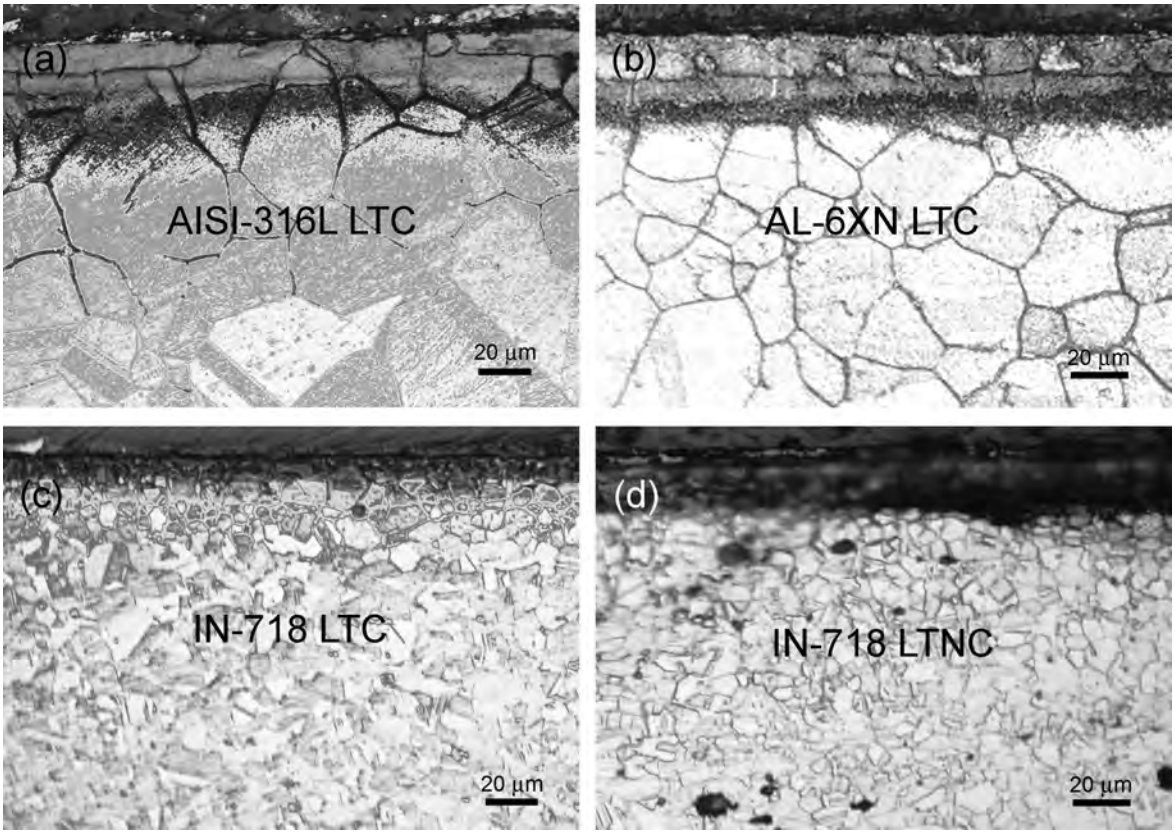

Figure 3.23. Metallographic cross-sections of (a) carburized AISI-316L, (b) carburized AL-6XN, (c) carburized IN-718, and (d) nitro-carburized IN-718, respectively, before and after PCHE-B-Air and -Vac.

In a word, after annealing at LCA temperature of BWR (1070 K) in air for 3.6 ks, carburized IN-718, carburized AL-6XN, nitro-carburized IN-718, and carburized AISI-316L have gradually decreased oxidation resistance, according to the fraction of oxides shown in XRD patterns. The origin of the lattcie contraction will be further discussed in the 'Discussion' section.

2 Metallography

Figure 3.23a-d presents the metallographic cross-sections of carburized AISI-316L, AL-6XN, IN-718, and nitro-carburized IN-718 after the PCHE-B-Air treatment. The

continuous and contrast-free white bands, corresponding to the carburized or nitro-carburized near-surface region, have disappeared in all these samples. Instead, dark layers have been observed, and carburized IN-718 has the thinnest dark region among these alloys. Such dark layers have also been observed in the Fe–Cr–Ni samples after the PCHE-B-Vac treatment. The nature of the dark layer is unclear. Sensitization might occur during the PCHE-B-Air and -Vac treatments and resulted to the loss of corrosion resistance in the near-surface region of CSS-engineered Fe–Cr–Ni alloys. The phases and elemental distributions in the carburized and nitro-carburized near-surface zones have been further studied by SAM and TEM.

3 SAM

Figure 3.24a shows the Cr, carbon and oxygen concentration depth profiles of carburized AISI-316L after PCHE-B-Air. An oxygen-rich outer layer, with a thickness of ≈ 12 μm, is present. Moreover, this layer is poor in carbon. Signals from Fe, Cr, and Ni are also observed in this layer. Combined with the XRD data, shown in Fig 3.22a, it can be concluded that the outer layer is composed of Fe-, Cr- and Ni-oxides. The depletion of carbon in this layer implies that the carburized near-surface region completely oxidizes up to ≈ a depth of 12 μm after the PCHE-B-Air treatment. This is consistent with the XRD data, in which only oxide diffraction peaks were detected. The oxide layer can be clearly observed in the SEM image, shown in Fig 3.25.

Under the oxide layer, a carburized region appears, with the carbon concentration increasing from the edge of the oxide layer (12 μm) to ≈ 15 μm, as seen in Fig 3.25. The carbon concentration reached ≈ 8 at% at the depth of 15 μm. For the PCHE-B-Air treated AISI-316L, the carbon concentration depth profile extends to about 40 μm, which is much deeper than that of the carburized sample (20 μm).

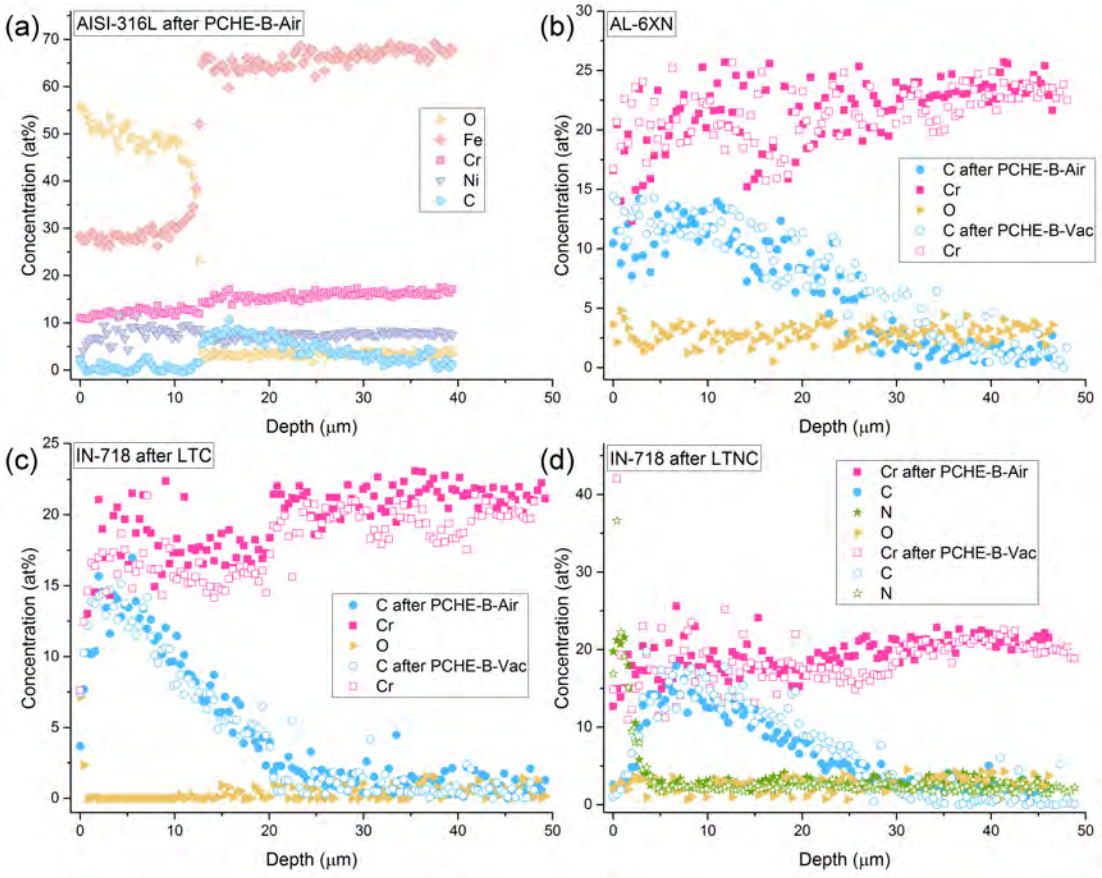

Figure 3.24. SAM elemental concentration depth profiles of (a) carburized AISI-316L, (b) carburized AL-6XN, (c) carburized IN-718, and (d) nitro-carburized IN-718, respectively, before and after PCHE-B-Air and -Vac.

Figure 3.24b shows the Cr, carbon and oxygen concentration depth profiles of carburized AL-6XN after the PCHE-B-Air and PCHE-B-Vac treatments. The oxygen-rich layer is not observed for the PCHE-B-Air treated AL-6XN in the Auger profile, although diffraction peaks belonging to oxides have been observed in the XRD pattern. This is probably due to the loss of the oxide layer before the chemical analysis. A black layer was seen on the surface of epoxy mount after the specimens were taken out for chemical analysis.

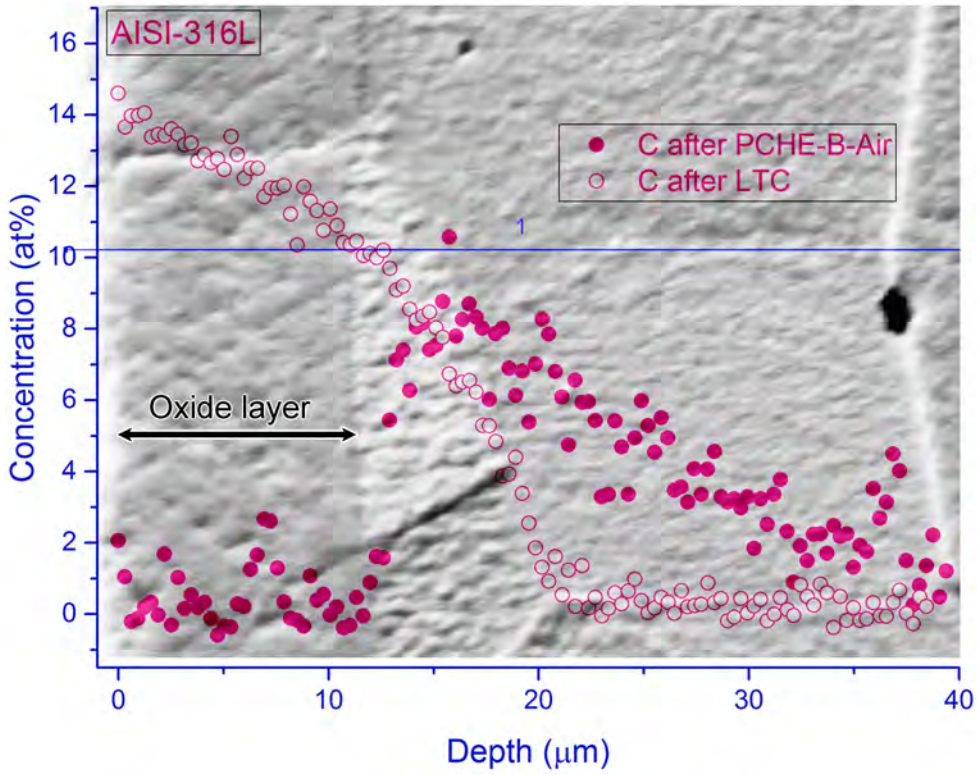

Figure 3.25. Secondary electron image and corresponding SAM carbon concentration depth profiles of carburized AISI-316L (red circle), and LTC AISI-316L after PCHE-B-Air (red disk).

Both samples yield high carbon and Cr signals, which is probably due to the formation of carbide particles during the annealing process. Moreover, both samples have similar carbon and Cr concentration depth profiles. The similar Cr depth profiles to those of carburized sample suggests that there is no further Cr depletion during annealing. Compared to those of carburized AL-6XN, shown in Fig 3.26a, the shape of Cr depth profiles of PCHE-B-Air and PCHE-B-Vac treated AL-6XN is similar to those of carburized specimen, while the carbon depth profiles extend to longer distance ($\approx 30\,\mu m$) and the carbon concentration at the surface dropped from 20 at% to about 12 at%. The change of carbon depth profiles indicates that carbon diffuses a significant distance (from 22 μm to 30 μm) during annealing at 1070 K for 3.6 ks.

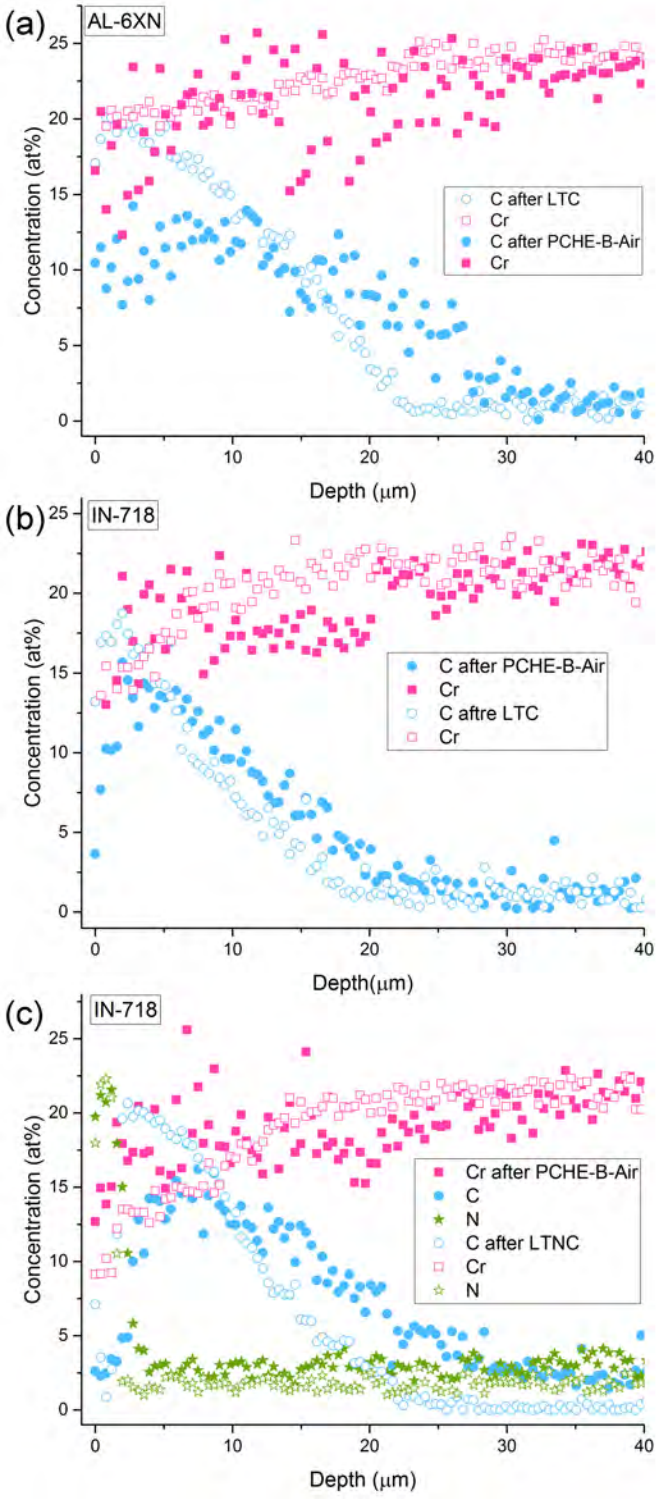

Figure 3.26. SAM elemental concentration depth profiles of carburized and PCHE-B-Air treated (a) AL-6XN, (b) IN-718, respectively. (c) Nitro-carburized and PCHE-B-Air treated IN-718.

Figure 3.24c shows the Cr, carbon and oxygen concentration depth profiles of carburized IN-718 after the PCHE-B-Air and PCHE-B-Vac treatments. Oxygen signals appear in the first 0.5 μm of IN-718 after the PCHE-B-Air treatment. Such a thin oxide layer is probably the reason that oxide peaks cannot be detected by XRD.

The Cr signals in the near-surface regions also become higher in both air and vacuum-annealed samples compared to carburized sample (Figure 3.26b), which is probably due to the formation of carbide particles during the annealing process. The size of the Auger electron beam is 20 nm and the size of carbide is around 100 nm in the air and vacuum-annealed IN-718 samples. Moreover, there is no significant Cr concentration difference between air and vacuum-annealed samples, Cr depletion being observed in both samples. Compared to carburized IN-718, shown in Figure 3.26b, there is no further Cr depletion during annealing at 1070 K for 3.6 ks. Depletion of carbon is detected in the first 5 μm for both air and vacuum-annealed IN-718 samples, in comparison to the carbon profile of as-carburized sample seen in Figure 3.26b. This is the first time that decarburization was observed in low-temperature carburized alloys, such as AISI-316L, 2205 and IN-718.

Figure 3.24d shows the Cr, carbon, nitrogen and oxygen concentration depth profiles of nitro-carburized IN-718 after the PCHE-B-Air and PCHE-B-Vac treatments. An oxygen-rich layer is not observed for the PCHE-B-Air treated IN-718 in the Auger profile, although diffraction peaks belonging to oxides have been observed in the XRD pattern. This is probably due to the loss of the oxide layer before the chemical analysis.

Similar to that of AL-6XN and IN-718, nitro-carburized IN-718 after the PCHE-B-Air and -Vac treatments also show higher Cr signals in the near-surface region compared to nitro-carburized sample (Figure 3.26c). Moreover, there is no significant Cr concentration difference between air and vacuum-annealed samples. Compared to nitro-carburized IN-718, there is no further Cr depletion during annealing at 1070 K for 3.6 ks. In addition, the nitrogen-rich region (the first 3 μm) also does not show observable differences among nitro-carburized, air and vacuum-annealed samples. The carbon-rich zone starting at 3 μm thickness, on the contrary, has clear difference between nitro-carburized and annealed samples.

4 TEM

A cross-sectional view of microstructure of PCHE-B-Air treated AL-6XN is shown in Figure 3.27. Figure 3.27a shows two porous layers on top of AL-6XN substrate, with the total thickness ranging from 3 μm to 7 μm. It can be seen clearly in the STEM images (Figure 3.27b and c) that this layer contains two sub-layers: (1) layer 1 with dense and large grains, and (2) layer 2 with smaller grains. In layer 1, there are bright and dark grains, as seen in Fig. 3.27c. STEM provides "Z-contrast" images when high angle angular dark field detector with a short camera length is used.

This can be confirmed by XEDS mapping. Figure 3.28 maps two grains: the dark grain contains mainly Fe and oxygen, while the bright grain contains Fe, Ni, Mo and oxygen. Figure 3.29 maps the interface of layer 1 and 2. At the layer 1 side, a bright grain which is rich in Mo, Ni is observed. Similar elemental distributions have been observed in other grains in layer 1. XEDS data showed the composition is $Mo_{11}Fe_5Ni_8O_{76}$. The fractions of Mo, Fe and Ni might have some variations in different grains.

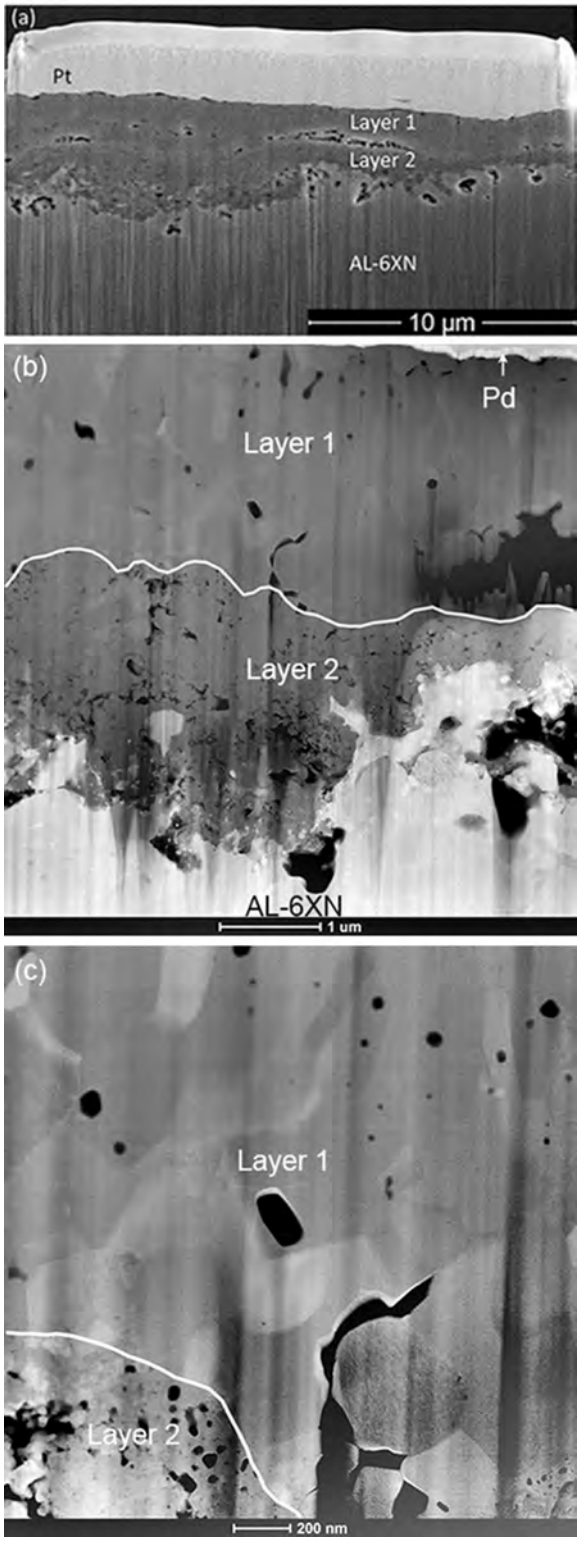

Figure 3.27. (a) SEM cross-sectional image, (b) and (c) STEM images of carburized AL-6XN after PCHE-B-Air.

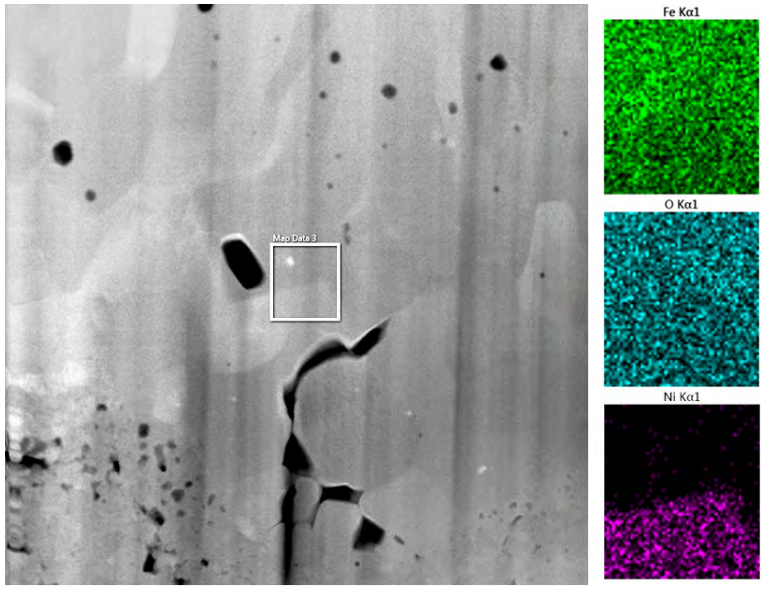

Figure 3.28. STEM "Z-contrast" image and corresponding XEDS maps of carburized AL-6XN after PCHE-B-Air.

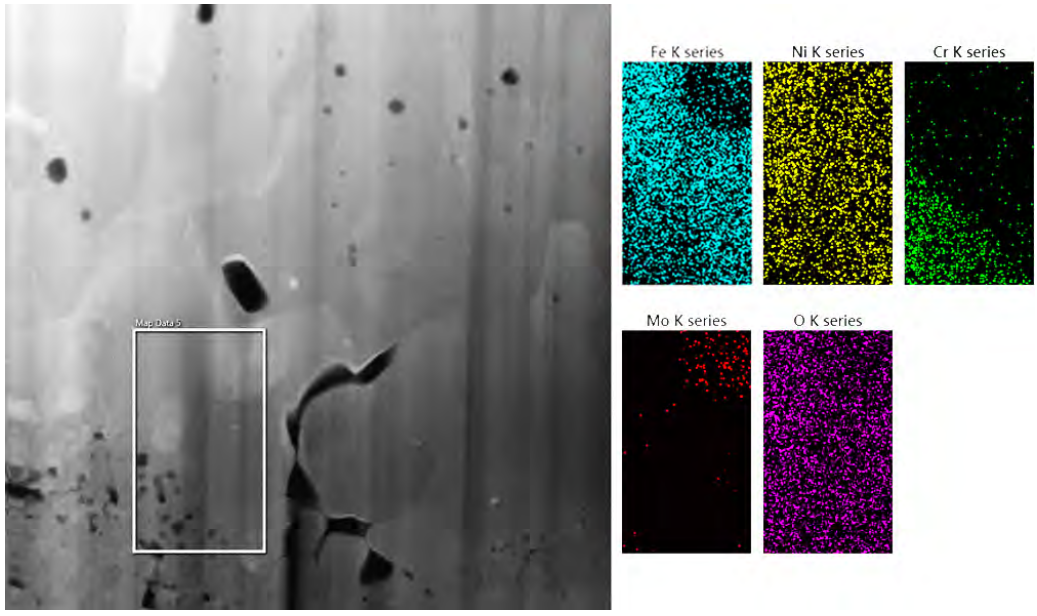

Figure 3.29. STEM "Z-contrast" image and corresponding XEDS maps of carburized AL-6XN after PCHE-B-Air.

The layer 2 side, as shown in Figure 3.29, contains Cr, Fe, Ni and oxygen. XEDS data showed that layer 2 is an $(Cr_{15},Fe_{12},Ni_6)O_{67}$ oxide. The fraction of elements might

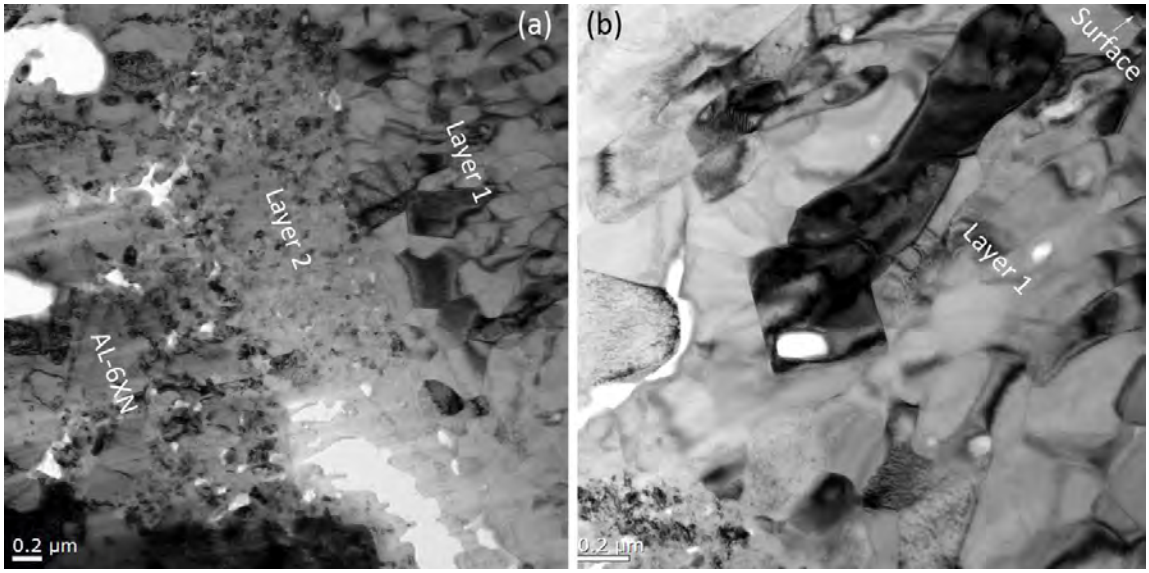

Figure 3.30. TEM BF images of carburized AL-6XN after PCHE-B-Air.

have some variation in different grains. The difference between layer 1 and layer 2 is that layer 2 contains Cr while layer 1 does not. The existence of these oxides in XEDS mapping is consistent with the XRD data, in which oxides were detected.

Figure 3.30 show the TEM-BF (bright-field) images of layer 1 and 2. The images indicate that layer 2 contains nano-sized grains, while layer 1 contains columnar grains.

Considering that carburized IN-718 specimen has the best oxidation resistance among these CSS-engineered Fe–Cr–Ni alloys at 1070 K, the microstructure as well as elemental spatial distribution of carburized IN-718 after the PCHE-B-Air treatment was studied. In Fig 3.31, four regions are identified. Region 1 and 2 are Pt and Pd layers, respectively, deposited before Ga^+ milling in order to protect the sample surface. Region 3 is darker than region 4, indicating a high volume fraction of elements with low atomic mass. In region 4, dark nano-sized zones are dispersed in the bright region, indicating a segregation of elements with light weight inside a region that has

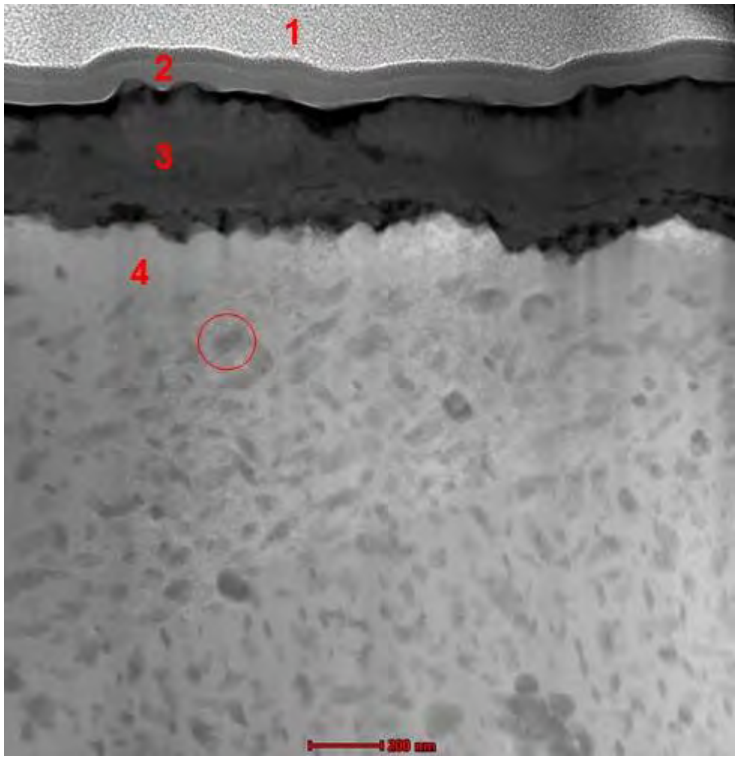

Figure 3.31. STEM image of carburized IN-718 after PCHE-B-Air. Regions 1 and 2 are Pt and Pd layers, respectively, deposited before Ga^+ milling in order to protect the sample surface.

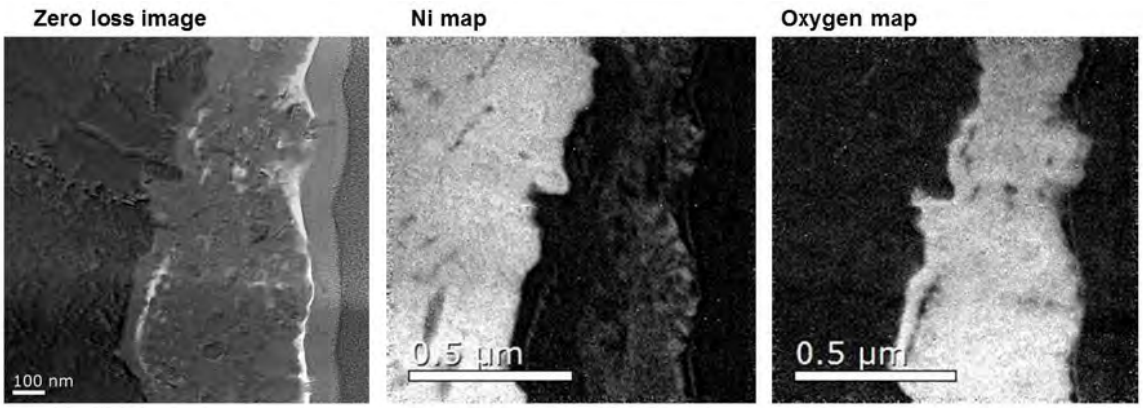

Figure 3.32. TEM Zero-loss image, ESI Ni and oxygen maps of the surface layer (region 3) of carburized IN-718 after PCHE-B-Air.

a high volume fraction of heavy elements. To identify the elements in region 3 and 4, ESI (electron-spectroscopic imaging) and XEDS mapping were used.

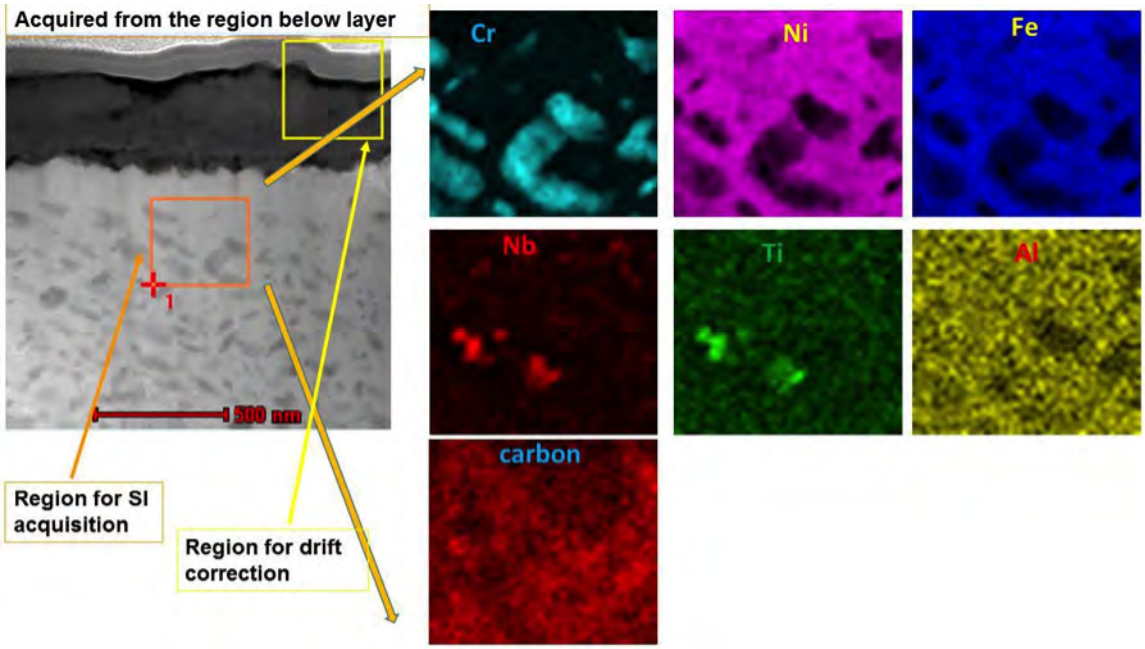

Figure 3.33. XEDS elemental maps of carburized IN-718 after PCHE-B-Air. Mapping area is the one inside the orange rectangle.

Figure 3.32 is the HAADF-STEM image of the 1070 K (air) annealed IN-718. During the heat treatment, an oxide layer formed at the surface, as seen in region 3 in Figure 3.31 and in Figure 3.32. The thickness of this oxide layer ranges from 100 to 500 nm. Figure 3.34 presents the EFTEM (energy filtered transmission electron microscopy) elemental maps for Ni, Fe, Cr and C. The region of acquisition is provided by the TEM image acquired with the pre-C edge. The other elemental maps clearly show that the particles are rich in Cr and C (the brighter regions in the elemental maps show the local presence of the corresponding element). They are Cr-rich carbides. These carbide particles are nano-sized (about 100 nm in longest dimension).

Figure 3.33 presents the XEDS elemental maps acquired from the region containing Cr carbide particles (orange rectangle). The whole maps were acquired with drift correction (yellow rectangle). These particles are found to be rich in Cr. However,

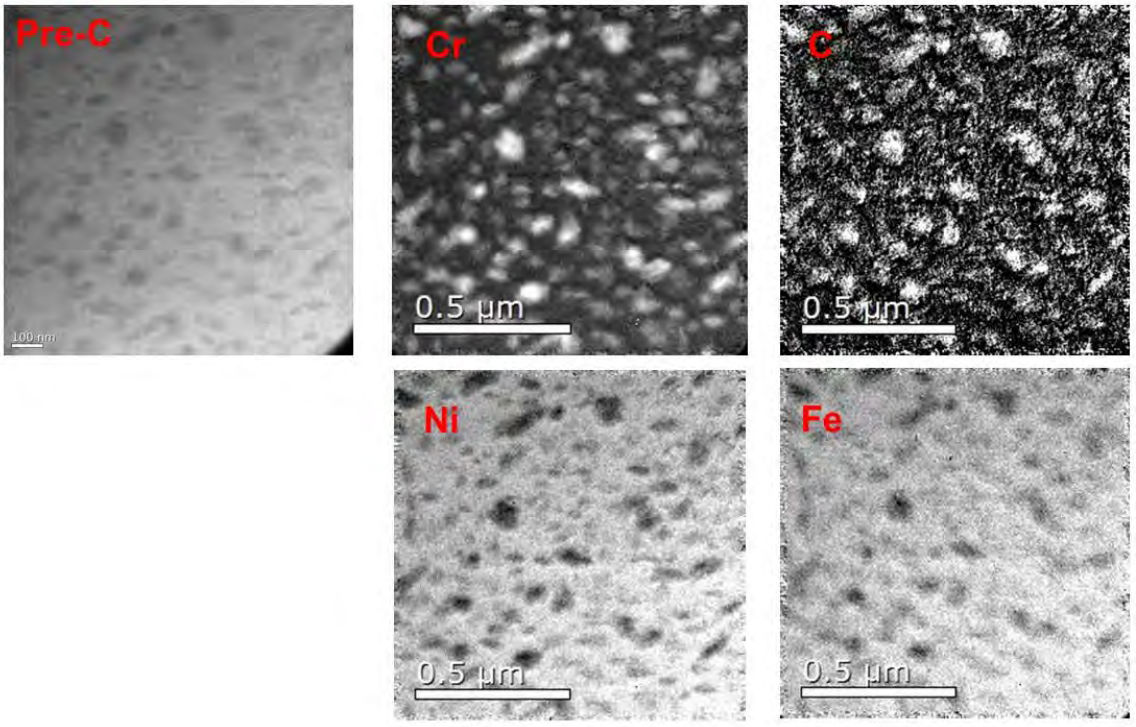

Figure 3.34. EFTEM elemental maps acquired from the region for Cr, C, Ni and Fe. Brighter regions show the presence of the respective elements in the elemental maps.

since XEDS is not sensitive to light elements, the carbon map, Figure 3.33, does not show any useful information. EFTEM is a better tool to detect light elements like carbon. The carbon and chromium maps in Figure 3.34 clearly show that these nano-sized particles are chromium carbides.

5 Nano-hardness

According to Figure 3.35a, the first 12 µm from the surface of AISI-316L is very hard, since this area is full of oxides. The high hardness in the first 12 µm suggested that this oxide layer is not porous but dense. Hardness starts to decrease at 12 µm until the core. The nano-hardness data agree with the SAM data in Figure 3.25 very well.

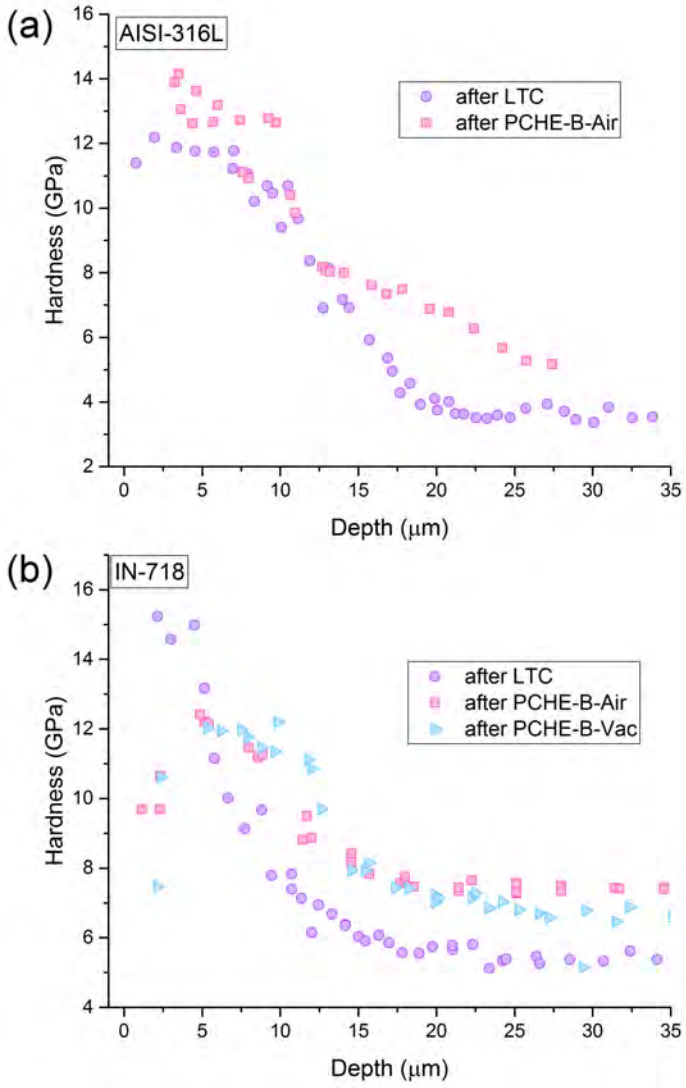

Figure 3.35. Nano-hardness depth profiles of (a) carburized AISI-316L, and (b) carburized IN-718, respectively, after PCHE-B-Air and PCHE-B-Vac.

Although LTC AISI-316L seems very stable at a BWR simulated circumstance and McClintock *et al.*[59] suggested that there are not significant mechanical property changes between the as-received 316L and the Kolsterising-treated 316L, severe SCC in LTC AISI-316L specimen indicates that AISI-316L treated with LTC cannot help to suppress SCC. Moreover, all the evidences imply that LTC AISI-316L cannot survive a LCA.

Therefore, another CSS engineered alternative, which is more corrosion and oxidation resistant than AISI-316L, should be investigated to fit the application requirements during a LCA.

Figure 3.35b showed the decreasing of hardness at the first 5 μm for both IN-718 specimens annealed in air and vacuum. The loss of hardness resulting from the depletion of C agrees well with the carbon profile seen in Figure 3.24.

3.2.4 Irradiation Tests

Considering the best mechanical properties (hardness, wear resistance, tensile strength, and ductility) and the best oxidation resistance of carburized IN-718 among these CSS-engineered Fe–Cr–Ni alloys, focus was given to irradiation behavior of carburized IN-718.

IN-718 after LTC. The carburized IN-718 sample was exposed to 1.5 MeV protons to 0.5 dpa (displacement per atom) at 620 K for 86.4 ks (24 h).

Nano-sized particles were observed in irradiated IN-718 after carburization, as shown in Figure 3.36c; however, no particles are present in the non-treated sample in Figure 3.36a and in the carburized IN-718 seen in Figure 3.36b. Satellite reflections in Figure 3.37 are possibly from epitaxial surface oxide. In addition, the elemental map, as shown in Figure 3.38, suggests that these nano-sized particles are nano-sized carbides.

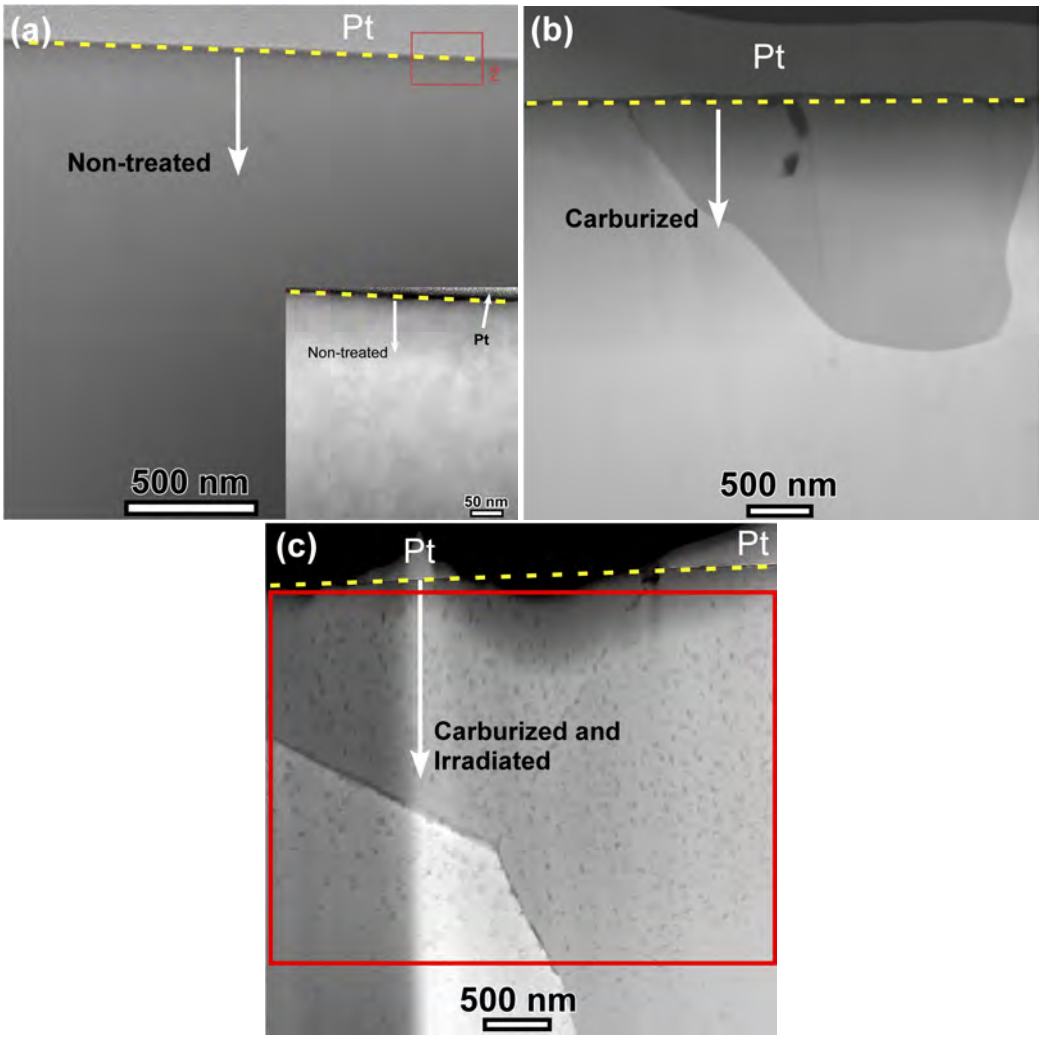

Figure 3.36. STEM images of (a) non-treated, (b) carburized and (c) carburized IN-718 after irradiation test, respectively.

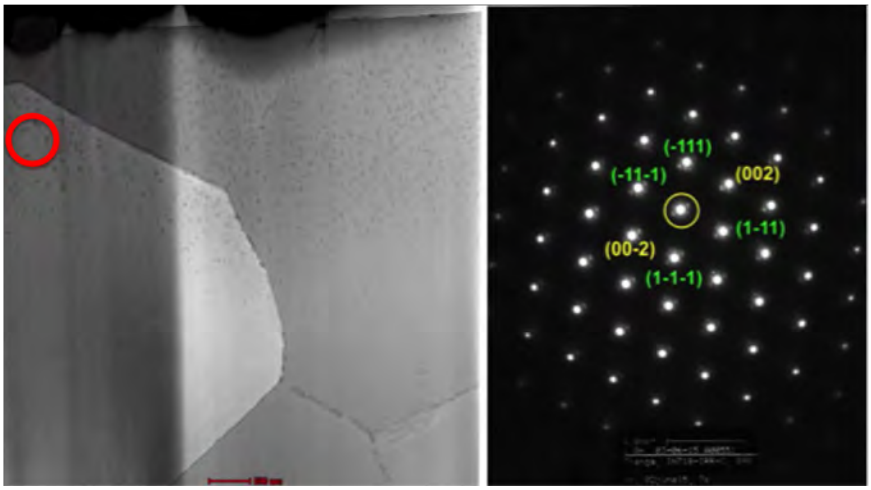

Figure 3.37. TEM image of LTC IN-718 after irradiation (diffraction pattern comes from the region of enclosed red circle).

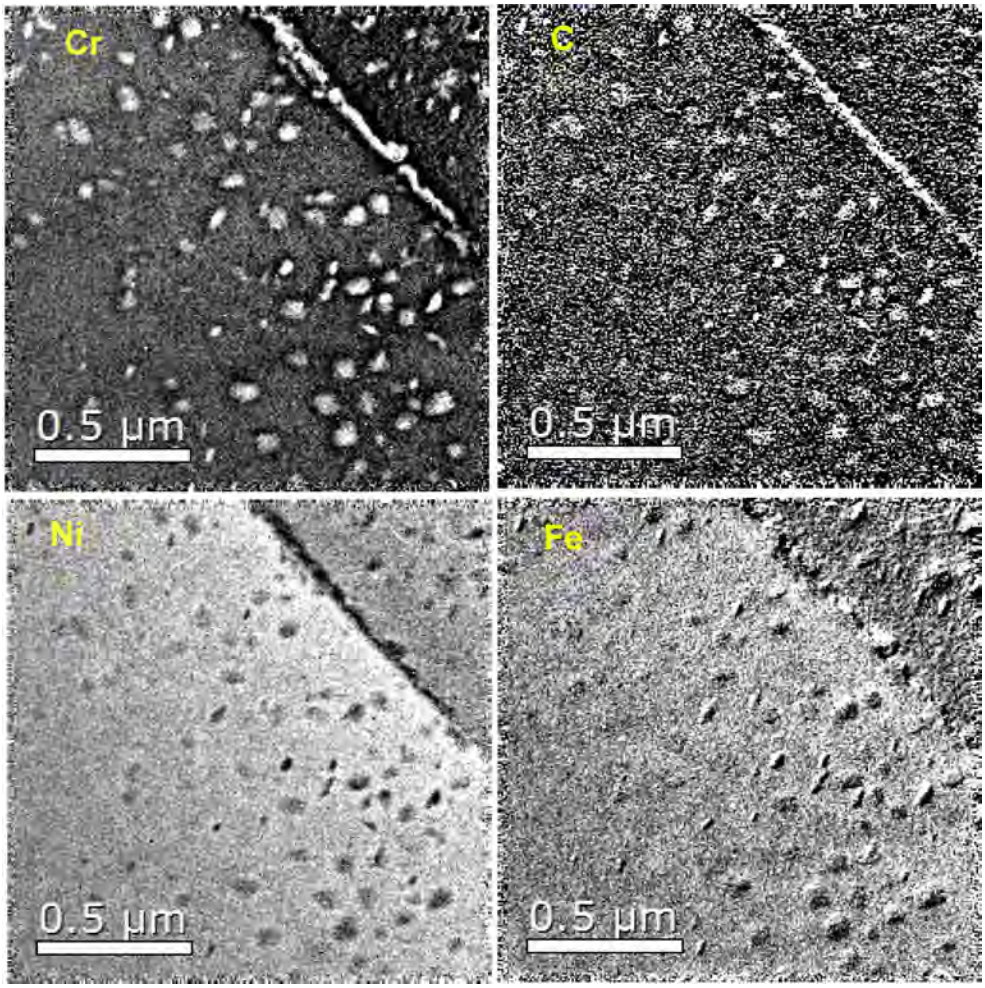

Figure 3.38. EFTEM (energy filtered transmission electron microscopy) elemental maps of irradiated IN-718 after carburization. Brighter regions show the presence of the respective elements in the elemental maps.

4 Discussion

4.1 Possible Mechanisms of Passivation by Ethanol

Figure 4.1 shows how the AAA method works. Accordingly, contact with ethanol after etching passivates the surface against re-formation of the initial, passivating Cr-rich oxide layer. To reform the oxide layer requires contact with oxygen.

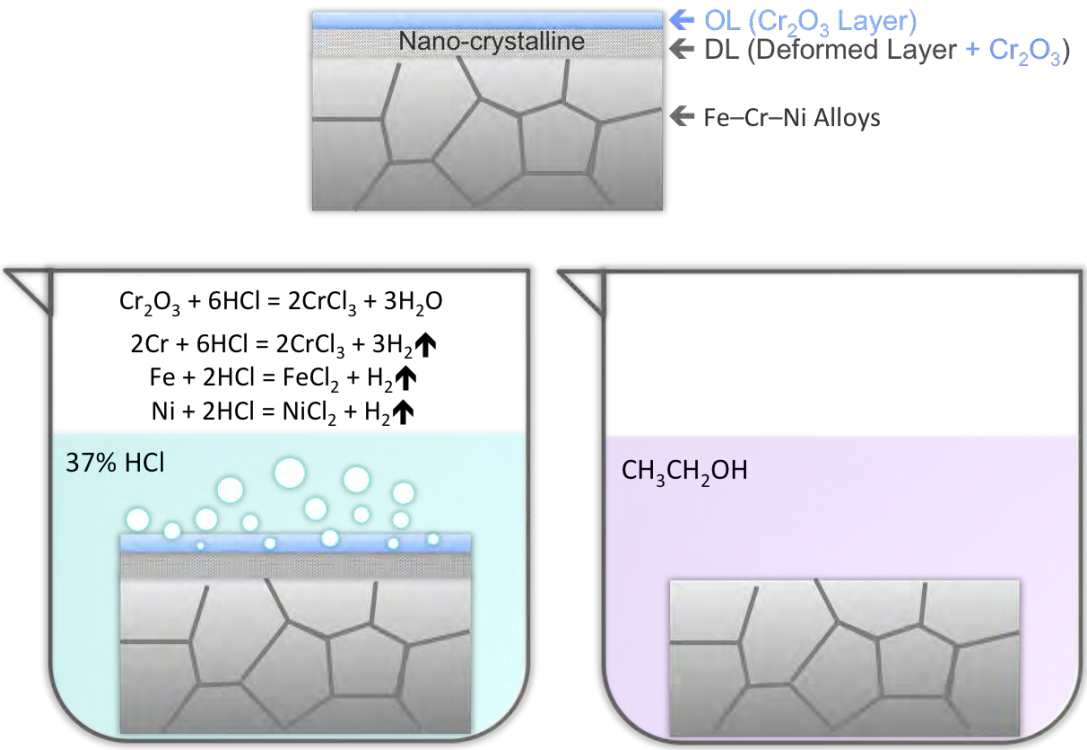

Figure 4.1. AAA process applied on Fe–Cr–Ni alloys.

There are two hypotheses in which ethanol could preserve the alloy surface and an activated state after stripping the oxide:

(1) Ethanol molecules that could be adsorbed as a film on the alloy surface – a film that prevents the formation of the usual Cr-rich oxide layer.

(2) Metal ethoxides generated on the surface could form a film to protect the activated surface.

Ethanol molecules could form a protective film to prevent the activated surface from oxidizing. This is the first possible mechanism of ethanol passivation. After the immersion of AISI-316 and AL-6XN specimens in highly concentrated (22.4 at%) HCl for activation, these samples were transfered into ethonal immediately. Later (around 300 s), Fe–Cr–Ni alloys (without drying the ethanol on the surface of these specimens) were transfered from ethanol to carburizing furnace, where was purged with nitrogen before these specimens were moved in, for further carburization. The purity of ethanol used for protecting the activated surface of Fe–Cr–Ni alloys is 99.99 %. The oxygen diffusivity in ethanol/toluene solution at room temperature is about $5 \times 10^{-9}\,m^2/s$,[60] which can yield a diffusion distance of 1 mm in ethanol. It is can be expected that the oxygen diffusivity in pure ethanol can be at the same level compared to that in ethanol/toluene solution. Furthermore, oxygen dissolved in this highly purified ethanol in 300 s is negligible, suggesting the activated surface of Fe–Cr–Ni alloys can be protected while they are immersed in ethanol. When these Fe–Cr–Ni alloys were taken out from the ethanol, they were covered and protected by ethanol. Considering that only 30 s is needed to transfer the Fe–Cr–Ni alloys into the carburizing furnace, it is possible that an ethanol film with several micrometers was left to cover and protect the activated surface of Fe–Cr–Ni alloys, although it is known that ethanol can evaporate at room temperature. Finally, this

protective ethanol film evaporate in the nitrogen purged carburizing furnace with elevated temperature, and then the activated surfaces were exposed to carburizing gases.

The second possible mechanism of passivation by ethanol can be due to the formation of metal ethoxides, which protected the surface from re-oxidation, on the activated surface of Fe–Cr–Ni alloys. The most common metal ethoxide is sodium ethoxide, which can be prepared by adding metal to sodium into absolute ethanol. Generally, metal ethoxides can be dissolved in ethonal,[61,62] and the pyrolysis (forming metal oxides) temperature of metal ethoxide can be as low as 520 K.[63]

Chromium, iron and nickel ethoxides are especially interested herein. Chromium, iron and nickel ethoxides were used as precursors of oxides because these exthoxide decomposed with elevated temperature.[63–65] Iron ethoxide is not easy to react with oxygen (oxidizing).[65] Metal (Cr, Ni *etc.*) ethoxides can be prepared by mixing the metal chloride, ethanol and sodium ethoxide.[63,64] Moreover, Kubo *et al.* reported that CrN can react with ethanol forming chromium ethoxide during the tribological testing.[66]

It is possible that metal ethoxides were formed when the activated Fe–Cr–Ni alloys were immersed in ethanol. In this case, even if ethanol in some part of the sample fully evaporated during the transfer of specimen, the part exposed to air can be protected by metal ethoxides left after the evaporation of ethanol. After the specimens transfered into the carburizing furnace, ethanol evaporated with elevated temperature left the metal ethoxides film on the activated surface of Fe–Cr–Ni alloys. When temperature was higher enough (i. e. 570 K), metal ethoxides can decomposed to metal oxides. It is known that iron and nickel oxides cannot provide protective film to prevent the infusion of C atoms.

4.2 CSS-engineering of AISI-316L, AL-6XN and IN-718

4.2.1 Interstitial Carbon in LTC Fe–Cr–Ni Alloys

It is well known that Cr has high affinity to carbon, and it is for this reason that colossal super-saturation with carbon interstitials can be achieved in Fe–Cr–Ni alloys. The Cr compositions for AISI-316L, AL-6XN and IN-718 are 18 at%, 20 at% and 24 at%, respectively. Figure 3.12 implies the higher the Cr composition, the higher carbon concentration that can be achieved while carburizing these Fe–Cr–Ni alloys with similar carbon activity. Carbon activity in the carburizing furnace at CWRU for AISI-316L, AL-6XN and IN-718 ranges from 0.88 to 1.[35] The highest carbon concentration, which can be obtained on the outermost carburized region, is 15 at%, 20 at% and 18 at% for AISI-316L, AL-6XN and IN-718, respectively. In addition, carbon diffusivity is highly dependent on the carbon concentration. This will be fully discussed in later sections. However, it does not necessarily mean that the higher carbon concentration the Fe–Cr–Ni alloys have, the larger lattice parameter expansion they show. It has been observed that all of the Fe–Cr–Ni alloys show more or less Cr depletion, as will be discussed in a later section, after the LTC and LTNC process. The lattice parameter of Fe–Cr–Ni alloys could be expanded more compared to that of Cr-loss LTC and LTNC Fe–Cr–Ni alloys, if no Cr depletion would occur during the LTC and LTNC.

4.2.2 Acetylene Carburization of AL-6XN

The major barriers for infusion of carbon in AL-6XN were discussed in this section. There are two barriers preventing the inward diffusion of carbon during carburization: (1) a Cr-rich oxide layer on the alloy surface and (2) a nano-crystallized layer generated

by surface machining/polishing. Ge *et al.*[31] reported that acetylene can activate and carburize finely polished AISI-316L (the mechanical deformed layer is polished off). Meanwhile, acetylene can also activate and carburize AISI-316L with a combination of coarse polishing and acid immersion (the Cr-rich oxide layer and mechanical deformed layer can be both removed). However, if the AISI-316L is merely polished, the coarser the surface finish, the thinner the carburized layer can be achieved, implying acetylene can remove the Cr-rich layer but has some difficulty removing the nano-crystallized layer on the surface of AISI-316L sample. In addition, it indicated that the carbon-infusion-barrier of the nano-crystalline layer can be easily removed by dipping in aqueous HCl at room temperature. However, the data in Figure 3.5 suggested that the Cr-rich oxide layer is the main barrier for infusion of carbon in AL-6XN since the finely polished and electropolished AL-6XN coupons, where Cr-oxide layer is the only barrier for the infusion of interstitial atoms because the nano-crystalline layers were removed, cannot be carburized uniformly. AL-6XN is much more corrosion resistant in comparison with AISI-316L. The acetylene itself simply cannot fully activate (remove the Cr-rich oxide layer) the surface of AL-6XN, resulting in no further infusion of carbon atoms.

4.2.3 Shape of XRD Peaks after LTC and LTNC

All the LTC Fe–Cr-Ni alloys (AISI-316L, IN-718 and AL-6XN) showed lattice parameter expansion after LTC. Accordingly, the {111} and {200} peaks were shifted to lower 2θ angles compared to those of non-treated spcimens. However, the {111} and {200} peaks of LTNC IN-718 seen in Figure 3.3 were shifted to higher 2θ angles compared to those of non-treated IN-718. This implies that the lattice of LTNC IN-718 shrank. Figure 3.12 indicated that only around 9 at% of Cr was left in the nitrogen-rich region, suggesting nearly 12 at% Cr depletion. Although the nitrogen concentration in the nitrogen-rich

region is as high as 20 at%, it is still not enough to compensate the lattice parameter shrinkage introduced by losing as much as 12 at% Cr. Nitriding might cause Cr depletion as well and this is probably the reason that LTNC introduced more Cr depletion in IN-718 compared to LTC.

Although all the LTC Fe–Cr–Ni alloys had Cr depletion, the lattice parameter expansion caused by infusion of carbon is large enough to compensate for the lattice parameter contraction produced by Cr depletion, so overall lattice parameter expansions were observed for LTC Fe–Cr–Ni alloys. This could be explained by the following reasons: (1) since Cr loss in LTC IN-718 is less than that in LTNC IN-718, lattice parameter shrinkage in LTC IN-718 is less than that in LTNC IN-718 and (2) the radius (56 pm)[67] of nitrogen atom is less than that (67 pm)[67] of carbon atom, so the expansion introduced by nitrogen interstitials should be smaller than that generated by carbon interstitials.

Evidence of texture in the non-treated AISI-316L is present, but the texture disappeared after LTC, as seen in Figure 3.1. The coupons were cold rolled and then annealed. The strong evidence of texture indicated that recrystallization was not fully completed after the annealing process. However, texture in AISI-316L was gone after the LTC, as shown in Figure 3.1. Possibly, recrystallization, which introduced new grains to replace the deformed/enlongated grains, could occur during the LTC process.

As seen in Figure 3.2, the intensities of {111} and {200} peaks are similar after LTC, while the intensity of {111} peak is higher than that of {200} peak, indicating that orientation of grains in AL-6XN changed after LTC. As mentioned in the previous paragraph, recrystallization could occur during the LTC process.

Broadening is seen in all X-ray diffraction patterns of CSS-engineered Fe–Cr–Ni alloys. This is probably due to the different carbon concentration at different surface

depth, leading to a continuous variation of lattice parameter a. The broadening can also be partially attributed to crystal defects (dislocations), which builds up at the carburized near-surface region. In addition, the asymmetric {111} and {200} peaks seen in the LTC AL-6XN specimen (Figure 3.2) was most likely due to the gradient carbon concentration distribution in the near-surface region. The carbon concentration in the near-surface region of LTC AL-6XN can reach 20 at%, which was 5 at% more than that of LTC AISI-316L. This higher C concentration in the near-surface region of carburized AL-6XN introduced more lattice parameter expansion and asymmetry compared to carburized AISI-316L. As a result, 2θ shifted to lower angles compared to those of carburized AISI-316L.

4.2.4 Carbon Concentration Dependent Carbon Diffusivity

Sharghi-Moshtaghin *et al.*[21] reported that the 'effective' carbon diffusivity at 780 K in IN-718 is close to that at 720 K in AISI-316L. With the same carbon diffusivity, similar thickness of carburized near-surface region can be generated after the LTC treatment with similar processing time.

Assume that the carbon infusion process can be predicted by Fick's second law, which assumes that the carbon diffusivity is independent of carbon concentration. Seen from Figure 3.12, case depths of 22 μm, 23 μm and 20 μm are achieved after the LTC process for AISI-316, AL-6XN and IN-718, respectively. The diffusivities of carbon at the carburization temperature (720 K for AISI-316L and AL-6XN and 780 K for IN-718) in AISI-316L, AL-6XN and IN-718 can be calculated with the following diffusion equation:

$$x = \sqrt{D_C t}, \tag{4.1}$$

where x is the diffusion distance, D_C is the diffusivity of carbon and t is the diffusion time (72 ks for carburizing AISI-316L and AL-6XN and 100.8 ks for carburizing IN-718).

According to this equation, the diffusivities of carbon at the carburizing temperature in AISI-316, AL-6XN and IN-718 are 6.7×10^{-15} m^2/s, 7.3×10^{-15} m^2/s and 4×10^{-15} m^2/s. However, Ernst[68] *et al.* found that the dilute carbon diffusivity, which is independent of carbon concentration,[69] at 720 K in AISI-316L is only 9.1×10^{-17} m^2/s, which is two orders lower compared to the ones calculated with the diffusion equation. This data indicated the carbon diffusivity in the carburized AISI-316L is carbon concentration-dependent. Ernst[68] *et al.* also reported that the higher the carbon concentration, the larger the carbon diffusivity in the carburized near-surface zone. Ge[35] found that both the depth of carburized and nitrided near-surface regions on AISI-316L are proportional to the square root of time, regardless of whether the carbon diffusivity is dependent or independent of carbon concentration. However, if it is already known that carbon diffusivity is dependent on carbon fraction in a AISI-316L specimen, this 'carbon diffusivity' calculated with the diffusion equation (4.1) is the 'effective' carbon concentration-dependent carbon diffusivity and should be larger than the dilute carbon diffusivity at the same carburizing temperature in AISI-316L. Although the calculated 'carbon diffusivity' does not change with the carbon concentrations, it can still represent the 'effective' value of the carbon concentration dependent on carbon diffusivity. Therefore, this 'effective' carbon diffusivity will be used in the following discussion sections.

As seen in Figure 3.12a and b, the carbon concentration profile of low-temperature carburization AISI-316L and AL-6XN has a concave shape, indicating the carbon diffusivity in these two carburized samples is strongly dependent on carbon concentration. In addition, the carbon diffusion coefficient in LTC stainless steels is several orders of

magnitude larger than that of non-treated one.[28] The most likely explanation for the strong increase is that carbon-induced local expansion of metal-metal atom distances, which is observed as an expansion of the lattice parameter, reduces the activation energy for carbon diffusion.[68,70] On the other hand, the shape of carbon concentration profile of carburized and nitro-carburized IN-718 is less concave-like, suggesting that carbon diffusivity is less carbon concentration-dependent in carburized and nitro-carburized IN-718 specimens. IN-718 and AISI-316L specimens can have a case with the thickness of 7 μm and 22 μm, respectively, after a low-temperature carburization process at 720 K for 72 ks. According to the diffusion equation, the effective diffusivities of carbon in carburized IN-718 and AISI-316 are 6.8×10^{-16} m^2/s and 6.7×10^{-15} m^2/s, respectively. The effective carbon diffusivity in IN-718 is one order lower than that of AISI-316L at the same carburizing temperature (i. e. 720 K).

Another thing should be concerned is that orientation of AISI-316 crystal also has an effect on the diffusion coefficient of nitrogen, which can cause various case depths in different crystal orientations.[36] The intensity of non-treated AISI-316L {200} is higher than that of {111} in Figure 3.1, indicating that the grains with this specific orientation are preferred in the non-treated AISI-316L. According to data of Wu,[36] the nitrided near-surface region of AISI-316L along {111} planes is 50% (15 μm) more than that (10 μm) along {200} planes. However, this effect was not observed on any carburized Fe–Cr–Ni alloys, indicating that carbon diffusivity is independent of the orientation of AISI-316L grains.

4.2.5 Cr Loss during Carburization

Since no water vapor is involved in the annealing process, no Cr loss is detected in the annealed but not carburized IN-718 specimen, as seen in Fig 3.13, but Cr depletion is

clearly observed in the LTC and LTNC IN-718 samples. Therefore, it is concluded that Cr loss in surface-engineered IN-718 specimens must be related to three aspects: (1) the presence of water vapor, (2) Cr fraction dependence of driving force for the diffusion of Cr atoms (the higher the Cr fraction is, the higher the driving force could be) and (3) carburization time (longer time means more Cr loss).

Figure 3.12 suggested that Cr depletion was observed for all of the CSS-engineered Fe–Cr–Ni alloys. AISI-316L contains 18 at% of Cr, while AL-6XN and IN-718 contain 24 at% and 21 at%, respectively. Furthermore, the carburizing temperature (720 K) is lower than that (780 K) of IN-718. Therefore, carburized AISI-316L has the least Cr depletion (only 1 at% of Cr depletion was detected in the carburized region). Carburized AL-6XN has 4 at% of Cr loss in the carburized near-surface zone. Although AL-6XN contains more Cr than IN-718, the carburizing temperature (720 K) for AL-6XN is lower than that of IN-718. It seems that the carburizing temperature, while compared to Cr fraction, plays a more important role to determine the Cr diffusivity/mobility in the Cr depletion process in similar carburization times. Finally, nitro-carburized IN-718 has the most significant depletion of Cr. Around 12 at% of Cr loss was found in the carburized near-surface region. Nitriding might be the reason that more Cr loss was observed in LTNC IN-718.

Possible Reactions in the CSS-engineered Process. Strong evidence of Cr depletion in the carburized near-surface region was detected in Figure 3.12, implying that the Cr diffusivity is larger than expected in the carburized surface at the carburizing temperature. This phenomenon is reasonable because the existence of metal vacancies, induced by Cr evaporation, enhances the Cr diffusivity.

Astem *et al.*[71] reported that evaporable $CrO_2(OH)_2$ is formed by placing AISI-304L at 870 K in the presence of water vapor. The chemical reaction of forming $CrO_2(OH)_2$ can be written:

$$\frac{1}{2}Cr_2O_3(s) + \frac{3}{4}O_2(g) + H_2O(g) \rightarrow CrO_2(OH)_2(g)\,. \tag{4.2}$$

It is very clearly shown in this equation that oxygen is a necessary reactant, implying that oxygen is present during the low-temperature carburization process. Oxygen can come from two possible sources: (1) oxygen and H_2O impurities in the high purity gas (i. e. H_2) and (2) oxygen produced by the following reaction with the catalysis of Fe–Cr–Ni alloys.

$$2CO(g) = 2C(s) + O_2(g)\,. \tag{4.3}$$

Then carbon atoms diffuse into the Fe–Cr–Ni specimens and oxygen could become the required reactant for forming $CrO_2(OH)_2$ or further oxidize the Fe–Cr–Ni samples with the following equation:

$$4Cr(s) + 3O_2(g) = 2Cr_2O_3(s)\,. \tag{4.4}$$

But considering the large scale of Cr depletion from Figure 3.12c, it is unlikely that the oxygen and water vapor, required for such a large scale of Cr depletion, comes from impurities (H_2O and O_2) with extremely low concentration (i. e. 5 ppm). It is highly possible that oxygen is produced by the above reactions. Christiansen *et al.* reported that supplying CO after the activation process can successfully carburize AISI-316 specimen,[72] indicating CO decomposing into C and O_2 is possible in the carburizing process. Meanwhile, water vapor is produced by the reaction written in the bottom:

$$CO(g) + H_2(g) = 2C(s) + H_2O(g)\,. \tag{4.5}$$

Based on the above discussion, it can be concluded that during the low-temperature-carburization process, H_2O and O_2 will react with Cr_2O_3 forming $CrO_2(OH)_2$ vapor, providing a large driving force for the diffusion of Cr atoms. Researchers at CWRU have investigated gas-phase based low-temperature carburization for more than a decade, yet are still struggling with the reactions that are actually happening in the carburizing process.

With the observation of chromium depletion after low-temperature carburization, several possible reactions in the carburization process were confirmed experimentally. A small amount of acetylene should be added in future carburization processes to prevent the oxidation happening during low-temperature carburization. In addition, no Cr loss was detected for the annealed-only IN-718, shown in Figure 3.13, suggesting that without the existence of H_2O during annealing, no Cr loss was observed. The lattice parameter of non-carburized face centered cubic (FCC) IN-718 is 0.3604 nm calculated from the XRD pattern in Figure 3.3. The lattice parameter of carburized IN-718 is 0.3692 nm, which is a 2.5% expansion compared to the lattice of non-carbruized IN-718 despite strong evidence of Cr depletion in the carburized near-surface region. Much larger lattice parameter expansions can be expected if no Cr depletion existed. Therefore, the high diffusivity of Cr at the carburization temperature in the case is mainly resulted from the following perspectives:

(1) The formation of $CrO_2(OH)_2$ gives a large driving force for Cr atoms diffusing.

(2) Higher carburizing temperatures yield higher Cr diffusivities.

(3) Metal vacancies introduced by Cr depletion will also increase the diffusivity of Cr.

AL-6XN was carburized with acetylene and no oxygen is even involved in the low-temperature carburization process, yet Cr depletion was seen in Figure 3.12b. However, acetylene, which is used to carburize AL-6XN, is mixed with 4 vol% of acetone to stabilize it, so acetone is present in the acetylene in the carburizing process. According to Rice *et al.*[73], acetone can be decomposed into a gas mixture containing CO at 770 K for only 180 s. However, the AL-6XN specimen was carburized at 720 K, lower than the temperature, at which acetone decomposes. As discussed before, a well activated AISI-316L can be carburized with CO gas. The Gibbs free energy for CO decomposing to C and O_2 at 720 K is 350 KJ/mol, calculated with the thermodynamic data published by Chang.[74] The reaction was possible in the carburization process of AISI-316L, implying that AISI-316L, AL-6XN and IN-718 alloys are actually acting as catalyst to make this chemical reaction happen in the carburization process. It is also can be expected that acetone decomposed at the carburizing temperature 720 K with the help of the AISI-316L, AL-6XN and IN-718 alloys.

Atomistic Model for Simultaneous Carbon Infusion and Cr Depletion. Regarding the processes that occur in the Fe–Cr–Ni alloys at the atomistic level, Figure 4.2 indicates that three processes occur simultaneously:

(1) Cr atoms evaporate by forming volatile $CrO_2(OH)_2$. This generates a gradient in Cr chemical potential towards the surface. It also generates an increased concentration of vacancies on regular lattice sites – and a corresponding gradient in vacancy chemical potential towards the alloy interior.

(2) The chemical potential gradient generated by Cr loss of the surface causes Cr atoms deeper below the surface to diffuse toward the surface. The gradient in vacancy chemical potential causes vacancy diffusion into the alloy.

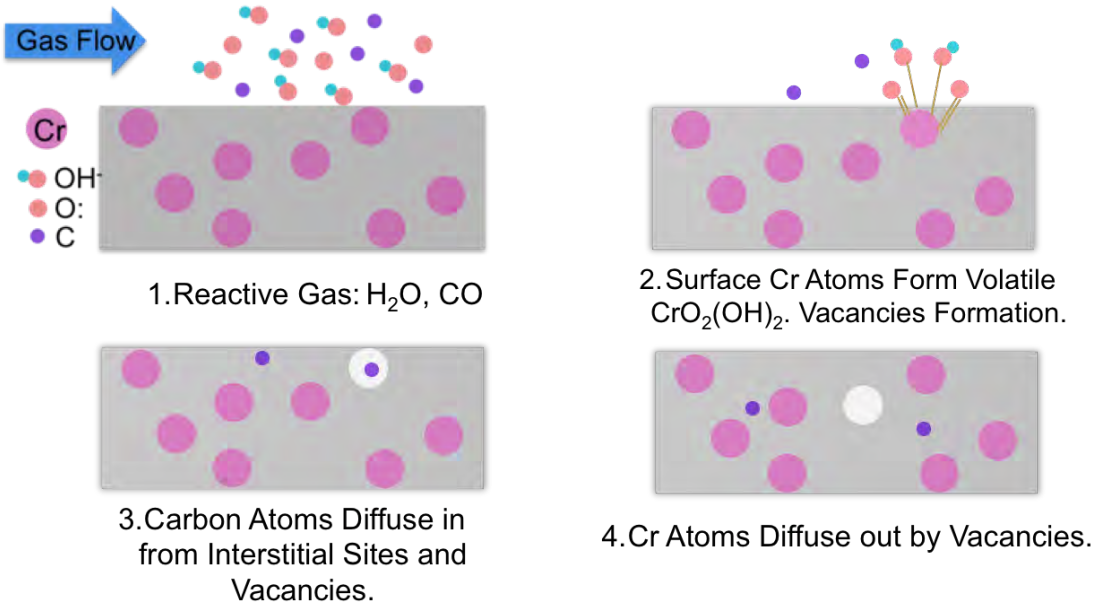

Figure 4.2. Micro-mechanism for carbon diffusing inward and chromium diffusing outward the lattice of Fe–Cr–Ni alloys.

(3) Carbon atoms diffuse into the alloy through interstitial sites – as before – and possibly also with the help of Cr vacancies.

Sharghi *et al.*[21] reported that the carbon diffusivity in IN-718 at 780 K is similar to that in AISI-316 at 720 K. However, the shape of the carbon-concentration –depth profile shown in Figure 3.20c is less concave than the profile of AISI-316L and AL-6XN. This means that the depletion of Cr decreases the concentration dependence that is normally observed for diffusion of carbon in IN-718. On the other hand, the profile in Figure 3.20d is more concave than that in Figure 3.20c. This suggests that Cr vacancies enhance the concentration dependence of carbon diffusivity in IN-718. However, the profile in Figure 3.20d is less concave than those in Figures 3.20a and b. This confirms that the presence of Cr is the most important reason for carbon to diffuse into IN-718. While the diffusivity of carbon also increased by the vacancies diffusing into the alloy, the most

important parameter for carbon diffusivity is the level of carbon itself, which (under otherwise constant conditions) increases with the Cr fraction. This explains the following observations:

(1) Different alloys, processing temperature, and time produce different initial surface (maximum) carbon concentrations in these alloys. The carbon concentration at the surface of surface-engineered IN-718 will be highest without Cr depletion.

(2) A concave carbon concentration profile means that the carbon diffusivity increases with carbon concentration.

(3) At the same carbon concentration, the diffusion distance of carbon in nitro-carburized IN-718 is larger than that of carbon in carburized IN-718. This means that the carbon diffusivity in nitro-carburized IN-718 is higher than in carburized IN-718 and the increase of carbon diffusivity is probably correlated with an increased concentration of metal vacancies. (The carbon profile in Figure 3.20d is more concave-like than that in Figure 3.20c.)

4.2.6 Ferromagnetism of LTC and LTNC IN-718

No ferromagnetism was detected in LTC AISI-316L and AL-6XN, however, strong ferromagnetism was observed in the first 5 μm and 7 μm of case in carburized and nitro-carburized IN-718, respectively. Possible reasons inducing ferromagnetism in the case of carburized and nitro-carburized IN-718 are discussed herein.

The TTT diagram of IN-718[21] implied that there will be no precipitates at the carburizing temperature (780 K) for ten thousand hours. The Curie temperatures for the

solutionized and aged IN-718 are 80 K and 160 K,[75] respectively, meaning that both solutionized and aged IN-718 are paramagnetic materials at room temperature. Since even the high temperature aged IN-718 with precipitates is paramagnetic at room temperature, the carbide- and precipitate-free IN-718 after annealing at the carburizing temperature 780 K (several hundred K lower than the aging temperature) for 100.8 ks should be paramagnetic at room temperature as well. It can clearly be seen in Figure 3.17, that the non-carburized matrix of IN-718 remains paramagnetic. However, the first five micrometers of the carburized surface of IN-718 show strong evidence of ferromagnetism, seen in Figure 3.17. Wu *et al.*[76] found the first few micrometers of low-temperature-nitrided AISI-316L become ferromagnetic due to the expansion of lattice with interstitial N atoms. Wu concluded that 5% of lattice parameter expansion is needed before ferromagnetism can be detected in AISI-316L.

When the concentration of Cr in Cr–Ni alloy increases to 10 at%, the Curie temperature decreases below the room temperature, implying that the Cr–Ni alloy with 10 at% of Cr is paramagnetic at room temperature.[77] Takahashi *et al.* found if Cr concentration dropped below 10 at%, the $Ni_{76+x}Cr_{16-x}Fe_8$ (IN-600) alloy will become ferromagnetic at room temperature.[78] It is possible that 10 at% of Cr will be the threshold for keeping the IN-718 specimen paramagnetic. The first five micrometers became ferromagnetic after carburization, as shown in Figure 3.17b. The Cr concentration in the outermost ferromagnetic surface of LTC IN-718 is around 12 at%, and is 17 at% at the end point (5 μm against the outermost ferromagnetic surface) where ferromagnetism ceases. Therefore, Cr depletion in IN-718 is not the reason for the ferromagnetism in LTC IN-718.

With the increase of C and N atoms in the matrix of AISI-316L and the expansion of the lattice parameter of nitrided AISI-316L, the electronic structure of AISI-316L gradually changed. Ferromagnetism in LTC and LTNC IN-718 could be introduced by the change of electronic structure of IN-718 after C and N atoms infused. There will be certain amount of C and N atoms needed to generate ferromagnetism in IN-718. Since the more the C and N atoms infused in the lattice of IN-718, the more lattice expansion they can cause. In other words, certain lattice expansion (certain concentration of C and N) is needed to turn the paramagnetic IN-718 to ferromagnetic IN-718.

In terms of the depletion of Cr observed in LTC IN-718, the actual lattice parameter expansion rate of carburized IN-718 is much higher than the expansion of 2.5%. In Figure 3.22c, the lattice of carburized IN-718 shrank after annealing at 1070 K for 3.6 ks. It is should be noted that carbon atoms still reside in the lattice after this heat-treatment, even though some ($\leqslant$ 5 vol%) nano-sized chromium carbides can be seen under TEM, which cannot be detected with XRD, indicating the lattice can further shrink. Chen *et al.*[79] predicted that the lattice of Ni–Cr alloy changed by 0.002 nm by increasing the Cr concentration from 10 at% to 20 at%. Nammas *et al.*[80] also found a lattice increase of Fe–Ni–Cr alloy by 0.002 nm after the Cr concentration changed from 10 at% to 20 at%. Therefore, the predicted lattice parameter expansion caused by carbon infusion, considering the loss of Cr is 3.1%, but since the lattice of IN-718 can further shrink as discussed before, the actual expansion of the IN-718 lattice parameter could be larger. The amount of C and N atoms, which caused lattice expansion, might be enough to cause ferromagnetism in IN-718. In addition, Cao *et al.*[33] found a linear relationship between the lattice parameter of austenite and carbon solute fractions:

$$a^{\gamma} = a_0^{\gamma} + \alpha X_{\mathrm{C}}^{\gamma}. \tag{4.6}$$

where a^{γ} is the lattice parameter of austenite after carburization, a_0^{γ} is the lattice parameter of austenite before carburization, X_C^{γ} is the carbon fraction in the austenite and α is the expansion coefficient (0.00104 nm/at%). 18 at% of carbon can produce a lattice parameter expansion of 0.02 nm, which is a 5.2% of expansion compared to the lattice parameter (0.358 nm) of non-treated IN-718. Making paramagnetic high Cr fraction alloys ferromagnetic may have some interesting applications in the future.

The LTNC IN-718 also showed ferromagnetism in the first 7 μm of the nitro-carburized near-surface region, however, the mechanism for ferromagnetism detected in this near-surface zone is different than that of carburized near-surface region. As seen in Figure 3.17d, the ferromagnetism of the outermost 2 μm, where the material is rich in nitrogen, is not obvious. Figure 3.13 implies that the Cr concentration of LTNC IN-718 in the first 2 μm is around 9 at% to 10 at%, which is the possible threshold for maintaining IN-718 alloy paramagnetic. Furthermore, Figure 3.3 indicated that the lattice of IN-718 alloy is contracted compared to that of non-treated IN-718 after the LTNC process. Considering the penetration of X-ray is around several micrometers, it is concluded that the signal of lattice parameter contraction was collected from the nitrogen-rich case. If the first 2 μm of the nitrogen-rich region is polished off, the lattice parameter expansion induced by carbon infusion can be detected. Based on the discussion above, it is reasonable that ferromagnetism in the first 2 μm of nitro-carburized near-surface region is not observed. On the other hand, strong ferromagnetic patterns were detected in the nitro-carburized region from 2 μm through 7 μm, where the material is rich in carbon. Ferromagnetism in this region is also introduced by the infusion of C atoms and expansion of the lattice, which changed the electronic structure of LTC IN-718, in the LTNC process.

4.3 Oxidation Tests

4.3.1 PCHE-A

No significant difference from the metallographic images and hardness profiles after the PCHE-A process are shown compared to those of the as-carburized Fe–Cr–Ni alloys in Figure 3.19 and Figure 3.21. The X-ray diffraction patterns of LTC and LTNC Fe–Cr–Ni alloys after the PCHE-A treatment in Figure 3.18 indicated no precipitates (oxides, carbides and nitrides) in any of these alloys, implying that carburized Fe–Cr–Ni alloys were fairly stable at 620 K for a short period of time (i. e. 86.4 ks). Actually, the case of carburized AISI-316L can remain carbide-free for years at 620 K (working temperature of BWR) if temperature is the only factor considered in annealing.[28] Wang *et al.* reported that carburized AISI-316L remained carbide-free after annealing at 650 K for 20.7 Ms (8 months).[81]

Figure 3.20 does not reveal obvious changes in either C or Cr fraction depth profiles for Fe–Cr–Ni alloys after the PCHE-A treatment, suggesting that both carbon and chromium diffusivities at 620 K are so low that no noticeable difference can be seen within 86.4 ks. The carbon dilute diffusivity, extrapolating from data of Ernst *et al.*,[68,69] is 1.3×10^{-18} m^2/s at 620 K in AISI-316L specimen. The diffusion distance (0.34 μm) of carbon atom is calculated with the diffusion equation (4.1). Sharghi-Moshtaghin[21] pointed out that the diffusivity of Cr in Ni is at least 4 orders lower than that of C in Ni at the carburizing temperature (i. e. 780 K). Therefore, it can be expected that the chromium diffusivities in Fe–Cr–Ni alloys at 620 K should also be smaller than the carbon diffusivity at this temperature and no change of Cr fraction depth profile should be observed, which is exactly the case seen in Figure 3.20. Although there are no variations (case

depth, carbon concentration *etc.*) seen between as-carburized and low-temperature-short-time annealed (i. e. 620 K for 86.4 ks) Fe–Cr–Ni alloys, Wang reported that the case depth of carburized AISI-316L is doubled (50 μm) after annealing at 650 K for 20.7 Ms.[81] In this case, the effective carbon diffusivity calculated from the diffusion equation (4.1) is 1.6×10^{-2} m^2/s. By applying this carbon concentration-dependent carbon diffusivity back to the diffusion equation (4.1), it is found that the carbon only diffused 4 nm in AISI-316L after PCHE-A process, which agreed well with the coinciding carbon profiles of as-carburized and PCHE-A processed AISI-316L in Figure 3.20.

4.3.2 PCHE-B

Metallography. The featureless band from LTC and LTNC Fe–Cr–Ni alloys seen in Figure 3.4a-d turns into black/dark layers as shown in Figure 3.23a-d after PCHE-B-Air heat treatment. These black/dark layers are not featureless anymore. Grain boundaries can been easily seen in the black/dark layers of LTC AISI-316L and AL-6XN. Conclusions can be made that black/dark layers instead of featureless bands appear when the corrosion resistance of featureless bands is more or less compromised. The LTC AISI-316 and AL-6XN showed more features compared to LTC and LTNC IN-718, indicating that the corrosion resistance of LTC AISI-316L and AL-6XN is attenuated more in comparison with that of LTC and LTNC IN-718. The metallographic images of PCHE-B-Vac processed LTC and LTNC Fe–Cr–Ni alloys showed similar black/dark layers, implying that the corrosion resistance of LTC and LTNC Fe–Cr–Ni alloys decreased.

Oxides and Carbides. The X-ray diffractogram of LTC AISI-316L in Figure 3.22a indicated that the surface of LTC AISI-316L is covered by different kinds of oxides after PCHE-B-Air test, implying that the high temperature oxidation resistance of LTC AISI-316L is not good. It can be clearly seen in Figure 3.24a that an oxide layer as thick as 12 μm

is formed after the PCHE-B-Air heat treatment, suggesting LTC AISI-316L will rapidly oxidize under LCA. The oxide layer on the surface of the AISI-316L sample is so thick (12 μm) that X-rays cannot penetrate though to obtain the carbide signals beneath the oxide layers. However, carbides were expected to be present due to the high annealing temperature (i. e. 1070 K) and the high affinity of chromium to carbon. Moreover, this oxide layer can be clearly seen in the SEM image of Fig 3.25 and was confirmed to have very high hardness (i. e. around 14 GPa in the first 12 μm of the surface of LTC AISI-316L after the PCHE-B-Air annealing process) seen in Figure 3.35a.

On the other hand, the SEM image in Figure 3.27 showed that two oxide layers, with the total thickness of 5 μm, formed on the surface of LTC AL-6XN after the PCHE-B-Air process. Figure 3.29 suggested that layer 1 was dominated by Fe- and (Fe,Ni)-oxides, while layer 2 mainly contained Cr oxide with smaller grains in comparison with that in layer 1. However, SAM did not collect any oxygen signals from the first 5 μm of the surface on the AL-6XN specimen. Since there are 128 data points distributed in 40 μm, the distance between each data point is 0.3 μm, which is around one twentieth of the thickness (5 μm) of the oxide layers on the AL-6XN, indicating SAM should not miss these oxygen signals if the oxide layers were on the surface of AL-6XN specimen. Therefore, porosity is most likely the nature of these oxide layers and they were easily peeled off during the sample preparation process (mounting, polishing and demounting *etc.*) for SAM. Fig 3.22b implied that oxides and carbides were detected on the surface of LTC AL-6XN after the PCHE-B-Air test. The oxide layers on the surface of AL-6XN were thin (5 μm) enough for the X-ray to penetrate through to collect the carbide signal below them. However, carbides rather than oxides were observed on the surface of LTC AL-6XN

after PCHE-B-Vac process, meaning carbides are more than 5 vol% so that they could be detected.

Furthermore, Fig 3.22d indicated that oxide was clearly seen on the surface of LTNC IN-718 after the PCHE-B-Air test, implying that the thickness (i. e. $> 5\,\mu m$) of the oxide layer is comparable with the penetration depth of the X-ray. However, oxygen signals were not picked up in Figure 3.24d. Considering the oxide layer on the surface of IN-718 can be as thick as 5 μm, SAM cannot miss this layer since it is known that the distance between two data points is only 0.3 μm, which is much smaller in comparison with the thickness of the oxide layer. Therefore, the most plausible explanation for the absence of the oxygen signals in Figure 3.24d would be that the porous oxide layer had peeled off during the sample preparation process. A film-like foil is observed in the epoxy after AL-6XN and IN-718 specimens were removed. Another thing should be noticed in Fig 3.22d is that carbides were not shown on the surfaces of both LTC IN-718 specimens after the PCHE-B-Air and PCHE-B-Vac heat treatments, meaning that the volume percentage of carbides in the case is less than 5 vol% (the detection limit of XRD).

Finally, an oxide layer with thickness of 100 nm to 500 nm is generated on the surface of LTC IN-718 after air-1070 K annealing, as shown in Figure 3.32. This is expected because Cr loss occurring during low-temperature carburization will impair the oxidation resistance of carburized IN-718. The oxide layer of LTC IN-718 is the thinnest among all LTC and LTNC Fe–Cr–Ni alloys after the PCHE-B-Air heat treatment, implying that LTC IN-718 possessed the highest oxidation resistance at 1070 K among all surface-engineered Fe–Cr–Ni alloys. However, this oxide layer with thickness of 100 nm to 500 nm is probably a dense Cr-rich oxide layer, which can prevent the further oxidation of LTC IN-718.

Fig 3.22c did not show any extra peaks other than the {111} and {200} ones. Since the penetration depth of X-rays are several micrometers (i. e. 5 μm to 10 μm), an oxide layer with the thickness of 200 nm is only 4 % of the X-ray penetration depth. It is reasonable that the oxides peaks did not show up in Fig 3.22c.

Moreover, the STEM image of Fig 3.31 clearly showed nano-sized carbides, confirmed by EFTEM (energy filtered transmission electron microscopy) imaging in Figure 3.34, formed below the oxide layer. However, carbide peaks were absent in LTC IN-718 samples after both PCHE-B-Air and PCHE-B-Vac tests seen in Fig 3.22c, indicating that the fraction of these nano-sized carbides in the case is less than the detection limit of XRD.

The lattice of surface-engineered AL-6XN and IN-718 has contracted compared to those of non-treated AL-6XN and IN-718, shown in Fig 3.22, after the PCHE-B-Air and PCHE-B-Vac treatments. As discussed previously, Cr was depleted from the lattice of LTC IN-718 by forming nano-sized chromium carbides, which has a smaller lattice in comparison with that of non-carburized IN-718. The formation of nano-sized chromium carbides is one of the factors resulting in the contraction of the lattice shown in Figure 3.22c. The X-ray diffraction pattern of the non-carburized-1070 K-annealed IN-718 showed no peak shifts compared to non-carburized IN-718, illustrating that if no carbides form, there will be no lattice parameter contraction, but that does not mean non-carburized IN-718 specimen has better performance than a carburized IN-718 sample under the loss of coolant accident. On the contrary, carburized IN-718 will perform better than the non-carburized specimen in a loss of coolant accident because of the following reason:

(1) The formation of nano-sized chromium carbides slightly change the chromium distribution in the case area, so the corrosion resistance will be mostly maintained. Carbon atoms reside in the interstitial position also act in a role as to preventing the depletion of chromium by forming nano-sized chromium carbides in a loss of coolant accident.

Carbon Loss. Figure 3.24 indicated carbon loss was observed in the first several micrometers (i. e. carbon concentration reached the maximum around 5 μm for LTC AISI-316, 10 μm for LTC AL-6XN and 5 μm for LTC and LTNC IN-718) of the carbon-rich region in all CSS-engineered Fe–Cr–Ni alloys after both PCHE-B-Air and PCHE-B-Vac processes. Decarburization was first observed in air-1070 K annealed LTC IN-718. To determine whether the driving force for the carbon loss is caused by forming CO_2 with the oxygen in air, LTC was exposed at 1070 K for 3.6 ks under vacuum conditions (2 Pa). However, this vacuum container might have enough oxygen molecules to introduce the carbon loss, as shown in Figure 3.24d.

It is well known that the hardness of the carburized near-surface region is tripled in comparison with that of the core, seen in Figure 3.14, so it should be expected if the hardness decreases after the carbon depletion. As seen in Figure 3.35, the hardness profiles of the LTC IN-718 after the PCHE-B-Air and PCHE-B-Vac tests suggested that the first five micrometers of the carbon-rich area decreased compared to that of LTC IN-718, and the maximum hardness presented at around 5 μm, which agrees well with the SAM data shown in Figure 3.24. Furthermore, it is also well known that interstitial carbon atoms cause lattice parameter expansion of the Fe–Cr–Ni alloys, so lattice parameter contraction seen in Figure 3.22b-d is also expected when carbon loss is clearly shown in Figure 3.24b-d.

However, based on the data in this thesis, the lattice parameter contraction of the surface-engineered AL-6XN and IN-718 after the PCHE-B-Air and PCHE-B-Vac is not merely dependent on carbon loss seen in Figure 3.24b-d but also relates to two other major factors:

(1) Cr depletion, as shown in Figure 3.12b-d, during the LTC process already resulted in lattice parameter contraction of AL-6XN and IN-718 in the first place, however, this lattice parameter contraction was compensated by lattice parameter expansion by interstitial carbon atoms.

(2) Chromium carbides, confirmed with XRD and EFTEM imaging in Figure 3.22 and Figure 3.34, further depleted the Cr from the matrix of AL-6XN and IN-718, so the lattice of AL-6XN and IN-718 further contracted.

4.4 SCC

It is already well known that surface-engineering can improve the corrosion resistance of Fe–Cr–Ni alloys. Moreover, surface-engineered Fe–Cr–Ni alloys introduced compressive stresses (as high as 2 GPa), which can keep cracks closed and presumably increase the SCC resistance of Fe–Cr–Ni alloys in the carburized near-surface zone. However, tensile stresses applied on the Fe–Cr–Ni alloys tends to make these cracks open. Under this condition, carburized Fe–Cr–Ni alloys were susceptible to SCC.

Tensile tests on AISI-316L and IN-718 dog bones (rod) and tube specimens were performed. Wei Niu from the University of Akron collected the tensile test data for rod samples and the tensile tests on AISI-316L and IN-718 tube specimens were carried out at CWRU. Figure 4.3 reveals that carburization strengthened AISI-316L and reduced the strain to failure of AISI-316L when the tensile test was performed in air.

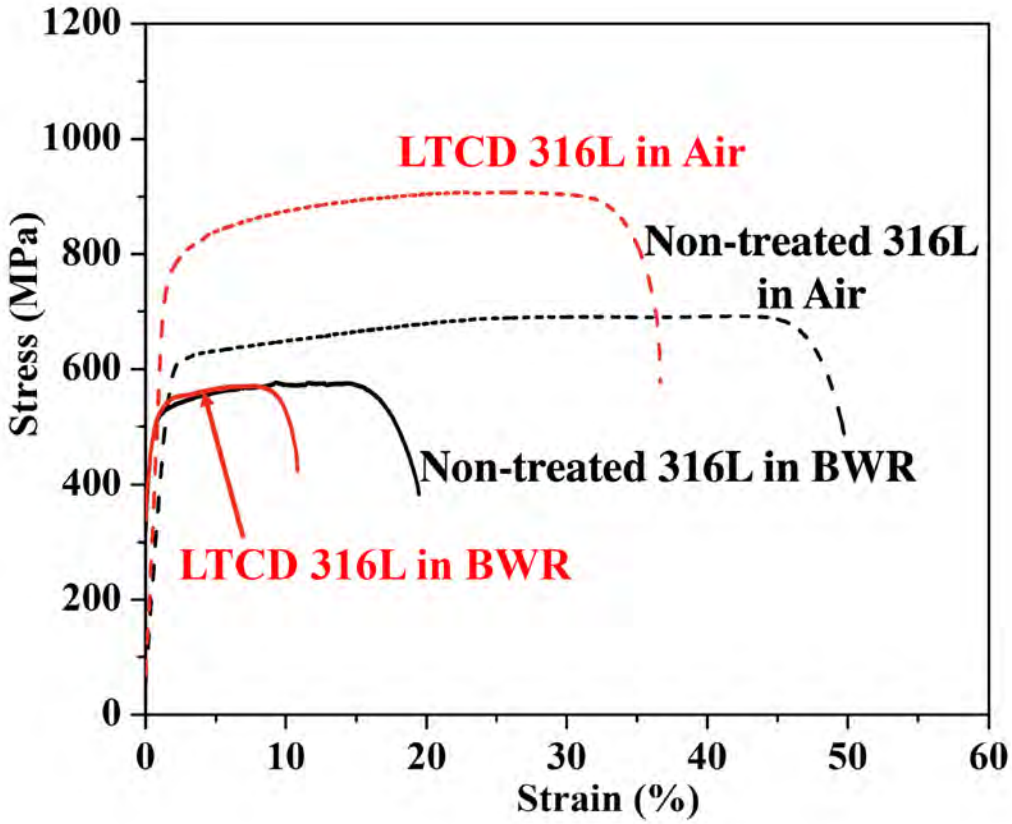

Figure 4.3. Stress-strain curves of non-treated and carburized AISI-316L in air and BWR.[82]

Figure 4.3 indicated that carburization strengthened AISI-316L tensile bar (UTS (ultimate tensile strength) increased from 600 MPa to 850 MPa) and reduced the strain to failure. Tensile tests of tubes also suggested a similar effect of carburization on AISI-316L tubes, as shown in Figure 3.15. However, Figure 3.15 also indicated that the AISI-316L tube sample, annealing at the carburizing temperature for 72 ks but without supplying carburizing gas, showed a reduction of the strain to failure when compared to that of non-treated AISI-316L tube. Furthermore, Michal *et al.*[27] reported that the annealed but not carburized AISI-316L showed an increase of UTS and a reduced strain to failure. The

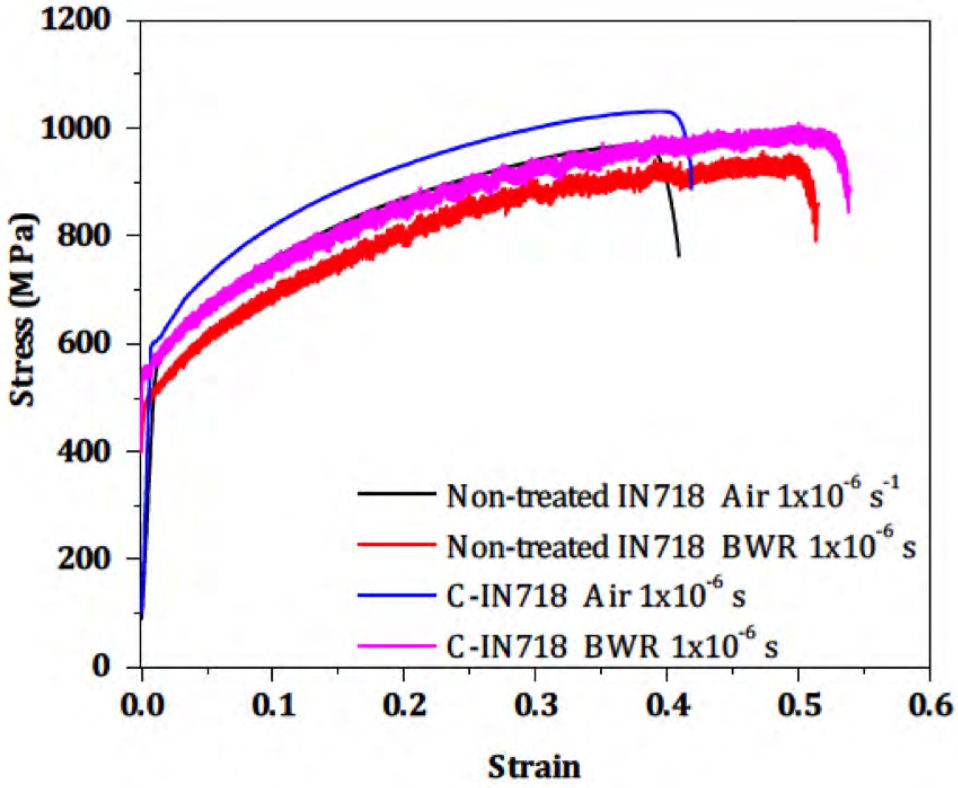

Figure 4.4. Stress-strain curves of non-treated and carburized IN 718 in air and BWR.[82]

most possible reason causing this strengthening effect is dynamic strain aging, which is commonly observed in AISI-316L[83] and IN-718[84] alloys and is introduced by carbon interstitials pinning and inhibiting the movement of dislocations in the AISI-316L specimen. However, this improvement of UTS by annealing/carburization was compromised (UTS of carburized AISI-316L tensile bar is equal to that of non-treated one) while the tensile tests were applied in a BWR simulated environment as seen in Figure 4.3. Moreover, the 10% strain to failure of carburized AISI-316L tested in BWR simulated environment was significantly decreased compared to that of non-treated AISI-316L specimen

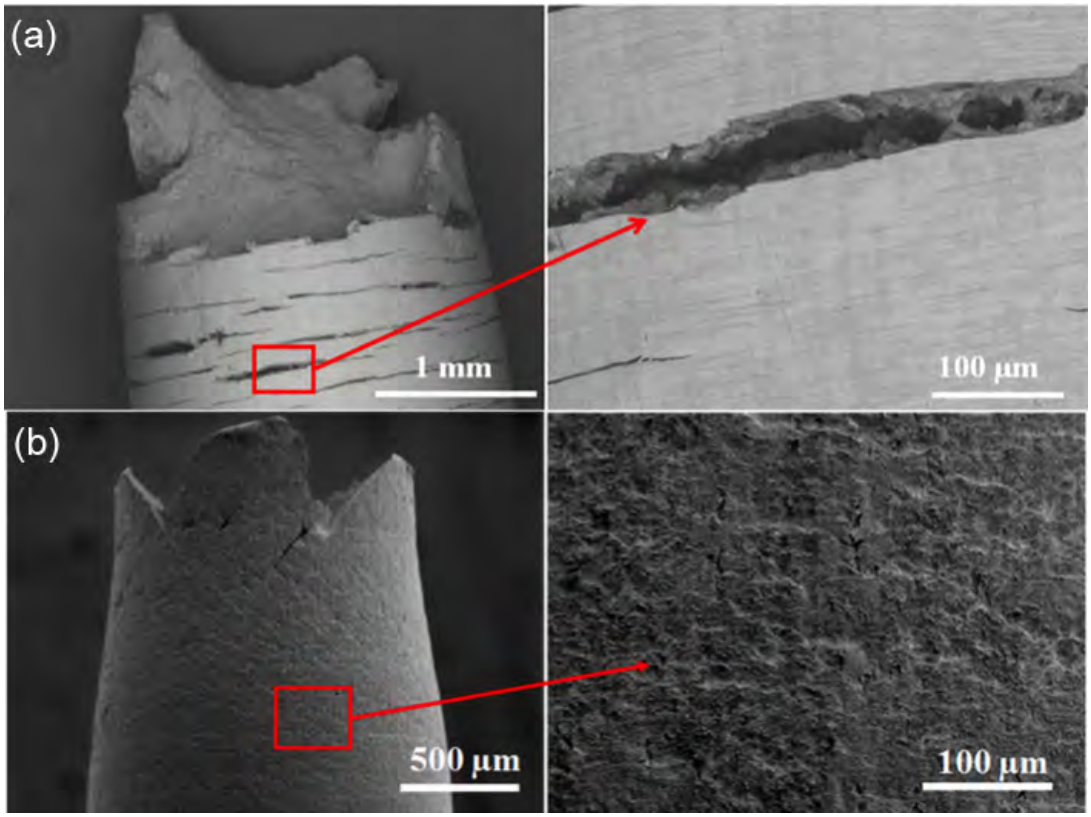

Figure 4.5. SEM image of tensile rod after failure at a BWR simulated environment (a) LTC AISI-316L and (b) LTC IN-718.[82]

tested in BWR simulated environment and to those of non-treated (50%) and carburized (35%) samples tested in air. Finally, Niu[82] reported that it is lack of dimples in the case area of LTC AISI-316L after testing in the BWR simulated environment. Long and deep cracks that penetrated the case and propagated into the core of AISI-316L tensile bar were observed after the tensile test in BWR simulated environment, as seen in Figure 4.5a. Summarizing, all the evidence suggested that the SCC resistance of LTC AISI-316L is not improved by low-temperature carburization.

In contrast, LTC IN-718 tensile bars have better mechanical properties (i. e. higher UTS and larger strain to failure) than those of non-treated IN-718 samples, regardless whether the tensile tests were performed in air or in BWR simulated environment, as

seen in Figure 4.4. The carburized IN-718 tested in the BWR environment even held the best strain to failure among all the specimens shown in Figure 4.4. Again, Figure 3.15b indicated that the annealed-only IN-718 is strengthened (higher UTS, 900 MPa) compared to the non-treated IN-718 (850 MPa) but interestingly the strain to failure of annealed IN-718 is increased in comparison with that of non-treated IN-718. The strengthening effect after the annealing process can be explained by dynamic strain aging. On the other hand, strain to failure of carburized IN-718 increased when compared to that of non-treated IN-718. This can be explained that the carburizing/annealing temperature (780 K) is close to the temperature (i. e. 785 K around half of the melting point 1570 K of IN-718) that can cause point defects and dislocation annihilation (recovery) in the plastic deformed surface introduced by mechanical machining.[85] This increase of strain to failure was not seen in annealed AISI-316L shown in Figure 3.15a. The carburizing/annealing temperature for AISI-316L is 720 K, which is 100 K lower than 835 K (half of the melting point 1670 K of AISI-316L), so possibly recovery (annihilation of point defects and dislocation) did not happen in AISI-316L specimen during the annealing process.

Although the annealed IN-718 tube had better strain to failure compared to that of the non-treated IN-718 tube, as seen in Figure 3.15b, the LTC IN-718 tube showed less strain to failure compared to that of non-treated sample. In contrast, Figure 4.4 suggested that the LTC IN-718 tensile bar had better strain to failure than that of a non-treated specimen. The area of the case is 12% of the cross-sectional area of the LTC IN-718 tube and that is only 4% of that of the LTC IN-718 tensile bar, implying that the carburized near-surface region on the IN-718 tube played a more important role than

on the IN-718 tensile bar to affect the strain to failure of the IN-718 specimens. Moreover, Niu[82] reported that dimples (seen in ductile fracture) were everywhere in the case region of LTC IN-718 after testing in the BWR simulated environment. Cracks cannot be found on the surface of carburized IN-718 shown in Figure 4.5b. Given all the discussion above, the carburization process did not compromise the SCC resistance of IN-718.

4.5 Irradiation Test

Figure 3.36c and Figure 3.38 suggested nano-sized carbides (i. e. 30−50 nm) were formed in LTC IN-718 after exposure to 1.5 MeV protons to 0.5 dpa at 620 K for 72 ks.

Bruemmer[86] reported that only vacancies and small (< 4 nm) dislocation loops can form in the AISI-316 specimen after exposure to low-temperature (i. e. < 620 K) and low-dose (i. e. 0.1 dpa to 5 dpa) conditions; however, radiation-induced voids and precipitation cannot form under these conditions. Chopra[87] also reported that radiation-produced segregation is not a concern at temperatures less than 620 K if the irradiation dose is kept low (i. e. less than 5 dpa). Considering the real working temperature of BWR is around 560 K, which is 60 K lower than the temperature that LTC IN-718 was exposed to, it is possible that no carbides will be detected if LTC IN-718 is placed in the real working environment of BWR.

In the 'Results' section, it is already shown that nano-sized carbides can also form in the LTC IN-718 after the PCHE-B process (simulating the LCA by exposing LTC IN-718 at 1070 K in air and vacuum for 3.6 ks). Generally, precipitates are not desired under low-temperature (i. e. < 620 K) and low-dose (i. e. 0.1 dpa to 5 dpa) conditions.

However, when segregation is not avoidable (i. e. LCA with temperature > 1000 K), nano-sized carbides are desired for the following reasons: (1) the corrosion resistance of

IN-718 can be mostly kept since nano-sized carbides minimally change the distribution of Cr and (2) forming nano-sized carbides prevent Cr forming the vaporized component ($CrO_2(OH)_2$), which will cause a large scale Cr depletion in the specimen.

Moreover, the nano-sized Cr carbides have narrow size distribution, as shown in Figure 3.38 and Figure 3.34, which may reduce the ripening rates induced by the elemental chemical potential difference from the surface of different sized particles.

5 Conclusions

1. Both the Cr-rich oxide layer and the underneath plastically-deformed layer on the surface of austenitic Fe–Cr–Ni alloys prevented the diffusion of carbon and nitrogen during LTC. The aqueous acid activation method is an effective way to remove both layers (i. e. to activate the surface of Fe–Cr–Ni alloys), compared to the double gaseous HCl activation method. However, the alloy surfaces cannot stay activated due to the quick reformation of the Cr-rich oxide when in air. By immersing the activated Fe–Cr–Ni alloys in ethanol, the reforming of Cr-rich oxide layer is retarded. To avoid the reformation of Cr-rich oxide layer during LTC, C_2H_2 is more appropriate than CO as a carbon source.
2. Ferromagnetic layers have been detected on the surface of LTC and LTNC IN-718. The ferromagnetism is probably induced by the change of electronic structure, which is introduced by infusion of interstitial solutes (C and N atoms) and lattice expansion after the LTC and LTNC process.
3. Cr depletion has been observed after CSS-engineered Fe–Cr–Ni alloys. In addition, three possible reactions during the LTC have been proposed because of Cr depletion:

$$2CO(g) = 2C(s) + O_2(g)\,, \tag{5.1}$$

$$4Cr(s) + 3O_2(g) = 2Cr_2O_3(s)\,, \tag{5.2}$$

$$CO(g) + H_2(g) = 2C(s) + H_2O(g)\,. \tag{5.3}$$

4. The high diffusivity of Cr at the carburization temperature in the near-surface region is mainly due to:
   (1) Higher carburizing temperatures yield higher Cr diffusivity.
   (2) Metal vacancies introduced by Cr depletion (the formation of evaporable $CrO_2(OH)_2$) will also increase the diffusivity of Cr.
5. CSS-engineered Fe–Cr-Ni alloys did not show observable property changes after PCHE-A treatment (simulating the working condition of BWR for 86.4 ks). This suggests good oxidation resistance and thermal stability of CSS-engineered Fe–Cr–Ni alloys in the working temperature of BWR for 86.4 ks.
6. After exposure in PCHE-B-Air (simulating the LCA condition of BWR), LTC AISI-316L oxidized severely, forming oxide layer with a thickness of $\approx 12\,\mu m$. Therefore, LTC AISI-316L cladding cannot survive under LCA conditions. Oxide layers with a total thickness of $\approx 5\,\mu m$ were formed on the surface of LTC AL-6XN after exposure in PCHE-B-Air, indicating a better high-temperature oxidation resistance of LTC AL-6XN than that of LTC AISI-316L. Carbide formed in LTC AL-6XN after exposure in PCHE-B-Air, implying that a poor thermal stability of LTC AL-6XN at the LCA temperature of BWR. Oxides were detected in the X-ray diffraction pattern of LTNC IN-718, however, they were absent in the LTC IN-718 after exposure in PCHE-B-Air, implying that the LTC IN-718 possessed the best high-temperature oxidation resistance among all

the CSS-engineered Fe–Cr–Ni alloys discussed in this thesis. Moreover, nano-sized instead of large size carbide was observed in the LTC IN-718 after the PCHE-B-Air treatment, indicating LTC IN-718 had best thermal stability among all CSS-engineered Fe–Cr–Ni alloys mentioned herein. When precipitates are not avoidable, nano-sized carbides are desired for the following reasons:

(1) The corrosion resistance can be mostly kept since nano-sized carbides only slightly change the distribution of Cr.

(2) Forming nano-sized carbides helped to prevent Cr and C depletion under the working environment of BWR and LCA.

In a word, LTC IN-718 has the best oxidation resistance and thermal stability under the LCA condition of BWR for 3.6 ks.

7. The lattice parameter contraction of the CSS-engineered Fe–Cr–Ni alloys after the PCHE-B-Air and PCHE-B-Vac relates to three major factors:

   (1) Cr depletion in the LTC process introduced lattice parameter contraction of AL-6XN and IN-718 in the first place, however, this lattice contraction was compensated by lattice parameter expansion by interstitial carbon atoms.

   (2) C loss after the PCHE-B tests revealed the nature of lattice contraction.

   (3) Chromium carbides further depleted the Cr from the matrix of AL-6XN and IN-718, so the lattice of AL-6XN and IN-718 further contracted.

8. Nano-sized carbides were also detected in LTC IN-718 after irradiation. Moreover, lack of cracks after the tensile test in a BWR simulated environment indicated that LTC did not compromise the SCC resistance of IN-718.

In conclusion, LTC IN-718 is the most promising candidate for nuclear reactor claddings materials among the CSS-engineered AISI-316L, AL-6XN, and IN-718.

6 Futurework

1. In order to investigate whether the protective thin film on the active surface of Fe–Cr–Ni ally is ethanol or ethoxide film, two potential techniques can be applied: (1) ellipsometry and (2) surface-enhanced Raman scattering. Moreover, the AAA process should be broadened to other acids, protective solvents (methanol, acetone *etc.*) and alloys.
2. More Cr depleted in LTNC IN-718 than in LTC IN-718. Probably nitriding would introduce Cr depletion as well as low-temperature carburization. Therefore, nitriding of IN-718 should be conducted to test whether low-temperature nitriding can cause Cr depletion as well.
3. No elements (Cr) depletion should be observed after the low-temperature carburization/nitriding process. In order to reduce the large scale of Cr depletion, acetylene instead of CO should be supplied as carburizing gas during the surface-engineering process.
4. The nature of the dense oxide layer formed on the surface of LTC IN-718 after the high temperature annealing should be investigated. The mechanism, that dense and protective (presumably Cr-rich) oxide layer formed on the surface of LTC IN-718 while Cr is depleted by (1) forming evaporable $CrO_2(OH)_2$ in the LTC process and (2) forming

nano-sized carbides in the high temperature annealing treatment, is worth investigating.

5. Orientation of grains changed in LTC Fe–Cr–Ni alloys. Electron backscatter diffractometry should be applied on the non-treated and carburized Fe–Cr–Ni alloys to investigate the rotation of grains. Moreover, strong asymmetric X-ray diffraction pattern was observed in LTC AL-6XN. TEM and simulation should be performed on this specimen to investigate how this strong asymmetric X-ray diffraction pattern is formed.
6. It is not clear how C and N solutes change the electronic structure of IN-718 in order to introduce ferromagnetism. First-principles calculations could be conducted to study the change of eletronic structure of LTC and LTNC IN-718.

Appendix A
Aqueous Acid Activation

It has been known that the efficiency of aqueous HCl activation is much higher than that of gaseous HCl activation. This is probably because AAA method suppresses the surface from immediately oxidizing for a short time, and allows sufficient time to load the specimens into the furnace and start carburization before the surface re-passivates, forming a new layer of Cr_2O_3-rich film.

Since an AISI-316L tube was successfully uniformly carburized by pre-dipping into an aqueous 22.4 at% HCl solution before CSS-engineering, the high temperature HCl activation process could be replaced by a room temperature aqueous HCl solution activation method. The problems of the existing technology (i. e. surface activation with the help of HCl gas at elevated temperature (520 to 720 K)) are numerous:

(1) The hot HCl gas causes rapid corrosion of the furnace hardware, which constitutes a significant cost factor.

(2) The HCl gas is problematic because of safety and environmental pollution and sustainability concern.

(3) In the current industrial process, surface activation requires a total of six hours of processing time.

The above factors increased production costs. However, aqueous HCl activation will be a time saving, low cost and safe way to activate the surface of AISI-316L, if successfully implemented.

To verify these hypotheses, several experiments were designed and performed. One of the AISI-316L coupons was ultrasonically cleaned in ethanol for 300 s (5 min), and then dried with compressed air prior to carburization. The metallography indicated that

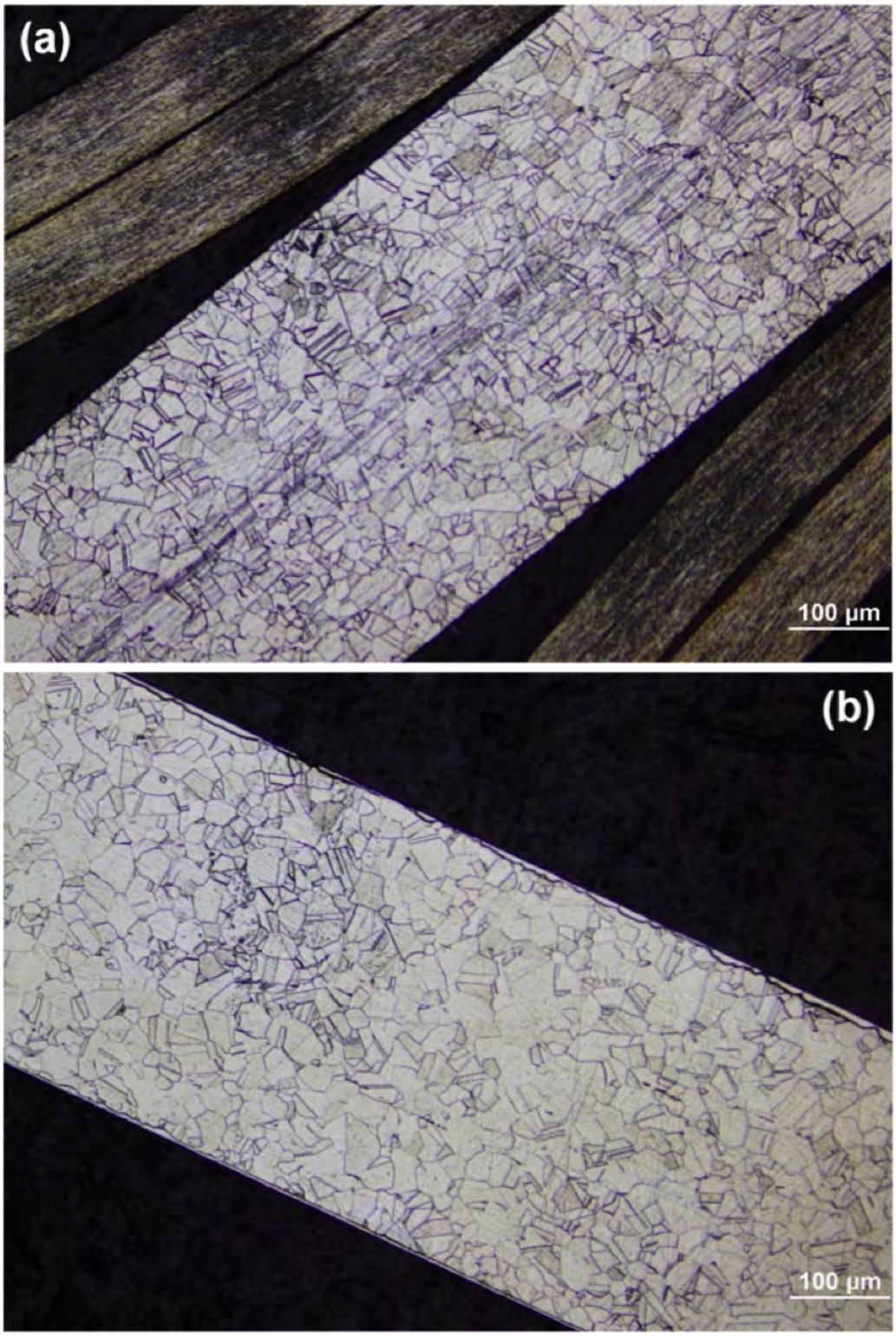

Figure A.1. (a) AISI-316L coupon was ultrasonically cleaned prior to carburization. (b) Metallography of AISI-316L coupon, which was ultrasonically cleaned, dipped into HCl for 600 s (10 min) and dried with compressed air, after carburization.

no case is present, as shown in Figure A.1a. The other AISI-316L coupon was ultrasonically cleaned with ethanol, dried with compressed air, then dipped into highly concentrated aqueous HCl solution for 600 s (10 min) and again dried with compressed air. The metallography showed carburized but non-uniform case, as shown in Figure A.1b. Another experiment on the aqueous HCl activation was performed. Again, all the AISI-316L coupons were ultrasonically cleaned in ethanol for 300 s (5 min). One AISI-316L coupon was only cleaned with ethanol before carburization, and the metallography showed no case, as seen in Figure A.2a. The other AISI-316L coupon was dipped into aqueous HCl solution for 9 ks (2.5 h) and later immersed in ethanol prior to carburization. The metallography of the HCl immersed samples suggested that a case with some pits formed, as shown in Figure A.1b.

From the two experiments mentioned above, conclusions can be made that:

(1) Dipping the sample into aqueous HCl does activate the surface of AISI-316L coupon.

(2) After being dipped into aqueous HCl, the AISI-316L should not be rinsed with water, which tested did not give good results (i. e. the surface showed no carburization).

(3) If the specimen was immersed in ethonal after the aqueous HCl activation process, a uniform case can be achieved.

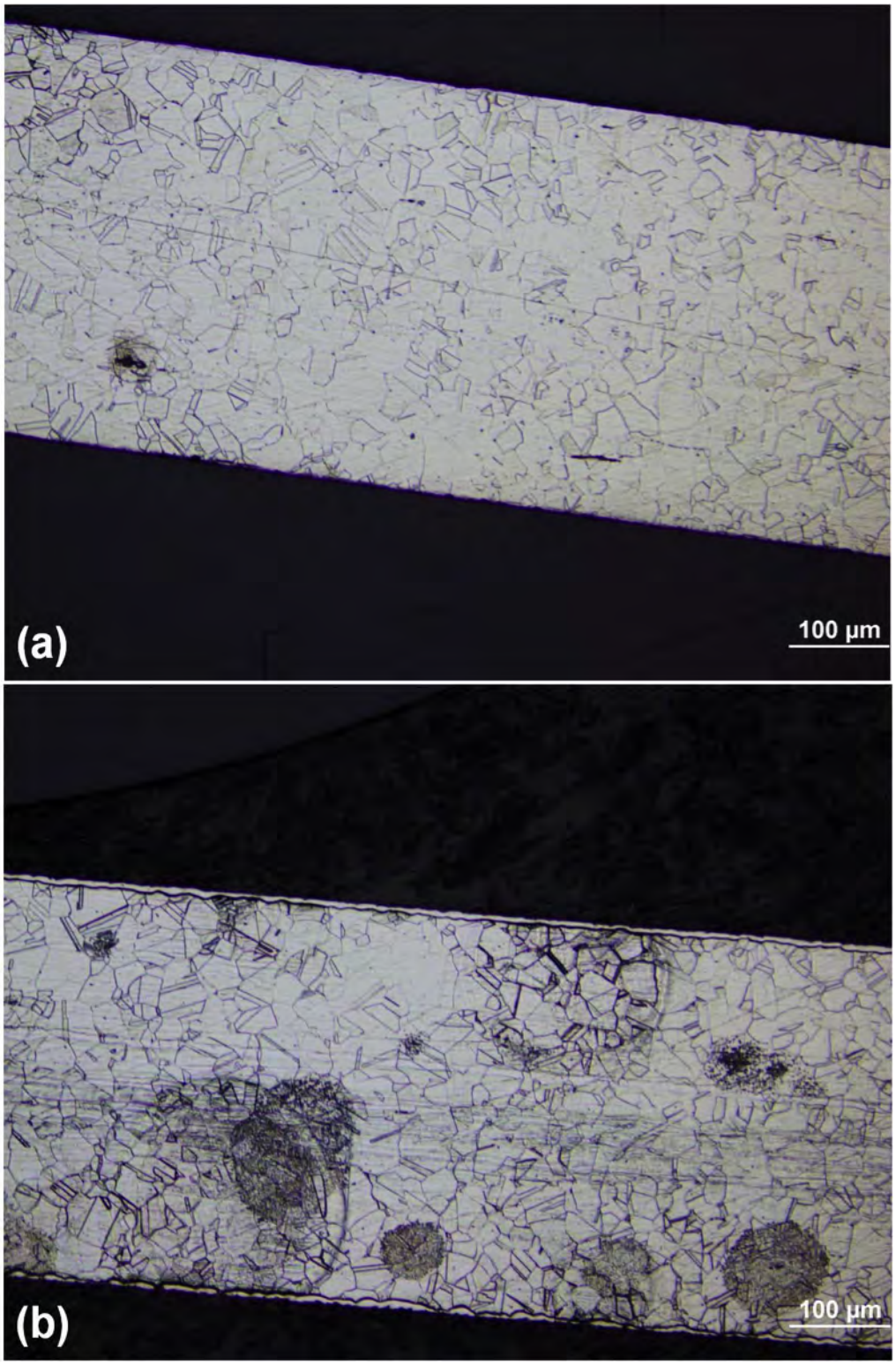

Figure A.2. (a) AISI-316L coupon was only ultrasonically cleaned in ethanol for 300 s (5 min) prior to carburization. (b) Metallography of AISI-316L coupon, which was dipped in aqueous HCl for 9 ks (2.5 h) and immersed in ethanol without drying, after carburization.

Appendix B
Long term annealing of carburized AISI-316L

Dong[28] reported that if the annealing temperature is lower than 670 K, the CSS-engineered AISI-316L can be stable and be precipitate-free for years. However, the distribution of carbon after long term annealing process is unknown, so Wang *et al.*[88] ran a long term annealing on carburized AISI-316L specimens. Indeed, precipitates were not observed in XRD patterns of long term annealed AISI-316L sample. However, Wang *et al.* found that carburized AISI-316L ferrule annealed at 650 K for 21 Ms (8 months) has 50% more carbon than the as-carburized AISI-316L specimen, meaning the carburized AISI-316L is absorbing C from the air.

To verify this result, another experiment was performed on carburized AISI-316L. Two specimens were annealed at 650 K for 6.6 Ms (11 weeks): the first AISI-316L ferrule was sealed in a vacuum ampoule (2 Pa), and the second specimen was exposed to air. It was expected that the integrated carbon concentration of the vacuum annealed sample is the same as that of the as-carburized AISI-316L.

Figure B.1 shows the carbon concentration depth profiles of as-carburized and annealed AISI-316L samples. Both the carbon concentration profiles of in-air and in-vacuum annealed carburized AISI-316L showed the inward diffusion of carbon rather than outward diffusion of carbon atoms. The ratio of the integrated carbon concentration profile among vacuum-annealed, as-carburized and air-annealed AISI-316L is listed in Table B.1. The integrated carbon concentration profile between vacuum and reference is 1.03, suggesting that the vacuum-annealed specimen did not take carbon in during the annealing process. On the other hand, the integrated carbon concentration profile between air-annealed and reference and that between air-annealed and vacuum is 1.17

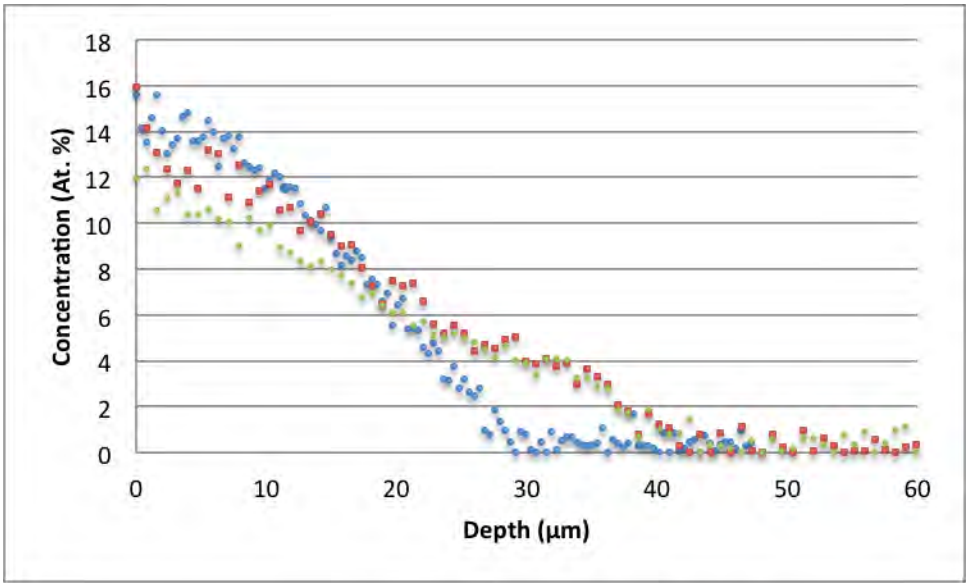

Figure B.1. Carbon concentration of as-carburized (Blue), 653 K-vacuum-annealed (Green) and 653 K-air-annealed (Red) AISI-316L as a function of case depth.

and 1.14, respectively. This again indicated that the air-annealed carburized AISI-316L is absorbing C from the air during the long term annealing process.

	Vacuum to reference	Air to reference	Air to vacuum
Ratio	1.03	1.17	1.14

Table B.1. Carbon profile integration ratio between as-carburized, air-annealed and vacuum-annealed AISI-316L specimens.

Figure B.2 implies that the integrated Fe concentration profile of as-carburized and air-annealed AISI-316L is very close, which indicates that the Fe concentration of as-carburized AISI-316L did not change before and after the long term annealing process, while Table B.1 suggests that a large amount of carbon atoms were absorbed in the long term annealing process. This result also indicates the absorption of carbon is true rather than artifact.

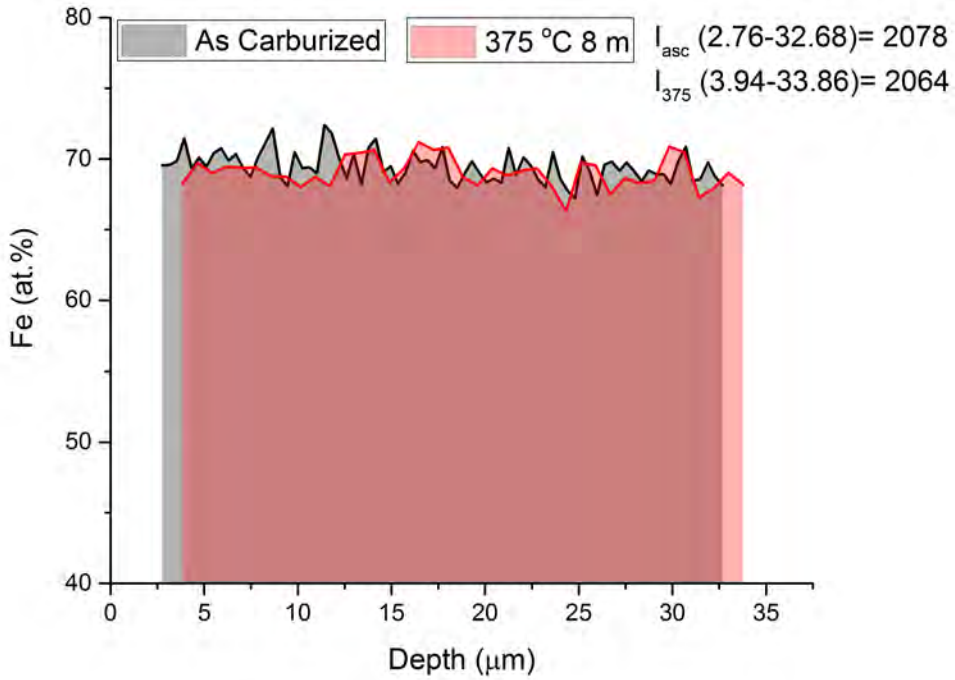

Figure B.2. Integration of iron concentration profile of as-carburized and air-annealed AISI-316L samples. (carbon is removed from the concentration profile)

The only source of C in the air is from carbon dioxide. Although it is not clear why carburized AISI-316L can absorb carbon from air, this process is theoretically and thermodynamically possible. More investigations should be done into this phenomenon.

Appendix C
LTC of nanostructured AISI-316L

Nanostructured AISI-316L samples were received from Zhenbo Wang, a Professor at IMRCAS (Institute of Metal Research, Chinese Academy of Science).

Bei *et al.*[89] reported the nitrogen diffusion coefficient in nanostructured steel is much higher than that of non-treated steel. A case, which is two times thicker in comparison to non-treated steel, can be achieved after gas phase based nitriding. Tong *et al.*[90] found that pure iron can be nitrided at lower temperatures if the surface of the iron specimen is nanostructured. All these experiments indicated that nitrogen atoms diffuse more quickly in the grain boundaries than diffusing in the lattice of steel and iron.

It will be very interesting to see whether carbon atoms diffuse faster in grain boundaries than diffusing in the lattice. The AISI-316L specimens were processed with SMRT (surface mechanical rolling treatment), as shown in Figure C.1. The AISI-316L rod was rotating with the speed V, while a force was applied on the rotating AISI-316L specimen inducing plastic deformation on the surface of the AISI-316L rod. Finally, a gradient nanostructured surface layer with the thickness of 400 μm was formed on the AISI-316L specimen after the SMRT. The grain size on the top surface of this nanostructured layer can reach 30 nm. The nano-sized grains can stay nano-sized at the temperature, 720 K, of LTC.

The nanostructured layer contains 100 % of austenitic nano-sized AISI-316L grains. In order to clearly see the difference between the specimen processed with SMRT and the non-treated specimen, the top layer of SMRT treated AISI-316L specimen was polished off, as shown in Figure C.2. If the diffusion coefficient of carbon in nanostructured

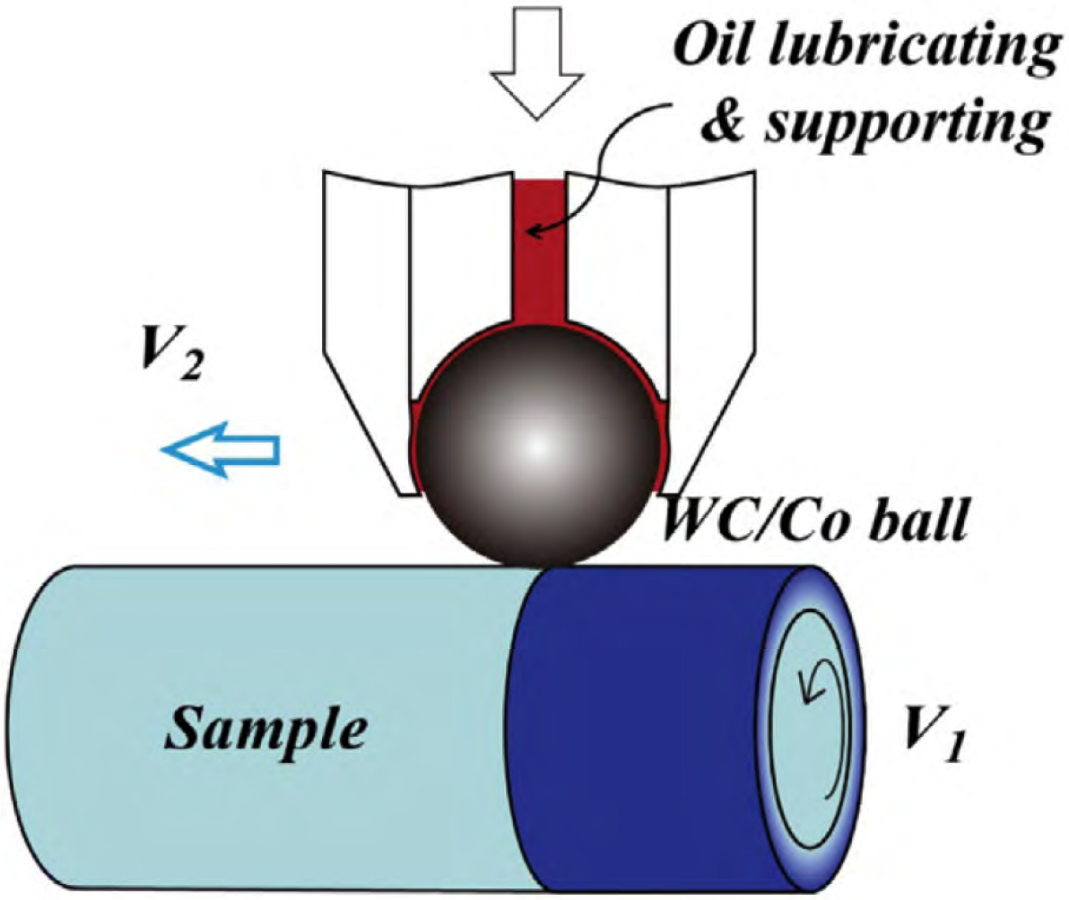

Figure C.1. Schematic diagram of the SMRT set-up.[91]

layer of the AISI-316L specimen is different from that of bulk AISI-316L, the case depth is expected to have an immediate change.

LTC was carried out at 690 K for 72 ks and the double activation was also conducted at 690 K with each activation lasting 7.2 ks. Figure C.3 presents the micrograph of the AISI-316L specimen after LTC. The top left is the polished area of AISI-316L, and the bottom right is the SMRT area of AISI-316L. However, there is no difference in the case depth in these two areas, suggesting that the carbon atoms can diffuse to the lattice as fast as in the grain boundaries.

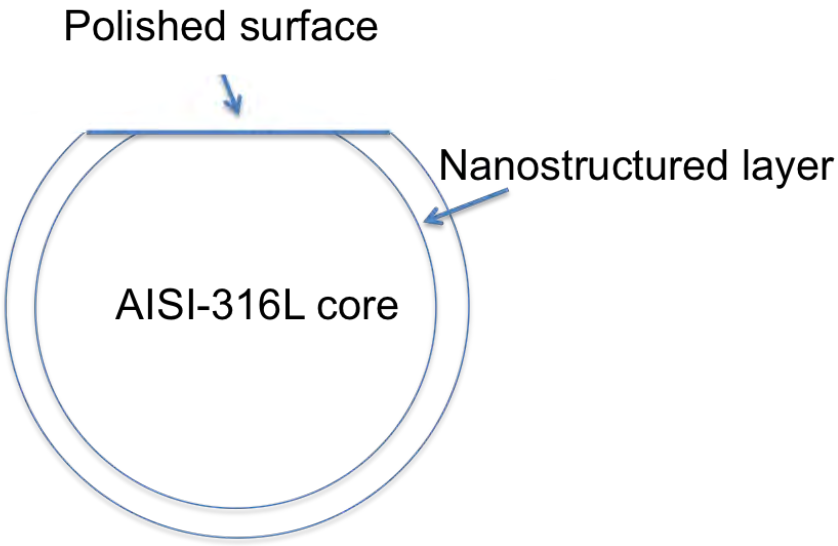

Figure C.2. Illustration of the AISI-316L specimen.

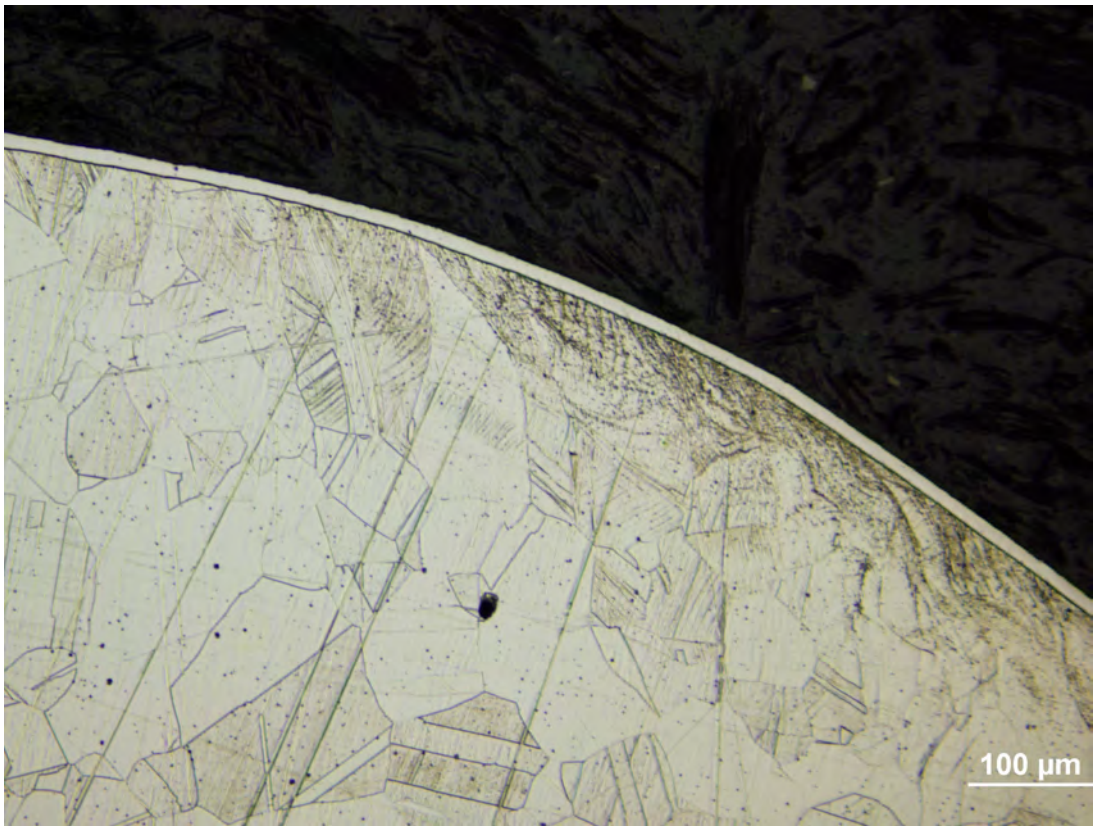

Figure C.3. Micrograph of LTC AISI-316L.

Complete References

[1] Zinkle SJ, Busby JT. Materials Today 2009;12:12.

[2] Abe A, Giovedi C, da Souza Gomes D, e Silva AT. Journal of Energy and Power Engineering 2014;8.

[3] Lucas TR. The effect of thermal aging and boiling water reactor environment on Type 316L stainless steel welds. Ph.D. thesis, Massachusetts Institute of Technology, 2011.

[4] Attia MH. Tribology international 2006;39:1320.

[5] Fisher NJ, Weckwerth MK, Grandison DA, Cotnam BM. Nuclear engineering and design 2002;213:79.

[6] Kang KH, Ryu HJ, Song KC, Yang MS. Journal of nuclear materials 2002;301:242.

[7] Kawasaki S, Furuta T, Suzuki M. Journal of Nuclear Science and Technology 1978; 15:589.

[8] Leistikow S, Schanz G. Nuclear engineering and design 1987;103:65.

[9] Pawel R, Cathcart J, McKee R. Journal of The Electrochemical Society 1979; 126:1105.

[10] Cheng T, Keiser JR, Brady MP, Terrani KA, Pint BA. Journal of Nuclear Materials 2012; 427:396.

[11] Zhang L, Bao Y, Tang R. Nuclear Engineering and Design 2012;249:180.

[12] Pint BA, Terrani KA, Brady MP, Cheng T, Keiser JR. Journal of Nuclear Materials 2013; 440:420.

[13] Greene G, Finfrock C. Oxidation of metals 2001;55:505.

[14] Lebrun J, Poirier L, Hertz D, Lincot C. Surface engineering 2002;18:423.

[15] Asteman H, Segerdahl K, Svensson JE, Johansson LG, Halvarsson M, Tang JE. In: Materials Science Forum. Trans Tech Publ, vol. 461, 2004; pp. 775–782.

[16] Bhavsar RB, Collins A, Silverman S. Minerals, Metals and Materials Society/AIME, Superalloys 718, 625, 706 and Various Derivatives(USA), 2001pp. 47–55.

[17] Ganesan P, Renteria C, Crum J. Superalloys 1991;718:625.

[18] MacDonald DD, Urquidi-MacDonald M. Corrosion Science 1991;32:51.

[19] Russell AJ, Tromans D. Metallurgical Transactions A 1979;10:1229.

[20] Agarwal N, Kahn H, Avishai A, Michal G, Ernst F, Heuer A. Acta Materialia 2007; 55:5572.

[21] Sharghi-Moshtaghin R, Kahn H, Ge Y, Gu X, Martin FJ, Natishan PM, Rayne RJ, Michal GM, Ernst F, Heuer AH. Metallurgical and Materials Transactions A 2010; 41:2022.

[22] O'Donnell L, Michal G, Ernst F, Kahn H, Heuer A. Surface Engineering 2010;26:284.

[23] Martin F, Lemieux E, Newbauer T, Bayles R, Natishan P, Kahn H, Michal G, Ernst F, Heuer A. Electrochemical and Solid-State Letters 2007;10:C76.

[24] Martin F, Natishan P, Lemieux E, Newbauer T, Rayne R, Bayles R, Kahn H, Michal G, Ernst F, Heuer A. Metallurgical and Materials transactions A 2009;40:1805.

[25] Dong H, Qi PY, Li X, Llewellyn R. Materials Science and Engineering: A 2006; 431:137.

[26] Ernst F. Improved Accident Tolerance of Austenitic Stainless Steel Cladding through Colossal Supersaturation with Interstitial Solutes. Unpublished Project Proposal.

[27] Michal G, Ernst F, Kahn H, Cao Y, Oba F, Agarwal N, Heuer A. Acta Materialia 2006; 54:1597.

[28] Dong H. International Materials Reviews 2010;55:65.

[29] Michal G, Gu X, Jennings W, Kahn H, Ernst F, Heuer A. Metallurgical and Materials Transactions A 2009;40:1781.

[30] Li Z, Ernst F, Heuer A. 2013 ANS Winter Meeting and Nuclear Technology expo 2013; 109:304.

[31] Ge Y, Ernst F, Kahn H, Heuer AH. Metallurgical and Materials Transactions B 2014; 45:2338.

[32] Ernst F, Cao Y, Michal G, Heuer A. Acta Materialia 2007;55:1895.

[33] Cao Y, Ernst F, Michal G. Acta Materialia 2003;51:4171.

[34] Williams P, Collins S. JOM 2008;60:27.

[35] Ge Y. Low-Temperature Acetylene-Based Carburization and Nitrocarburization of 316L Austenitic Stainless Steel. Ph.D. thesis, Case Western Reserve University, 2013.

[36] Wu D. Low-Temperature Gas-Phase Nitriding and Nitrocarburizing of 316L Austenitic Stainless Steel, 2013.

[37] Somers M, Christiansen T. Carburizing in hydrocarbon gas, 2006. URL https://www.google.com/patents/WO2006136166A1?cl=pt. WO Patent App. PCT/DK2006/000,363.

[38] Zhang Z, Bell T. Surface Engineering 1985;1:131.

[39] Li C, Bell T. Corrosion Science 2004;46:1527.

[40] Alves C, Da Silva E, Martinelli A. Surface and Coatings Technology 2001;139:1.

[41] Ernst F, Heuer A, Michal G. Surface hardening of Ti alloys by gas-phase nitridation: kinetic control of the nitrogen activity, 2005. US Patent App. 11/145,142.

[42] Agaponova A. Encapsulation Method for Surface Engineering of Corrosion-resistant Alloys by Low-temperature Nitro-carburization. Master's thesis, Case Western Reserve University, 2016.

[43] Agaponova A, Ernst F, Heuer A. Encapsulation Method for Alloy Surface Engineering by Infusing High Concentrations of Interstitial Solute. Unpublished Data.

[44] Funatani K. Metal science and heat treatment 2004;46:277.

[45] Jing Y, Jun W, Tan G, Ji X, Hongyuan F. ISIJ International 2016;56:1076.

[46] Nemat-Nasser S, Guo WG, Kihl DP. Journal of the Mechanics and Physics of Solids 2001;49:1823.

[47] Unocic KA, Pint B. In: 8th International Symposium on Superalloy 718 and Derivatives. Wiley Online Library, 2014 pp. 667–677.

[48] Caliari FR, da Rosa EF, da Silva MA, Reis DAP. Tecnol Metal Mater Miner 2014;11:189.

[49] Wu D, Kahn H, Dalton J, Michal G, Ernst F, Heuer A. Acta Materialia 2014;79:339.

[50] Standard A. Standard test methods for tension testing of metallic materials 2011; 3:66.

[51] Ziegler JF, Ziegler MD, Biersack JP. Nuclear Instruments and Methods in Physics Research Section B: Beam Interactions with Materials and Atoms 2010;268:1818.

[52] Ziegler JF. Nuclear instruments and methods in physics research section B: Beam interactions with materials and atoms 2004;219:1027.

[53] Menthe E, Rie KT, Schultze J, Simson S. Surface and Coatings Technology 1995; 74:412.

[54] Olsson CO, Landolt D. Electrochimica acta 2003;48:1093.

[55] Heuer A, Kahn H, Ernst F, Michal G, Hovis D, Rayne R, Martin F, Natishan P. Acta Materialia 2012;60:716.

[56] Li Z, Ernst F, Kahn H, Heuer A. Alloy surface activation by immersion in aqueous acid solution, 2015. URL https://www.google.com/patents/WO2015171698A1?cl=en. WO Patent App. PCT/US2015/029,372.

[57] Higashi G, Chabal Y, Trucks G, Raghavachari K. Applied physics letters 1990;56:656.

[58] Allongue P, De Villeneuve CH, Pinson J, Ozanam F, Chazalviel J, Wallart X. Electrochimica Acta 1998;43:2791.

[59] McClintock DA, Hyres JW, Vevera BJ. Journal of Nuclear Materials 2014;450:176.

[60] Schumpe A, Luehring P. Journal of Chemical and Engineering Data 1990;35:24.

[61] Takase A, Miyakawa K. Japanese journal of applied physics 1991;30:L1508.

[62] Lubinkowski JJ, Gimenez Arrieche C, McEwen WE. The Journal of Organic Chemistry 1980;45:2076.

[63] Lin C, Al-Muhtaseb SA, Ritter JA. Journal of sol-gel science and technology 2003; 28:133.

[64] Brown DA, Cunningham D, Glass W. Journal of the Chemical Society A: Inorganic, Physical, Theoretical 1968pp. 1563–1568.

[65] Holec P, Plocek J, Nižňanskỳ D, Vejpravova JP. Journal of sol-gel science and technology 2009;51:301.

[66] Kubo T, Nanao H, Mori S, Enomoto Y, Nie H, Nomura H. Wear 2010;268:1225.

[67] Atomic Radius of the Elements. URL http://periodictable.com/Properties/A/AtomicRadius.v.html.

[68] Ernst F, Avishai A, Kahn H, Gu X, Michal G, Heuer A. Metallurgical and Materials Transactions A 2009;40:1768.

[69] Agarwala R, Naik M, Anand M, Paul A. Journal of Nuclear Materials 1970;36:41.

[70] Christiansen TL, Somers MA. International Journal of Materials Research 2008; 99:999.

[71] Asteman H, Svensson JE, Johansson LG, Norell M. Oxidation of Metals 1999;52:95.

[72] Christiansen T, Somers MA. Surface Engineering 2005;21:445.

[73] Rice F, Vollrath R. Proceedings of the National Academy of Sciences 1929;15:702.

[74] Chang R. Physical chemistry for the chemical and biological sciences. University Science Books, 2000.

[75] Inconel Alloy 718. URL http://www.specialmetals.com/assets/documents/alloys/inconel/inconel-alloy-718.pdf.

[76] Wu D, Kahn H, Michal G, Ernst F, Heuer A. Scripta Materialia 2011;65:1089.

[77] Besnus M, Gottehrer Y, Munschy G. physica status solidi (b) 1972;49:597.

[78] Takahashi S, Sato Y, Kamada Y, Abe T. Journal of magnetism and magnetic materials 2004;269:139.

[79] Chen J, Farkas D, Reynolds W. Acta materialia 1997;45:4415.

[80] Nammas S, Al-Omari I, Mahmood S. Journal of alloys and compounds 2003;353:53.

[81] Wang J, Li Z, Wang D, Qiu S, Ernst F. Acta Materialia 2017.

[82] Niu W. Corrosion resistance of collossal superstruated Fe–Cr–Ni alloys. Unpublished Data.

[83] Prasanna HU, Udupa KR. Procedia Engineering 2013;55:566.

[84] Sundararaman M, Nalawade S, Verma A, Singh J, Kishore R. In: Proceedings of the international conference on advances in electron microscopy and related techniques and thirty first annual meeting of EMSI: souvenir and book of abstracts. 2010 .

[85] Mittemeijer EJ. In: Fundamentals of Materials Science, Springer, pp. 371–461. 2010 .

[86] Bruemmer SM, Simonen EP, Scott PM, Andresen PL, Was GS, Nelson JL. Journal of Nuclear Materials 1999;274:299.

[87] Chopra O, Rao A. Journal of Nuclear Materials 2011;409:235.

[88] Wang J, Ernst F, Li Z, Wang D, Qiu S. Thermal Stability of Low-Temperature-Carburized Austenitic Stainless Steel. In Preparation.

[89] BEll D, Gu J, Pan J. J. Mater. Sci. Technol 2002;18:1.

[90] Tong W, Tao N, Wang Z, Lu J, Lu K. Science 2003;299:686.

[91] Huang H, Wang Z, Lu J, Lu K. Acta Materialia 2015;87:150.